

Anders Kastet
Ahmad Adnan Alnaser

Estimating and Predicting Dynamic Properties of Stress-laminated Timber Bridges

Master's thesis in Structural Engineering, TKT4950
Supervisor: Anders Rønnquist
Co-supervisor: Petter Juell Nåvik and Haris Stamatopoulos
June 2022



Raufoss bridge, captured by Petter Juell Nåvik

Anders Kastet
Ahmad Adnan Alnaser

Estimating and Predicting Dynamic Properties of Stress-laminated Timber Bridges

Master's thesis in Structural Engineering, TKT4950
Supervisor: Anders Rønnquist
Co-supervisor: Petter Juell Nåvik and Haris Stamatopoulos
June 2022

Norwegian University of Science and Technology
Faculty of Engineering
Department of Structural Engineering



MASTER THESIS 2022

SUBJECT AREA: Dynamics, Timber Structures	DATE: 11.06.2022	NO. OF PAGES: 12 + 77 + 9
--	---------------------	------------------------------

TITLE: Estimating and Predicting Dynamic Properties of Stress-laminated Timber Bridges Estimering av dynamiske egenskaper til tverrspente limtrebruer	
BY: Anders Kastet and Ahmad Adnan Alnaser	 

<p>SUMMARY: Stress-laminated Timber bridges have recently grown in popularity due to their speed of manufacture and great adaptability. Timber is considered carbon-neutral and is therefore considered an essential building material in Norway's mission to achieve carbon-neutrality by 2030. Design criteria of these lightweight, slender structures are mainly governed by serviceability criteria.</p> <p>Stiffnesses from non-structural components are typically neglected during dynamic analysis. The asphalt pavement has been proven to greatly influence the dynamic properties of the Stress-laminated Timber bridges. Accurately predicting the asphalt's contribution for different temperatures is therefore essential to accurately predict the dynamic properties of the bridges.</p> <p>This thesis analyzed acceleration data from two stress-laminated timber bridges located in Raufoss and Brumunddal, respectively. The bridges were excited by Jumping Tests and Modal Hammer Tests. These data sets were analyzed using BFD, SSI-Cov, and SSI-DD. The SSI methods are only meant to analyze white-noise data. However, the methods accurately managed to predict the dynamic properties from the Modal Hammer Test. SSI-Cov yielded superior estimates for natural frequencies and damping ratios but struggled with the energy dissipation between mode shapes for closely spaced modes.</p> <p>A Python script that modeled, ran, and extracted estimated mode shapes and natural frequencies of Stress-laminated Timber bridges in ABAQUS was implemented. The material properties of the asphalt pavement were estimated as a function of temperature and loading frequency. The stiffness caused by the continuous layer of asphalt, was modelled as a rotational stiffness in ABAQUS. The rotational stiffness was optimized to minimize the error for the bridges' first natural frequency. The results yielded accurate predictions of natural frequencies and mode shapes. The mode shapes were, however, hardly affected by the rotational stiffness. This was caused by the boundary edges of the ABAQUS model being distorted.</p>

RESPONSIBLE TEACHER: Anders Rønnquist
SUPERVISOR(S): Petter Juell Nåvik and Haris Stamatopoulos
CARRIED OUT AT: Department of Structural Engineering, NTNU



MASTEROPPGAVE 2022

FAGOMRÅDE:	DATO:	ANTALL SIDER:
Dynamikk, Trekonstruksjoner	11.06.2022	12 + 77 + 9

TITTEL:

Estimering av dynamiske egenskaper til tverrspente limtrebruer

Estimating and Predicting Dynamic Properties of Stress-laminated Timber Bridges

UTFØRT AV:

Anders Kastet

og

Ahmad Adnan Alnaser



SAMMENDRAG:

Populariteten til tverrspente limtrebruer har økt den siste tiden grunnet rask byggetid og god tilpasningsevne. Treverk er betraktet som et karbonnøytralt byggemateriale og dermed ansett som et sentralt byggemateriale for å oppnå Norges klimamål om å bli karbonnøytralt innen 2030. Designkriteriet for disse lette, slanke konstruksjonene er hovedsakelig begrenset av bruksgrensetilstanden.

Stivheten til ikke-strukturelle komponenter er som regel neglisjert i dynamiske analyser. Det har blitt vist at asfaltdekket påvirker de dynamiske egenskapene til tverrspente limtrebruer. Det er dermed essensielt å nøyaktig forutse asfaltens bidrag for de dynamiske egenskapene for ulike temperaturer.

Denne masteren analyserte akselerasjonsdata fra to ulike tverrspente limtrebruer som befinner seg i Raufoss og Brumunddal. Bruene ble eksitert ved bruk av hopptester og modalhammertester. Tidsseriene ble analysert ved bruk av BFD, SSI-Cov og SSI-DD. SSI-metodene er egentlig kun egnet for å analysere hvitt støy, men metodene greide å estimere de dynamiske egenskapene fra modalhammertestene. SSI-Cov ga bedre estimater for egenfrekvenser og dempingsforhold, men metoden strevde med energidissipasjonen mellom modalformene til nærliggende moder.

En Python-kode som modellerte, kjørte og hentet ut modalformer og egenfrekvenser fra de modellerte tverrspente limtrebruene i ABAQUS ble implementert. ABAQUS-modellen estimerte det dynamiske bidraget til asfalten som en funksjon av temperatur og lastfrekvens. Stivheten forårsaket av det kontinuerlige asfaltlaget ble modellert som en rotasjonsstivhet. Rotasjonsstivheten ble optimert for å minimere feilen til bruens første egenfrekvenser. Modellen ga gode estimater for egenfrekvensene samt gode estimater for modalformer. Modalformene ble nesten ikke påvirket av rotasjonsstivheten ettersom opplagerkantene ikke deformerte seg lineært. Lineær deformasjon av opplagerkantene var forventet.

FAGLÆRER: Anders Rønquist

VEILEDER(E): Petter Juell Nåvik and Haris Stamatopoulos

UTFØRT VED: Department of Structural Engineering, NTNU

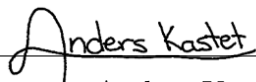
Preface


This master's thesis concludes the final work of the authors' study program *Civil and Environmental Engineering* at the *Norwegian University of Science and Technology* (NTNU). The work lasted the entire spring semester of 2022. Both participants contributed equally, and the thesis corresponds to 30 credits per student.

The authors share a common interest of structural dynamics and coding. This thesis enabled the authors to thoroughly study and implement three modal analysis techniques and learn ABAQUS modelling in Python. The thesis further builds upon a thesis written during the spring of 2021 named "*Dynamic Properties of Stress-laminated Timber Bridges*". The previously written thesis conducted all measurements thus resulting in this thesis solely being analytical.

We want to thank our supervisor Anders Rønnquist and co-supervisor Haris Stamatopoulos. We are especially grateful to our co-supervisor Petter Juell Nåvik for the continuous guidance and countless advice. Thanks to Hao Chen for helping with the modelling of the asphalt stiffness and giving us access to his current work and Gunnstein Thomas Frøseth for helping with the *Strid* package. Special thanks to our fellow students Andreas Grøndahl Nourouzi, Erik Hattestad, Olav Guddal, Stian Gundersen Raniszewski, and Trygve Vangsnes for always lending a helping hand.

Trondheim, 11.06.2022


Anders Kastet


Ahmad Adnan Alnaser

Contents

Abstract	i
Sammendrag	ii
Preface	iii
1 Introduction	1
1.1 Background	1
1.2 Research	2
1.3 Research Questions	3
1.4 Thesis Outline	3
1.5 Limitations	4
2 Stress-laminated Timber Bridges	5
3 Theory	7
3.1 State-space Model	7
3.1.1 Stochastic Subspace Identification	12
3.2 Stabilization Diagram	18
3.3 Basic Frequency Domain Method	19
3.4 Welch’s Method	21
3.5 Modal Assurance Criterion	21
3.6 Modal Phase Collinearity	21
3.7 Material Properties of Asphalt	22
3.8 Human Induced Frequencies	23
4 Method	24
4.1 Data Collection	24
4.1.1 Equipment	24
4.1.2 Sensor Placement	24
4.1.3 Excitation Methods	25
4.2 Analytical Analysis	25
4.2.1 Basic Frequency Domain Method	25
4.2.2 Stochastic Subspace Identification Methods	26

4.3	Numeric Modelling	26
4.3.1	Creating the Parts	27
4.3.2	Defining the Materials	28
4.3.3	Assigning Cross-sections	29
4.3.4	Assembly, Boundary Conditions, Constraints, and Step	29
4.3.5	Rotational Stiffness	30
4.3.6	Creating Field-outputs	30
4.3.7	Post-processing	30
5	Bridges	31
5.1	Raufoss	31
5.2	Brumunddal	32
6	Results and Discussion	33
6.1	Raufoss Bridge	33
6.1.1	Basic Frequency Domain Method	33
6.1.2	Stochastic Subspace Identification	36
6.1.3	Finite Element Model Comparison	45
6.1.4	Comfort Criterion	50
6.2	Brumunddal Bridge	51
6.2.1	Basic Frequency Domain Method	51
6.2.2	Stochastic Subspace Identification SSI	55
6.2.3	Finite Element Model Comparison	64
6.2.4	Comfort Criterion	69
6.3	Final Comparison	70
7	Concluding Remarks	72
7.1	Conclusion	72
7.2	Further Work	73
	Bibliography	74
	Appendices	78
A	Python Code to Model the Bridge in ABAQUS	78
B	Zip-file	85

Acronyms

BFD Basic Frequency Domain.

DFT Discrete Fourier Transform.

LQ Orthogonal Decomposition into Lower Trapezoidal matrices.

MAC Modal Assurance Criterion.

MHT Modal Hammer Test.

MPC Modal Phase Collinearity.

OMA Operational Modal Analysis.

PSD Power Spectral Density.

SLT Stress-laminated Timber.

SSI Stochastic Subspace Identification.

SSI-Cov Covariance-Driven Stochastic Subspace Identification.

SSI-DD Data-Driven Stochastic Subspace Identification.

SVD Singular Value Decomposition.

Chapter 1

Introduction

1.1 Background

Timber bridges have rapidly grown in popularity in recent years. This popularity is caused by the speed of manufacture and great adaptability of timber structures. Timber has always been a popular building material due to the vast availability of woodlands. Timber was most likely the first material employed to construct bridges simply by placing wooden logs to span watercourses [1].

In recent years, the importance of preserving the environment has become apparent. The Norwegian government put forward a plan for Norway to achieve carbon-neutrality by 2030 [2]. Timber is considered a renewable, carbon-neutral material. Carbon dioxide is stored in the trunk of the trees but as the trees grow larger, they absorb less carbon dioxide. Chopping down the larger trees enables new trees to grow in their place. The timber may be used in constructions further preventing the carbon dioxide from entering the atmosphere during the lifespan of the structure. Therefore, reducing the use of steel and concrete and replacing them with timber, would greatly decrease the structure's carbon footprint. Additionally, timber is considered durable and requires minimal maintenance if properly treated with preservatives. More information about the advantages of using timber as a building material can be read in [3] and [2].

Estimating the natural frequencies of footbridges is essential to ensure the safety and comfort of pedestrians. Several bridges have endured failure due to dynamic human-induced loading caused by crowds [4]. This led to several bridges displaying signs for troops to break step while crossing. One such sign was displayed on a railway suspension bridge at Niagara Falls that read as follows [5]:

A fine of \$50 to \$100 will be imposed for marching over this bridge in rank and file or to music, or by keeping regular step. Bodies of men or troops must be kept out of step when passing over this bridge. No musical band will be allowed to play while crossing except when seated in wagons or carriages.

Stress-laminated Timber (SLT) decks are commonly used for timber footbridges. However, precisely estimating the dynamic behavior of SLT decks in the design stage has been proven difficult, emphasizing the need for proper finite element models of these types of structures. Usually, non-structural parts, such as asphalt, may be neglected in the design phase. This is, however, not the case for the slender, lightweight SLT decks, where the asphalt pavement may drastically influence the dynamic behavior [6]. Safety and comfort are essential in bridge engineering. Due to SLT decks being lightweight and slender, they are typically governed by comfort criteria. Modes with natural frequencies greater than 5 Hz are exempt from any comfort criteria. Modes with lower natural frequencies may not experience an acceleration greater than 0.7 m/s^2 in the vertical direction induced by pedestrians crossing the bridge [7]. Estimations of the acceleration depend on the total mass of the bridge, natural frequency, and damping ratio further emphasizing the importance of accurately estimating the dynamic properties of the bridge [8]. The standard suggests a damping ratio of 1.5% for timber bridges.

1.2 Research

Timber bridges are typically lightweight, slender structures resulting in the design mainly being limited by serviceability criteria such as vibration and maximum deflection. The bridges have a high live-load to death-load ratio resulting in the dynamic properties being susceptible to added weight. Gülzow and coworkers [9] studied the dynamic properties of timber bridges with and without asphalt. Their research indicates that bridges yield lower natural frequencies after the asphalt pavement was applied due to the additional mass. Peeters and De Roeck [10] reported that the natural frequencies increased significantly as the temperature went below 0°C . They hypothesized that this was caused by the increased stiffness of the asphalt. Schubert and coworkers [6] discovered that the bridge's deflection was independent of the asphalt's stiffness. Only the mass of the asphalt contributed to the deflection. However, the team discovered that the asphalt pavement considerably affected the dynamic behavior of the bridge. Both damping and dynamic stiffness was affected by the high shear transfer between the deck and the asphalt. Lastly, the team studied the temperature dependency of the dynamic properties. Natural frequencies increased while damping ratios decreased as temperatures decreased. Weber [11] studied damping ratios of bridges with and without asphalt. He discovered that the asphalt pavement significantly increased the damping ratio and measured damping ratios in excess of 3% at 0°C for a timber bridge with a span length of 20 meters.

Weber [11] studied the influence of support conditions on the estimated natural frequencies of footbridges. Two support conditions were modelled; simply supported and pinned at both ends. Before the asphalt pavement was added, the measured natural frequencies lied somewhere between the results from the models with the two different support conditions. However, results after the introduction of the asphalt pavement, clearly indicated that the pinned-pinned boundary condition yielded superior approximations of the natural frequencies.

The availability of computational power has soared in recent times. This enables the use of new, computational heavy modal analysis techniques. This thesis will focus on three

output-only modal analysis techniques; Basic Frequency Domain (BFD), Covariance-Driven Stochastic Subspace Identification (SSI-Cov), and Data-Driven Stochastic Subspace Identification (SSI-DD). BFD simply analyzes the frequency content of the data and may therefore be applied to an arbitrary data set. Stochastic Subspace Identification (SSI) methods, on the other hand, require white noise as input. This thesis will utilize the SSI methods on forced vibrations induced by a roving hammer. Forced vibrations have been proven to provide better modal identification, but ambient vibrations tend to be preferred due to the low cost and simplicity [12]. Employing SSI methods for non-white noise data has previously been done when analyzing the damping in railway catenary wire systems which analyzed time series moments after trains had passed the sampling positions with SSI-Cov [13]. Magalhães and coworkers [14] compared damping ratios estimated from forced and ambient excitation by employing SSI-Cov and SSI-DD. The team concluded that the SSI methods yielded reliable estimates of the damping ratios from the forced excitation.

1.3 Research Questions

- *Can the implementation of rotational stiffness improve the accuracy of the FEM model?*
- *Does the estimated asphalt contribution yield accurate results from the FEM model?*
- *Can SSI methods be used to analyze non white noise data from a Modal Hammer Test?*
- *What differences are there between the three operational modal analysis techniques?*
- *What are the pros and cons of the three operational modal analysis techniques?*

1.4 Thesis Outline

Chapter 2: gives a general introduction to SLT decks.

Chapter 3: describes all theory used in this thesis. The chapter derives the modal analysis techniques, presents method for modal comparison, presents functions to estimate the material properties of asphalt, and defines human-induced frequencies.

Chapter 4: describes how the acceleration data was collected and analyzed and describes how the bridges were modelled in ABAQUS.

Chapter 5: gives a geometric description of the analyzed bridges.

Chapter 6: presents and discusses the results.

Chapter 7: concludes the results and proposes further work.

Appendix A: contains the Python script used for the ABAQUS model.

Appendix B: describes the content of the digital appendix.

1.5 Limitations

The data analyzed in this master's thesis, was gathered Sigve and Lavina during the spring of 2021. Therefore, there is no way to confirm that the measurements were conducted correctly. Additionally, each test was only performed once, which eliminates the possibility of comparing results across data sets. Conducting several tests could mitigate errors caused by noise and act to verify that the tests were properly conducted.

Asphalt pavement's material properties are highly temperature dependent. Since the bridges were analyzed on the same day, they were analyzed for similar temperatures. This makes it impossible to check whether the formula for the asphalt's elastic modulus yields realistic natural frequencies and mode shapes for other temperatures. Preferably, the bridges should have been analyzed for several temperatures to properly verify the model. This would also enable us to investigate the temperature dependency of the optimal rotational stiffness. The temperature was solely recorded for one of the bridges. It's difficult to predict the temperature of the asphalt for the bridge where the temperature wasn't recorded. Historical temperatures of the area was utilized to estimate that the temperature of the asphalt was approximately $3^{\circ}C$.

Computational power limited the calculations. Both computers used in thesis had 8 GB of RAM available. The computers were not able to run the SSI methods for the entire Modal Hammer Test time series for a sufficient number of block rows. A truncated time series had to be constructed to increase the number of block rows utilized. The available computational power also limited the mesh size of the ABAQUS model. The model was limited to six elements in the vertical direction of the SLT deck.

Chapter 2

Stress-laminated Timber Bridges

Stress-laminated Timber (SLT) bridges are cost-effective options for conventional short and medium span bridges [15]. The SLT bridge deck consists of planks or glulam beams compressed together by high-strength steel bars. The friction caused by the compressive forces enables load transfer between the individual beams [16]. This results in the entire deck behaving as an orthotropic plate. A SLT bridge located in Holmenkollen, Norway is shown in figure 2.1.



Figure 2.1: Example of a SLT bridge in Holmenkollen [17].

Stress-laminated Timber decks originate from 1970s Canada [18]. Engineers wanted to rehabilitate longitudinal nail-laminated decks and placed bars over and under the decks in order to prevent separation. It was discovered that post-tensioning the bars greatly improved the load distribution of the decks. This discovery gave birth to the SLT decks used today. Typically, the steel rods are placed with a spacing of 600 to 900 mm. If the deck has a

thickness greater than 500 mm, two or more pre-stressed bars are placed vertically to ensure a uniform compressive force acting between the beams [15]. The bars are threaded through pre-drilled holes and tensioned sufficiently to avoid slip between the laminates. Relaxation of the steel bars will eventually result in a reduction of pre-stressed force. Ekholm [19] discovered that little pre-stressing force was necessary for the SLT deck to act as a plate. Long term effects of the prestressing has been shown to be as high as 60% [20]. Given that the standard defines the minimum pre-stressed force to be 0.35 MPa [8], it's common practice to apply an initial pre-stressing force of 1 MPa [15].

Timber beams are limited in length resulting in beams requiring to be joined together in decks with longer span lengths [15]. These joints are called butt-joints and weaken the SLT deck. To minimize this weakness, the standard defines a minimum spacing for butt-joints in any four adjacent beams [8]. Figure 2.2 shows a typical composition of a SLT deck with butt-joints.

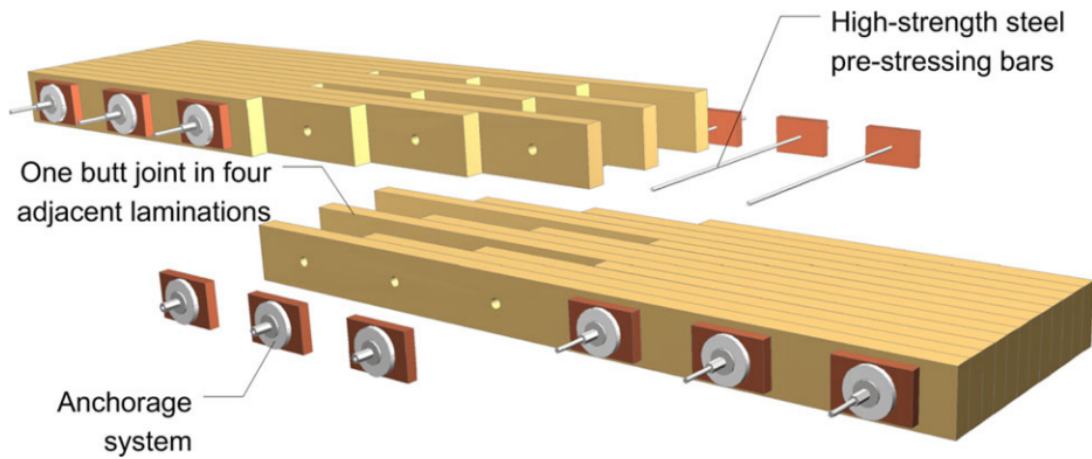


Figure 2.2: Sketch of butt-joints in a SLT deck [19].

SLT decks are renowned for their speed of manufacture and ease of assembly. Combined with their great adaptability, SLT bridges may be formed using complicated geometries. Given that a membrane is placed on top of the SLT deck, the bridge normally does not experience any significant expansion or contraction induced by moisture [15]. Timber is, as previously stated, considered a carbon neutral material [21].

Chapter 3

Theory

3.1 State-space Model

The dynamic behavior of a general *Multi-degree of Freedom* system, subjected to a loading vector $\{f(t)\}$, is governed by the *Equation of Motion* given by equation (3.1) [22].

$$[M] \{\ddot{y}(t)\} + [C] \{\dot{y}(t)\} + [K] \{y(t)\} = \{f(t)\} \quad (3.1)$$

The second order differential equation is converted to a sytem of first order differential equations by introducing the *State-Space Model*. The first step of the manipulation is to factorize the loading vector $\{f(t)\}$ into two different parts as follows:

$$\{f(t)\} = [\bar{B}] \{u(t)\} \quad (3.2)$$

where the matrix $[\bar{B}]$ defines the spatial distribution of inputs and $\{u(t)\}$ is the time variant part of the loading. Substituting the factorized loading vector from equation (3.2) into the Equation of Motion and pre-multiplying by $[M]^{-1}$, results into equation (3.3).

$$\{\ddot{y}(t)\} + [M]^{-1} [C] \{\dot{y}(t)\} + [M]^{-1} [K] \{y(t)\} = [M]^{-1} [\bar{B}] \{u(t)\} \quad (3.3)$$

Equation (3.3) may be rewritten as a system of equations as follows:

$$\begin{cases} \{\ddot{y}(t)\} = -[M]^{-1} [C] \{\dot{y}(t)\} - [M]^{-1} [K] \{y(t)\} + [M]^{-1} [\bar{B}] \{u(t)\} \\ \{\dot{y}(t)\} = [I] \{\dot{y}(t)\} \end{cases} \quad (3.4)$$

$$\begin{Bmatrix} \{\ddot{y}(t)\} \\ \{\dot{y}(t)\} \end{Bmatrix} = \begin{bmatrix} -[M]^{-1} [C] & -[M]^{-1} [K] \\ [I] & [0] \end{bmatrix} \begin{Bmatrix} \{\dot{y}(t)\} \\ \{y(t)\} \end{Bmatrix} + \begin{bmatrix} [M]^{-1} [\bar{B}] \\ [0] \end{bmatrix} \{u(t)\}. \quad (3.5)$$

By introducing the following *state-space vector*:

$$\{s(t)\} = \begin{Bmatrix} \{\dot{y}(t)\} \\ \{y(t)\} \end{Bmatrix} \quad (3.6)$$

and substituting it into equation (3.5), the system of equations may be simplified to the first order expression presented in equation (3.7).

$$\{\dot{s}(t)\} = \begin{bmatrix} -[M]^{-1} [C] & -[M]^{-1} [K] \\ [I] & [0] \end{bmatrix} \{s(t)\} + \begin{bmatrix} [M]^{-1} [\bar{B}] \\ [0] \end{bmatrix} \{u(t)\} \quad (3.7)$$

The *state matrix*, $[A_c]$, and the *input influence matrix*, $[B_c]$, are defined in equation (3.8), where the subscript "c" denotes continuous time.

$$\begin{aligned} [A_c] &= \begin{bmatrix} -[M]^{-1} [C] & -[M]^{-1} [K] \\ [I] & [0] \end{bmatrix} \\ [B_c] &= \begin{bmatrix} [M]^{-1} [\bar{B}] \\ [0] \end{bmatrix} \end{aligned} \quad (3.8)$$

The *state equation*, equation (3.7), can consequently be simplified into equation (3.9).

$$\{\dot{s}(t)\} = [A_c] \{s(t)\} + [B_c] \{u(t)\} \quad (3.9)$$

The *observation equation* is derived to tie the state-space $\{s(t)\}$ to the measured outputs $\{y_l(t)\}$. The subscript "l" denotes the amount of sensors used to measure the acceleration, velocity, and displacement. The most general case of the observation equation may be expressed as:

$$\{y_l(t)\} = [C_a] \{\ddot{y}(t)\} + [C_v] \{\dot{y}(t)\} + [C_d] \{y(t)\} \quad (3.10)$$

$\{y_l(t)\}$ is the vector of measured outputs. The three matrices $[C_a]$, $[C_v]$ and $[C_d]$ are the output location matrices for acceleration, velocity, and displacement, respectively. By substituting the acceleration vector from equation (3.3) into equation (3.10), the observation equation may be written as illustrated in equation (3.11).

$$\begin{aligned} \{y_l(t)\} &= ([C_v] - [C_a] [M]^{-1} [C]) \{\dot{y}(t)\} \\ &\quad + ([C_d] - [C_a] [M]^{-1} [K]) \{y(t)\} \\ &\quad + ([C_a] [M]^{-1} [\bar{B}]) \{u(t)\}. \end{aligned} \quad (3.11)$$

By defining the *output influence matrix* $[C_c]$ and the *direct transmission matrix* $[D_c]$ as follows:

$$[C_c] = \begin{bmatrix} [C_v] - [C_a] [M]^{-1} [C] & [C_d] - [C_a] [M]^{-1} [K] \end{bmatrix} \quad (3.12)$$

$$[D_c] = [C_a] [M]^{-1} [\bar{B}] \quad (3.13)$$

the observation equation can be expressed as shown in equation (3.14).

$$\{y(t)\} = [C_c] \{s(t)\} + [D_c] \{u(t)\} \quad (3.14)$$

Converting to discrete time

In order to use the state-space model for data from experimental tests, the continuous-time state-space model must be converted into a discrete-time model. This is due to the the available data being finite and discrete. Given a sampling frequency, F_s , the continuous-time system equations can be solved at any discrete time instant, $t_k = \frac{k}{F_s} = k\Delta t$, for $k = 0, 1, 2, \dots$ and $\Delta t = \frac{1}{F_s}$. The *Zero Order Hold* is employed to perform the conversion from continuous to discrete time. This conversion implies that the input is assumed piecewise constant. The conversion is presented in the following equations:

$$\begin{aligned} [A] &= e^{[A_c]\Delta t} \\ [B] &= ([A] - [I])[A_c]^{-1}[B_c] \\ [C] &= [C_c] \\ [D] &= [D_c] \end{aligned} \tag{3.15}$$

where $[A]$ is the *discrete state matrix*, $[B]$ is the *discrete input influence matrix*, $[C]$ is the *discrete output influence matrix*, and $[D]$ is the *discrete direct transmission matrix*. The Zero Order Hold and other relations between continuous- and discrete-time state-space systems can be found in [23]. The discrete-time state-space model equations can consequently be written as presented in equation (3.16).

$$\begin{cases} \{s_{k+1}\} = [A]\{s_k\} + [B]\{u_k\} \\ \{y_k\} = [C]\{s_k\} + [D]\{u_k\} \end{cases} \tag{3.16}$$

The deterministic model presented in the equation above is solely driven by the deterministic input $\{u\}$. A stochastic noise term is added to the system of equations in order to convert the system into a *discrete-time combined deterministic-stochastic state-space model* as shown below:

$$\begin{cases} \{s_{k+1}\} = [A]\{s_k\} + [B]\{u_k\} + \{w_k\} \\ \{y_k\} = [C]\{s_k\} + [D]\{u_k\} + \{v_k\} \end{cases} \tag{3.17}$$

where $\{w_k\}$ is the *process noise* due to disturbance and modal inaccuracies while $\{v_k\}$ is the *measurement noise* due to internal measurement errors from the sensors.

This report will solely study output-only Operational Modal Analysis (OMA) since the loading input is assumed unknown. Equation (3.17) may be rewritten into a *discrete-time stochastic state-space model* driven by the two noise components; $\{w_k\}$ and $\{v_k\}$. This simplification is simply performed by neglecting the input vector resulting in the process solely being driven by noise. The noise inputs are assumed to be zero mean, stationary white noise.

$$\begin{cases} \{s_{k+1}\} = [A]\{s_k\} + \{w_k\} \\ \{y_k\} = [C]\{s_k\} + \{v_k\} \end{cases} \tag{3.18}$$

Defining covariance terms

The response in the state-space model is assumed to be a *zero mean Gaussian process*. In order to represent the statistical properties of the system response, the covariance terms are essential as given in [24]. The covariance for a given *time-lag*, "i", is calculated as illustrated in equation (3.19).

$$[R_i] = E[\{y_{k+i}(t)\}\{y_k(t)\}^T] \quad (3.19)$$

Similarly to the the noise input, the state is also assumed to be a zero mean Gaussian process described by its covariance illustrated in equation (3.20).

$$[\Sigma] = E[\{s_k(t)\}\{s_k(t)\}^T] \quad (3.20)$$

The state is assumed to be uncorrelated to the process noise and the measurement noise. The following criteria must therefore be fulfilled:

$$\begin{aligned} E[\{s_k(t)\}\{w_k(t)\}^T] &= [0] \\ E[\{s_k(t)\}\{v_k(t)\}^T] &= [0]. \end{aligned} \quad (3.21)$$

For further calculations the following matrices need to be defined; the *process noise covariance matrix* ($[Q^{ww}]$), the *measurment noise covariance matrix* ($[R^{vv}]$), and the *process-measurment noise covariance matrix* ($[S^{wv}]$). The matrices are defined in the equation below.

$$\begin{aligned} [Q^{ww}] &= E[\{w_k(t)\}\{w_k(t)\}^T] \\ [R^{vv}] &= E[\{v_k(t)\}\{v_k(t)\}^T] \\ [S^{wv}] &= E[\{w_k(t)\}\{v_k(t)\}^T] \end{aligned} \quad (3.22)$$

Lastly, the *next state-output covariance matrix* is defined. This matrix represents the covariance between the response vector and the updated state vector. The matrix is defined in equation (3.23).

$$[G] = E[\{s_{k+1}\}\{y_k\}^T] \quad (3.23)$$

Rewriting expressions

In order to apply the different versions of the state-space model, certain expressions need to be rewritten. The state covariance expressed in equation (3.20) may be rewritten by substituting the state vector with the expression for the state vector expressed in the discrete-time stochastic state space model, equation (3.18).

$$\begin{aligned}
[\Sigma] &= E[\{s_k(t)\}\{s_k(t)\}^T] \\
&= E[([A]\{s_{k-1}\} + \{w_{k-1}\}) ([A]\{s_{k-1}\} + \{w_{k-1}\})^T] \\
&= [A]E[\{s_{k-1}(t)\}\{s_{k-1}(t)\}^T][A]^T + [A]E[\{s_{k-1}(t)\}\{w_{k-1}(t)\}^T] \\
&\quad + E[\{w_{k-1}(t)\}\{s_{k-1}(t)\}^T][A]^T + E[\{w_{k-1}(t)\}\{w_{k-1}(t)\}^T] \\
&= [A][\Sigma][A]^T + [A][0] + [0][A]^T + [Q^{ww}] \\
&= [A][\Sigma][A]^T + [Q^{ww}]
\end{aligned} \tag{3.24}$$

The next-state output covariance matrix may be rewritten by inserting the functions in equation (3.18) into equation (3.23). This results in the function expressed in equation (3.25).

$$\begin{aligned}
[G] &= E[\{s_{k+1}\}\{y_k\}^T] \\
&= E[([A]\{s_k\} + \{w_k\}) ([C]\{s_k\} + \{v_k\})^T] \\
&= [A]E[\{s_k(t)\}\{s_k(t)\}^T][C]^T + [A]E[\{s_k(t)\}\{v_k(t)\}^T] \\
&\quad + E[\{w_k(t)\}\{s_k(t)\}^T][C]^T + E[\{w_k(t)\}\{v_k(t)\}^T] \\
&= [A][\Sigma][C]^T + [A][0] + [0][C]^T + [S^{wv}] \\
&= [A][\Sigma][C]^T + [S^{wv}]
\end{aligned} \tag{3.25}$$

The covariance matrix for the system response, $[R_i]$, may be rewritten in terms of $[A]$, $[C]$, and $[G]$. This is done by substituting the response in equation (3.19) with the expression from the discrete stochastic state-space model, equation (3.18).

$$[R_i] = E[([C]\{s_{k+i}\} + \{v_{k+i}\}) ([C]\{s_k\} + \{v_k\})^T] \tag{3.26}$$

The term $\{s_{k+i}\}$ may be rewritten into the following expression:

$$\{s_{k+i}\} = [A]^i \{s_k\} + \sum_{n=0}^{i-1} [A]^{(i-1)-n} \{w_{k+n}\}. \tag{3.27}$$

By combining the two expressions from equation (3.26) and equation (3.27), the following expression may be derived:

$$\begin{aligned}
[R_i] &= E \left[\left([C]([A]^i \{s_k\} + \sum_{n=0}^{i-1} [A]^{(i-1)-n} \{w_{k+n}\}) + \{v_{k+i}\} \right) \left([C] \{s_k\} + \{v_k\} \right)^T \right] \\
&= [C][A]^i E[\{s_k(t)\} \{s_k(t)\}^T] [C]^T + [C][A]^i E[\{s_k(t)\} \{v_k(t)\}^T] \\
&\quad + [C] E \left[\left(\sum_{n=0}^{i-1} [A]^{(i-1)-n} \{w_{k+n}\} \right) \{s_k\}^T \right] [C]^T + [C] E \left[\left(\sum_{n=0}^{i-1} [A]^{(i-1)-n} \{w_{k+n}\} \right) \{v_k\}^T \right] \\
&\quad + E[\{v_{k+i}(t)\} \{s_k(t)\}^T] [C]^T + E[\{v_{k+i}(t)\} \{v_k(t)\}^T] \\
&= [C][A]^i [\Sigma] [C]^T + [C][A]^i [0] \\
&\quad + [C] \sum_{n=0}^{i-1} ([A]^{(i-1)-n} [0]) [C]^T + [C][A]^{i-1} E[\{w_k(t)\} \{v_k(t)\}^T] + [C] \sum_{n=1}^{i-1} ([A]^{(i-1)-n} [0]) \\
&\quad + [0] [C]^T + [0] \\
&= [C][A]^i [\Sigma] [C]^T + [C][A]^{i-1} [S^{wv}] \\
&= [C][A]^{i-1} \left([A] [\Sigma] [C]^T + [S^{wv}] \right) \\
&= [C][A]^{i-1} [G].
\end{aligned} \tag{3.28}$$

3.1.1 Stochastic Subspace Identification

Stochastic Subspace Identification (SSI) is an elegant modal analysis method in the time domain [25]. This thesis will study two central implementations of SSI; Covariance-Driven Stochastic Subspace Identification (SSI-Cov) and Data-Driven Stochastic Subspace Identification (SSI-DD). These two output-only modal identification methods seek to determine the state matrix, $[A]$, and the output matrix, $[C]$, introduced in section 3.1. These matrices are then used to identify the dynamic properties of the structure.

Covariance-Driven Stochastic Subspace Identification (SSI-Cov)

The SSI-Cov method addresses the stochastic realization problem, the problem of identifying a stochastic state-space model solely based on output data. This method utilizes *Singular Value Decomposition (SVD)* which results in the method being able to effectively treat noisy data [26]. The model is based upon the concept of minimal realization. This concept seeks to identify the minimal state-space dimension required for all modes to be appropriately excited and can be applied to systems with unit covariance and white noise input [27]. If the model order is too low, information about the structure will be lost. Orders that are too high result in redundant information [24].

In order to make a model with a minimal state-space dimension, it's essential to ensure that the system states of the model can be controlled and observed. These attributes are checked through the implementation of the observability ($[O]$) and controllability matrices. This report will, however, not compute the controllability matrix, but rather the reversed controllability matrix ($[\Gamma]$). A controllable system is defined as a system where a state can be

reached independently of the initial state of the system. The system is observable if the state is completely determined by the input and output. A system of order n is controllable and observable if and only if the criteria stated in equation (3.29) are fulfilled.

$$\begin{aligned} \text{Rank}([O]) &= n \\ \text{Rank}([\Gamma]) &= n \end{aligned} \quad (3.29)$$

In practice, the order of the system, n , is unknown, and identifying the correct order tends to be excessively complicated. To overcome this issue, the order of the system is overestimated. This results in spurious poles that later need to be identified and removed.

The SSI-Cov method starts by defining the correlations of the output data as shown in equation (3.30).

$$[\hat{R}_i] = \frac{1}{N-i} [Y_{1:N-i}] [Y_{i:N}^T] \quad (3.30)$$

$[Y]$ is the output data stored in an $l \times N$ matrix where l is the total amounts of observation points and N is the number of sampling points. The calculated unbiased correlation matrices with a time lag equal to the number of block rows, " i ", are collected in the *Toeplitz matrix* shown in equation (3.31).

$$[T_{1|i}] = \begin{bmatrix} [\hat{R}_i] & [\hat{R}_{i-1}] & \dots & [\hat{R}_1] \\ [\hat{R}_{i+1}] & [\hat{R}_i] & \dots & [\hat{R}_2] \\ \vdots & \vdots & \ddots & \vdots \\ [\hat{R}_{2i-1}] & [\hat{R}_{2i-2}] & \dots & [\hat{R}_i] \end{bmatrix} \quad (3.31)$$

The Toeplitz matrix has dimensions $li \times li$. The dimensions of this matrix need to be larger than the order of the system, n . Therefore, the following condition needs to be fulfilled:

$$li \geq n. \quad (3.32)$$

Equation (3.28) illustrates how the correlations are related to the $[C]$, $[A]$ and $[G]$ matrices. Substituting this relation into the Toeplitz matrix in equation (3.31) yields equation (3.33).

$$[T_{1|i}] = \begin{bmatrix} [C] \\ [C][A] \\ \vdots \\ [C][A]^{i-1} \end{bmatrix} \begin{bmatrix} [A]^{i-1}[G] & \dots & [A][G] & [G] \end{bmatrix} = [O_i][\Gamma_i] \quad (3.33)$$

The observability matrix ($[O]$) has dimensions $li \times n$ while the reversed controllability matrix ($[\Gamma]$) has dimensions $n \times li$. If the system is observable and controllable in combination with $li \geq n$, the Toeplitz matrix is of rank n . The controllability and observability matrices are

estimated by employing SVD on the Toeplitz matrix. The result can be rewritten as shown in equation (3.34) [24]. An in-dept explanation of the SVD can be found in [28].

$$[T_{1|i}] = [U][\Sigma][V]^T = \begin{bmatrix} [U_1] & [U_2] \end{bmatrix} \begin{bmatrix} [\Sigma_1] & [0] \\ [0] & [\Sigma_2 = 0] \end{bmatrix} \begin{bmatrix} [V_1]^T \\ [V_2]^T \end{bmatrix} \quad (3.34)$$

$[\Sigma]$ is a sorted, diagonal matrix. The equation above separates the non-zero singular values from the zero singular values on the diagonal of $[\Sigma]$. This clearly illustrates that the Toeplitz matrix is independent of $[U_2]$ and $[V_2]^T$, and can thus be omitted in further calculations. Equation (3.34) can therefore be simplified and written as shown in equation (3.35) [24].

$$[T_{1|i}] = [U_1][\Sigma_1][V_1]^T = [O_i][\Gamma_i] \quad (3.35)$$

By splitting the equation above, the following expressions can be derived:

$$\begin{aligned} [O_i] &= [U_1][\Sigma_1]^{\frac{1}{2}}[T] \\ [\Gamma_i] &= [T]^{-1}[\Sigma_1]^{\frac{1}{2}}[V_1]^T. \end{aligned} \quad (3.36)$$

$[T]$ is simply a transformation matrix applied to the state-space model. The attributes are independent of this transformation matrix, and will therefore be assumed to be the identity matrix in further calculations.

The $[A]$ matrix may be derived by defining a new, shifted Toeplitz matrix as shown in equation (3.37).

$$\begin{aligned} [T_{2|i+1}] &= \begin{bmatrix} [\hat{R}_{i+1}] & [\hat{R}_i] & \dots & [\hat{R}_2] \\ [\hat{R}_{i+2}] & [\hat{R}_{i+1}] & \dots & [\hat{R}_3] \\ \vdots & \vdots & \ddots & \vdots \\ [\hat{R}_{2i}] & [\hat{R}_{2i-1}] & \dots & [\hat{R}_{i+1}] \end{bmatrix} = \begin{bmatrix} [C] \\ [C][A] \\ \vdots \\ [C][A]^{i-1} \end{bmatrix} \begin{bmatrix} [A]^i[G] & \dots & [A]^2[G] & [A][G] \end{bmatrix} \\ &= [O_i][A][\Gamma_i] \end{aligned} \quad (3.37)$$

By rewriting equation (3.37) the following expression for $[A]$ can be derived:

$$[A] = [O_i]^+[T_{2|i+1}][\Gamma_i]^+ = [\Sigma_1]^{-\frac{1}{2}}[U_1]^T[T_{2|i+1}][V_1][\Sigma_1]^{-\frac{1}{2}} \quad (3.38)$$

where the notation " + " denotes the Moore-Penrose *pseudo-inverse* of a matrix which enables non-quadratic matrices to be inverted. Lastly, the $[C]$ matrix may be directly extracted from the Observability matrix defined in equation (3.36).

Data-Driven Stochastic Subspace Identification (SSI-DD)

SSI-DD identifies the state-matrices directly from raw data through the use of an elegant mathematical framework and robust linear algebra tools [24]. Compared to other data driven methods, SSI-DD avoids nonlinear optimization by reducing the optimization to a simple least square problem. Additionally, SSI-DD is a numerically efficient implementation due to the use of well-known mathematical tools such as Singular Value Decomposition and Orthogonal Decomposition into Lower Trapezoidal matrices (LQ).

The state sequence is estimated prior to the estimation of the state-space matrices [29]. The states are calculated directly from measurements using orthogonal projection. $[\Pi_E]$ denotes the operator that projects the row space of an arbitrary matrix onto the row space of the reference matrix, $[E]$, as shown in equation (3.39).

$$[\Pi_E] = [E]^T \left([E][E]^T \right)^+ [E] \quad (3.39)$$

The orthogonal projection of a generic matrix $[H]$ is derived as follows [24]:

$$[H]/[E] = [H][\Pi_E] = [H][E]^T \left([E][E]^T \right)^+ [E]. \quad (3.40)$$

The fundamental idea of this method, is that Kalman filter state estimates can be obtained from the raw data held in certain block *Hankel* matrices. The Kalman filter is regarded as an optimal predictor of the state space s_k given all previous states. The Kalman filter state sequence collects all the state estimates for the previous "i" time instants starting at "j" different time instants using the raw data. The estimates are stored as shown in equation (3.41) where each column represents one of the state estimates.

$$[\hat{S}_i] = [\{\hat{s}_i\} \ \{\hat{s}_{i+1}\} \ \dots \ \{\hat{s}_{i+j-1}\}] \quad (3.41)$$

SSI-DD starts by defining a block Hankel matrix containing all raw data as illustrated in equation (3.42). The block Hankel matrix has dimensions $2li \times j$, where it's assumed that $j \rightarrow \infty$. For all practical applications, j is set equal to $N - 2i + 1$.

$$\left[H_{0|2i-1} \right]_{2li \times j} = \frac{1}{\sqrt{j}} \begin{bmatrix} \{y_0\} & \{y_1\} & \dots & \{y_{j-1}\} \\ \{y_1\} & \ddots & \ddots & \{y_j\} \\ \vdots & \ddots & \ddots & \vdots \\ \{y_{i-1}\} & \{y_i\} & \dots & \{y_{i+j-2}\} \\ \{y_i\} & \{y_{i+1}\} & \dots & \{y_{i+j-1}\} \\ \{y_{i+1}\} & \ddots & \ddots & \{y_{i+j}\} \\ \vdots & \ddots & \ddots & \vdots \\ \{y_{2i-1}\} & \{y_{2i}\} & \dots & \{y_{2i+j-2}\} \end{bmatrix}_{2li \times j} = \begin{bmatrix} [Y_{0|i-1}] \\ [Y_{i|2i-1}] \end{bmatrix} = \begin{bmatrix} [Y_p] \\ [Y_f] \end{bmatrix} \quad (3.42)$$

Equation (3.42) divides the raw data into two sub-matrices; the past output matrix ($[Y_p]$) and the future output matrix ($[Y_f]$). For future calculations, another separation of the block

Hankel matrix is required. Equation (3.43) shifts the past and future output matrices by one row.

$$\left[H_{0|2i-1} \right]_{2li \times j} = \begin{bmatrix} \frac{[Y_{0|i-1}]}{[Y_{i|i}]} \\ \frac{[Y_{i+1|2i-1}]}{[Y_{i+1|2i-1}]} \end{bmatrix} = \begin{bmatrix} \frac{[Y_{0|i}]}{[Y_{i+1|2i-1}]} \end{bmatrix} \begin{bmatrix} \frac{[Y_p]^+}{[Y_f]^-} \end{bmatrix} \quad (3.43)$$

The future output matrix is orthogonally projected onto the past output matrix as shown below:

$$[P_i]_{(2li-i) \times j} = [Y_f][Y_p]^T \left([Y_p][Y_p]^T \right)^+ [Y_p]. \quad (3.44)$$

However, the orthogonal projection above may be more efficiently computed using Orthogonal Decomposition into Lower Trapezoidal matrices factorization of the block Hankel matrix, $[H_{0|2i-1}]$.

$$\left[H_{0|2i-1} \right]_{2li \times j} = [L][Q] = \begin{bmatrix} [L_{11}] & [0] & [0] \\ [L_{21}] & [L_{22}] & [0] \\ [L_{31}] & [L_{32}] & [L_{33}] \end{bmatrix} \begin{bmatrix} [Q_1] \\ [Q_2] \\ [Q_3] \end{bmatrix} \quad (3.45)$$

It can be proven that the orthogonal projections of $[Y_f]$ and $[Y_f^-]$ onto $[Y_p]$ and $[Y_p^+]$ may be rewritten in terms of the matrices calculated in equation (3.45) as shown below:

$$[P_i] = [Y_f]/[Y_p] = \begin{bmatrix} [L_{21}] \\ [L_{31}] \end{bmatrix} [Q_1] \quad (3.46)$$

$$[P_{i-1}] = [Y_f^-]/[Y_p^+] = \begin{bmatrix} [L_{31}] & [L_{31}] \end{bmatrix} \begin{bmatrix} [Q_1] \\ [Q_2] \end{bmatrix}. \quad (3.47)$$

The output sequence, $[Y_{i|i}]$, may be estimated as follows:

$$[Y_{i|i}] = \begin{bmatrix} [L_{21}] & [L_{22}] \end{bmatrix} \begin{bmatrix} [Q_1] \\ [Q_2] \end{bmatrix}. \quad (3.48)$$

Assuming that the system is controllable, observable, and the conditions expressed in equation (3.32) are satisfied, the projection matrix may be factorized into the observability matrix, $[O_i]$, and the Kalman filter state sequence, $[\hat{S}_i]$. The observability matrix was previously defined in equation (3.33).

$$[P_i] = [O_i][\hat{S}_i] \quad (3.49)$$

Similarly, the shifted projection matrix, $[P_{i-1}]$, may be represented as follows:

$$[P_{i-1}] = [O_i^\uparrow][\hat{S}_{i+1}] \quad (3.50)$$

where $[O_i^\uparrow]$ is computed by removing the last l rows from the observability matrix.

The observability matrix and Kalman state sequence are computed by applying a Singular Value Decomposition on the projected matrix, $[P_i]$, and solely retaining the nonzero singular values [24].

$$[P_i] = [U][\Sigma][V]^T = \begin{bmatrix} [U_1] & [U_2] \end{bmatrix} \begin{bmatrix} [\Sigma_1] & [0] \\ [0] & [\Sigma_2 = 0] \end{bmatrix} \begin{bmatrix} [V_1]^T \\ [V_2]^T \end{bmatrix} = [U_1][\Sigma_1][V_1]^T \quad (3.51)$$

Equation (3.51) allows for the following calculations:

$$[O_i] = [U_1][\Sigma_1]^{\frac{1}{2}}[T] \quad (3.52)$$

$$[\hat{S}_i] = [O_i]^+ [P_i]. \quad (3.53)$$

Equation (3.50) may be rewritten into the following equation:

$$[\hat{S}_{i+1}] = [O_i^\dagger]^+ [P_{i-1}]. \quad (3.54)$$

Once the state sequences $[\hat{S}_i]$ and $[\hat{S}_{i+1}]$ have been determined as shown in equation (3.51) and (3.54), the state matrices $[A]$ and $[C]$ may be determined:

$$\begin{bmatrix} [\hat{S}_{i+1}] \\ [Y_{i|i}] \end{bmatrix} = \begin{bmatrix} [A] \\ [C] \end{bmatrix} [\hat{S}_i] + \begin{bmatrix} [\rho_w] \\ [\rho_v] \end{bmatrix} \quad (3.55)$$

The residuals from the Kalman filter $[\rho_w]$ and $[\rho_v]$ are orthogonal and thus uncorrelated with $[S_i]$ [29]. Therefore, it's natural to solve the set of equations above in a least square sense. It can be proven that equation (3.56) is an unbiased estimate of the state matrices [30].

$$\begin{bmatrix} [A] \\ [C] \end{bmatrix} = \begin{bmatrix} [\hat{S}_{i+1}] \\ [Y_{i|i}] \end{bmatrix} [\hat{S}_i]^+ \quad (3.56)$$

Processing the state matrices

Once the state matrices $[A]$ and $[C]$ are derived using either SSI-Cov or SSI-DD, the natural frequencies, mode shapes, and modal damping ratios can be derived [25]. Firstly, the eigenvectors (Ψ) and eigenvalues (Λ) of the matrix $[A]$ are calculated:

$$[A] = \Psi \Lambda \Psi^{-1}. \quad (3.57)$$

Λ is a diagonal matrix containing the eigenvalues, λ_k . The state matrices are calculated for discrete time and need to be converted to continuous time. The conversion of the matrices $[A]$ and $[C]$ is illustrated in equation (3.15). This results in the following expressions for the mode shapes and natural frequencies of the structure:

$$f_k = \frac{|\lambda_{ck}|}{2\pi}, \text{ where } \lambda_{ck} = \frac{\ln \lambda_k}{\Delta t} \quad (3.58)$$

$$\phi_k = C\psi_k. \quad (3.59)$$

Lastly, the damping ratio can be derived:

$$\xi_k = -\frac{\text{Re}(\lambda_{ck})}{|\lambda_{ck}|} \cdot 100. \quad (3.60)$$

3.2 Stabilization Diagram

The model order needs to be determined when the SSI methods presented in section 3.1.1 are employed. Due to the presence of noise and modelling inaccuracies, it's difficult to precisely estimate the correct model order. The underestimation of the model order results in information loss, it is therefore preferred to overestimate the model order to ensure the identification of all modes, as stated in section 3.1.1. The overestimation of the model order will, on the other hand, result in spurious poles that need to be identified and removed. There are many criteria that can be implemented to identify the spurious poles [24]. The criteria used to filter poles in this paper are presented in equation (3.61). Note that MAC is further explained in section 3.5. Additional filtering criteria may be introduced. These criteria are further explained in [31].

$$\begin{aligned} \frac{|f_n - f_{n-1}|}{f_n} &\leq 0.01 \\ \frac{|\xi_n - \xi_{n-1}|}{\xi_n} &\leq 0.05 \\ 1 - \text{MAC}(\{\phi_n\}, \{\phi_{n-1}\}) &\leq 0.02 \end{aligned} \quad (3.61)$$

A stabilization diagram compares poles calculated for different model orders [24]. The y-axis indicates the model order, while the x-axis indicates the natural frequency of the calculated poles. Each pole is filtered using the filtering criteria presented in equation (3.61). If all criteria are met, the pole is plotted as a green dot, otherwise the pole is plotted with the color red.

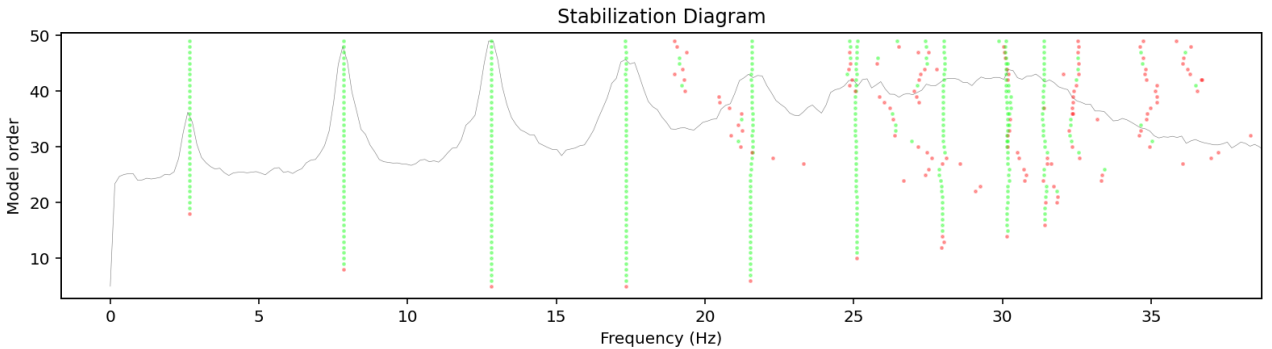


Figure 3.1: An example of a stabilization diagram of a nine-story shear frame with PSD in the background for comparison.

The stabilization diagram seeks to identify the physical modes from the alignment of the stable poles of different model orders. Spurious modes tend to be scattered and typically don't stabilize. Low model orders may result in bias towards certain modes. This is typically caused by the order being too low to separate closely spaced modes.

3.3 Basic Frequency Domain Method

The Basic Frequency Domain (BFD) is an undemanding method of modal analysis in the frequency domain [32]. To begin with, the data is transformed from the time domain into the frequency domain by employing the Discrete Fourier Transform (DFT). A discrete time series, $\{y_0, y_1, \dots, y_{N-1}\}$, is transformed into a sequence of exponential terms, $\{Y_0, Y_1, \dots, Y_{N-1}\}$, by applying DFT as illustrated by the following expression:

$$Y_k = Y(\omega_k) = \sum_{n=0}^{N-1} y_n \cdot e^{-i\omega_k n} \quad (3.62)$$

where $\omega_k = \frac{2\pi k}{N}$ for $k = 0, 1, 2, \dots, N-1$ and N is the number of samples in the time series.

By substituting *Euler's formula* into equation (3.62), the time series is expressed in terms of harmonic components in the frequency domain, as shown in equation (3.63).

$$Y_k = \sum_{n=0}^{N-1} y_n [\cos(\omega_k n) + i \sin(\omega_k n)] \quad (3.63)$$

The Power Spectral Density (PSD) is then computed using the following equation:

$$\{S_{y_i y_j}(\omega)\} = \frac{\{Y_i(\omega)\} \cdot \{Y_j^*(\omega)\}}{\Delta\omega} \quad (3.64)$$

where $\{Y_j^*(\omega)\}$ is the complex conjugate of $\{Y_j(\omega)\}$, $\Delta\omega = \frac{2\pi}{T}$ and T is the duration of the sampling process.

The auto-spectral densities for $\{S_{y_i y_i}(\omega)\}$ and $\{S_{y_j y_j}(\omega)\}$ are located on the diagonal of the resulted *Power Spectral Density matrix*, while the non-diagonal terms represent the cross-spectral densities. The natural frequencies are identified as the frequencies corresponding to the peaks of the auto-spectral densities. Mode shapes are estimated by the amplitudes of the peaks in the auto-spectral densities in combination with the signs from the cross-spectral densities.

Near the natural frequency ω_j , the physical degree of freedom $\{y_i\}$ at location $x = x_i$ can be approximated using *Single Mode Approximation* [33]:

$$\{y_i(t)\} \approx \phi_j(x_i) \{\eta_j(t)\} \quad (3.65)$$

where $\phi_j(x_i)$ is modal shape number j at location $x = x_i$ and $\eta_j(t)$ represents the generalized modal coordinates. Next, the second time derivative of $y_i(t)$ is derived:

$$\{\ddot{y}_i(t)\} \approx \phi_j(x_i) \{\ddot{\eta}_j(t)\} \quad (3.66)$$

Applying the Fourier transform on both sides, equation (3.67) is derived.

$$\{\ddot{Y}_i(\omega)\} \approx \phi_j(x_i)\{\ddot{H}_j(\omega)\} \quad (3.67)$$

By calculating the PSD of $\ddot{y}_i(t)$ and substituting for equation (3.67), the following expression can be derived:

$$\begin{aligned} \{S_{\ddot{y}_i\ddot{y}_i}(\omega)\} &\approx \frac{(\phi_j(x_i) \cdot \{\ddot{H}_j(\omega)\}) \cdot (\phi_j(x_i) \cdot \{\ddot{H}_j(\omega)\})^*}{\Delta\omega} \\ &\approx \phi_j(x_i)^2 \frac{\{\ddot{H}_j(\omega)\} \cdot \{\ddot{H}_j^*(\omega)\}}{\Delta\omega} \\ &\approx \phi_j(x_i)^2 \{S_{\ddot{\eta}_j\ddot{\eta}_j}(\omega)\} \end{aligned} \quad (3.68)$$

where:

$$\{S_{\ddot{\eta}_j\ddot{\eta}_j}(\omega)\} = \frac{\{\ddot{H}_j(\omega)\} \cdot \{\ddot{H}_j^*(\omega)\}}{\Delta\omega} \quad (3.69)$$

$S_{\ddot{\eta}_j\ddot{\eta}_j}(\omega)$ is the spectral density of the acceleration data in terms of the generalized degrees of freedom. The mode shape may be estimated by employing equation (3.68) for the natural frequency, ω_j . Firstly, the expressions for the PSD at location $x = x_1$ and $x = x_2$ near a frequency ω_j are defined:

$$S_{\ddot{y}_1\ddot{y}_1}(\omega_j) \approx \phi_j(x_1)^2 S_{\ddot{\eta}_j\ddot{\eta}_j}(\omega_j) \iff S_{\ddot{\eta}_j\ddot{\eta}_j}(\omega_j) \approx \frac{S_{\ddot{y}_1\ddot{y}_1}(\omega_j)}{\phi_j(x_1)^2} \quad (3.70)$$

$$S_{\ddot{y}_2\ddot{y}_2}(\omega_j) \approx \phi_j(x_2)^2 S_{\ddot{\eta}_j\ddot{\eta}_j}(\omega_j) \iff S_{\ddot{\eta}_j\ddot{\eta}_j}(\omega_j) \approx \frac{S_{\ddot{y}_2\ddot{y}_2}(\omega_j)}{\phi_j(x_2)^2}. \quad (3.71)$$

$S_{\ddot{\eta}_j\ddot{\eta}_j}(\omega_j)$ is a common term for both locations due to it solely being dependent on the frequency. The two equations above may therefore be rewritten as follows:

$$\frac{S_{\ddot{y}_1\ddot{y}_1}(\omega_j)}{\phi_j(x_1)^2} = \frac{S_{\ddot{y}_2\ddot{y}_2}(\omega_j)}{\phi_j(x_2)^2} \iff \frac{\phi_j(x_1)}{\phi_j(x_2)} = \sqrt{\frac{S_{\ddot{y}_1\ddot{y}_1}(\omega_j)}{S_{\ddot{y}_2\ddot{y}_2}(\omega_j)}}. \quad (3.72)$$

By assuming $\phi_j(x_1) = 1$, $\phi_j(x_2)$ is the only unknown and may be derived. The function for the absolute values of the mode shapes is presented below:

$$\{\phi_1\} = \left[\frac{1}{\sqrt{\frac{S_{\ddot{y}_2\ddot{y}_2}(\omega_1)}{S_{\ddot{y}_1\ddot{y}_1}(\omega_1)}}} \right], \{\phi_2\} = \left[\frac{1}{\sqrt{\frac{S_{\ddot{y}_2\ddot{y}_2}(\omega_2)}{S_{\ddot{y}_1\ddot{y}_1}(\omega_2)}}} \right]. \quad (3.73)$$

Lastly, the signs need to be identified. This is done by using the cross-spectral densities, as shown in equation (3.74).

$$\text{sign}(\phi_{ij}) = \text{sign}(S_{\ddot{y}_i\ddot{y}_j}(\omega_i)) \quad (3.74)$$

The final expression for the estimated mode shapes ϕ_1 and ϕ_2 are presented in equation (3.75) and (3.76).

$$\{\phi_1\} = \left[\begin{array}{cc} \text{sign}(S_{\dot{y}_1\dot{y}_1}(\omega_1)) \cdot 1 & \text{sign}(S_{\dot{y}_2\dot{y}_1}(\omega_1)) \cdot \sqrt{\frac{S_{\dot{y}_2\dot{y}_2}(\omega_1)}{S_{\dot{y}_1\dot{y}_1}(\omega_1)}} \end{array} \right]^T \quad (3.75)$$

$$\{\phi_2\} = \left[\begin{array}{cc} \text{sign}(S_{\dot{y}_1\dot{y}_2}(\omega_2)) \cdot 1 & \text{sign}(S_{\dot{y}_2\dot{y}_2}(\omega_2)) \cdot \sqrt{\frac{S_{\dot{y}_2\dot{y}_2}(\omega_2)}{S_{\dot{y}_1\dot{y}_1}(\omega_2)}} \end{array} \right]^T A \quad (3.76)$$

3.4 Welch's Method

Welch's method is employed to make PSD plots previously derived in section 3.3 [34] smooth. The data set used to obtain the PSD plot consists of a stochastic process which may complicate the peak-picking process. In order to smooth out the PSD plot, Welch's method may be employed to filter out as much noise as possible. This is done by subdividing the original time series into shorter, overlapping time series. The Power Spectral Density is estimated for each of these time series. The final PSD plot is an average of the PSD plots for all the subdivisions. The amount of divisions and overlap is an input to the method.

Each time series is tapered using a taper function to emphasize the middle part of the time series and reduce the influence of so called *edge effects*. In this thesis, *Hann window* is employed as the taper function. The taper function results in information loss at both ends of the time series. The overlap is therefore introduced to minimize the loss of information. More information about Hann window can be read in [35].

3.5 Modal Assurance Criterion

The *Modal Assurance Criterion (MAC)* estimates the correlation between two mode shapes [36]. Equation (3.77) calculates the MAC value of the two vectors $\{\phi_i\}$ and $\{\phi_j\}$:

$$MAC(\{\phi_i\}, \{\phi_j\}) = \frac{|\{\phi_i\}^H \{\phi_j\}|^2}{(\{\phi_i\}^H \{\phi_i\})(\{\phi_j\}^H \{\phi_j\})} \quad (3.77)$$

The MAC value varies between 0 and 1, where a value of 1 indicates perfect correlation, while the mode shapes are perfectly uncorrelated when the MAC value is 0.

3.6 Modal Phase Collinearity

The *Modal Phase Collinearity (MPC)* is applied to investigate the complexity of a mode shape and can be employed to distinguish the nearly real normal modes from the nearly complex, spurious modes [24]. The MPC value for mode shape 'i' is calculated according to equation (3.78).

$$MPC_i = \frac{\left\| \text{Re}(\{\tilde{\phi}_i\}) \right\|^2 + \left(\text{Re}(\{\tilde{\phi}_i\}^T) \text{Im}(\{\tilde{\phi}_i\}) \right) \left(2(\varepsilon_{MPC}^2 + 1) \sin^2 \theta_{MPC} - 1 \right) / \varepsilon_{MPC}}{\left\| \text{Re}(\{\tilde{\phi}_i\}) \right\|^2 + \left\| \text{Im}(\{\tilde{\phi}_i\}) \right\|^2} \quad (3.78)$$

where:

$$\{\tilde{\phi}_i\} = \{\phi_i\} - \text{mean}(\{\phi_i\}) \quad (3.79)$$

$$\varepsilon_{MPC} = \frac{\left\| \text{Im}(\{\tilde{\phi}_i\}) \right\|^2 - \left\| \text{Re}(\{\tilde{\phi}_i\}) \right\|^2}{2 \left(\text{Re}(\{\tilde{\phi}_i\}^T) \text{Im}(\{\tilde{\phi}_i\}) \right)} \quad (3.80)$$

$$\theta_{MPC} = \arctan \left(|\varepsilon_{MPC}| + \text{sgn}(\varepsilon_{MPC}) \sqrt{1 + \varepsilon_{MPC}^2} \right). \quad (3.81)$$

The MPC value varies between 0 and 1, and quantifies how real a mode shapes is. A MPC value equals 1 indicates that the mode is perfectly real and doesn't have an imaginary part. The mode is perfectly imaginary when the MPC value is equal to 0. A MPC value equal to 1 is unrealistic for real data due to noise. The characterization of mode as real is often determined by how close the MPC value is to 1.

3.7 Material Properties of Asphalt

Asphalt's dynamic properties are highly dependent on temperature and loading frequency [37]. Research has been conducted in order to approximate the dynamic stiffness, E^* , which may be calculated as follows:

$$\log(E^*) = \delta + \frac{\alpha}{1 + e^{\beta + \gamma \cdot \log(f_r)}} \quad (3.82)$$

where δ represents the minimum value of E^* and $\delta + \alpha$ represents the maximum value of E^* . The parameters β and γ are shape parameters controlling the slope and horizontal position of the turning point, respectively. Lastly, the parameter f_r represents a reduced frequency and is calculated as follows:

$$\log(f_r) = \log(f) + \log(\alpha_T) \quad (3.83)$$

where f is the loading frequency and α_T is a temperature dependent shift function, and may be calculated as shown in equation (3.84).

$$\alpha_T = \frac{-C_1 \cdot (T - T_r)}{C_2 + T - T_r} \quad (3.84)$$

T_r is a reference temperature, defined as 15°C in this thesis. The constants C_1 and C_2 are empirical constants [38]. The constants are later defined in section 4.3.2.

3.8 Human Induced Frequencies

SLT decks are mainly used for pedestrian bridges. In order to investigate the vibration serviceability, models have been developed to simulate the excitation loads by individual pedestrians and crowds. Two of the most common models are the French guideline Sétra and the European guideline HiVoSS [39]. In both models, the human induced walking force is modelled as sum of Fourier harmonic components [40]. According to Sétra, it is sufficient to avoid the resonance of the first harmonic. HiVoSS, on the other hand, additionally considers the second harmonic frequency in the vertical direction. Bridges should preferably avoid natural frequencies within the range induced by pedestrians. The frequencies of the first harmonic are presented below:

- Vertical and longitudinal direction: 1.25 to 2.3 Hz
- Lateral direction: 0.5 to 1.2 Hz.

The induced frequencies in the lateral direction are approximated to be half of the vertically induced frequencies. Lateral frequencies are caused by the nature of the walking process where the pedestrians' weight shifts between their right and left foot. Since the force from each step acts in the opposite lateral direction but the same vertical direction, the lateral frequency is half of the vertical frequency. Lateral frequencies will, however not be further considered in this thesis.

Taking into account the second harmonic, the pedestrian induced frequency range is expanded to 1.25-4.6 Hz. Pedestrian SLT bridges should preferably avoid vertical and torsional modes with natural frequencies within this interval to ensure that the vibration serviceability is fulfilled. To ensure that all relevant modes are considered in the analysis, all modes with a natural frequency lower than $3 \times f_{max,pedestrians} \approx 15 Hz$ are investigated, while higher natural frequencies are neglected [41].

Chapter 4

Method

4.1 Data Collection

All data sets analyzed in this master's thesis were previously gathered by Sigve and Lavina in 2021 [42]. This section simply seeks to explain the collection procedure performed to gather the analyzed data. It's worth noting that solely a small sample of the gathered data was investigated in this thesis. A more thorough description of the collection process is given in their thesis.

4.1.1 Equipment

The bridge decks were monitored with triaxial accelerometers. These sensors are able to identify accelerations in three orthogonal directions by utilizing the piezoelectric effect. Accelerations induce stresses in microscopic crystals resulting in voltage as output. The accelerometers separate accelerations in the three directions into three different cables. The voltage is translated into accelerations by a Compact Rio. The students who performed the analysis, decided to only record accelerations in the vertical direction (z-direction). This was done since they considered the decks to be too stiff in the lateral direction to have natural frequencies that could be excited by pedestrians. Hence why this thesis will solely analyze vertical accelerations and thus only vertical and torsional modes.

4.1.2 Sensor Placement

The bridge decks were monitored with 15 accelerometers strategically placed on the bridge decks. Due to the relative slenderness of SLT bridges, both vertical and torsional modes were expected to be excited by pedestrians. The configuration illustrated in figure 4.1 was utilized to ensure that vertical and torsional modes were identifiable.

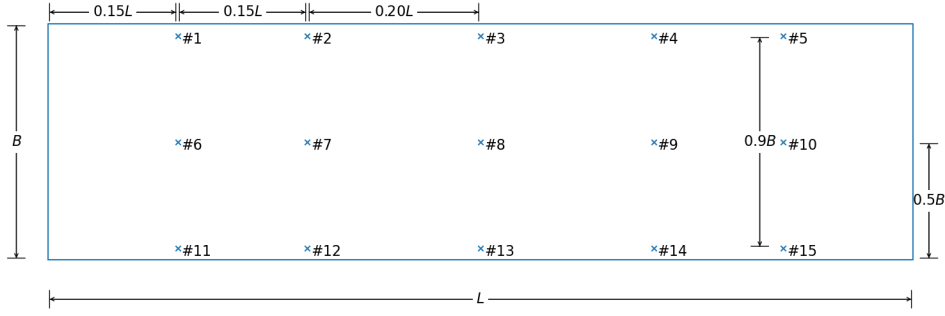


Figure 4.1: Sensor placement on the bridge deck.

4.1.3 Excitation Methods

Jumping Test

Jumping Tests were conducted by recording the accelerations while performing jumps on the bridge deck. Usually, a Jumping Test consists of jumps performed at several locations to excite all relevant modes of the bridge. However, the Jumping Tests data analyzed in this thesis, were solely excited by jumps performed at the midspan of the bridge decks.

Modal Hammer Test

A Modal Hammer Test (MHT) consists of exciting the bridge using a roving hammer. The roving hammer was moved around on the deck to excite all modes. In addition to recording the acceleration data, the roving hammer recorded the input force applied on the bridge deck. Due to the input force being recorded, this test is usually used for input-output modal identification techniques. This thesis will solely study output-only identification techniques. The input data was considered unknown and therefore neglected in future calculations.

Different hammer tips may be employed depending on the frequency range of interest [43]. In general, harder hammer tips excite a wider frequency range as opposed to softer hammer tips. A hard hammer tip was utilized during the MHT.

4.2 Analytical Analysis

The following sections will present the procedures utilized to investigate the acceleration data with the three modal analysis techniques.

4.2.1 Basic Frequency Domain Method

A Python script was created to analyse the time series from the Jumping Test and Modal Hammer Test in the frequency domain. The package *scipy.signal* was imported as it contains pre-built scripts for Welch's method and peak-picking. The data sets were separately investigated with these functions. To simplify the peak-picking process, smoothing was applied with Welch's method until the peaks in the PSD plots were easily identifiable. The peak-picking function

estimated the natural frequencies. Mode shapes were estimated by a self-written script employing the theory presented in section 3.3.

4.2.2 Stochastic Subspace Identification Methods

A Python package named *Strid* [44], written by Gunnstein T. Frøseth, was downloaded and imported to a Python script. This package contains several Stochastic Subspace Identification methods including the implementations of SSI-Cov and SSI-DD. The package requires the model order range, number of block rows, and data set as inputs and returns all estimated poles. Each pole was saved as a class containing relevant information as the model order, natural frequency, mode shape, damping ratio, and MPC value. The code subsequently filtered each pole by the filtering criteria previously defined in section 3.2 before plotting the stabilization diagram. A Python script was written to analyze the stabilization diagrams. To simplify the process, a minimum model order for when all modes had stabilized was identified. Frequency ranges for the different modes were identified to subdivide the poles into the separate modes. This part required some manual labor, but it drastically reduced the code complexity. Separating the poles into modes, allowed for the estimation of natural frequencies, mode shapes, and damping ratios.

Data sets from the Modal Hammer Test were analyzed. These time series were extremely long caused by a sampling frequency of 400 Hz and the excitation process taking a long time. The long time series resulted in the analysis being limited to a low number of block rows and model order which yielded poor results. To overcome this issue, a truncated time series was constructed. The analyzed time series only considered data where the roving hammer was located next to sensors 1 through 8. The roving hammer excited the bridge for one minute at each location. Time stamps indicated that moving the roving hammer took two minutes. These pauses were consequently removed to further reduce the length of the data set. The truncated time series analyzed consisted therefore solely of the time where the bridge deck was excited by the roving hammer. The number of block rows and model order could consequently be increased significantly.

4.3 Numeric Modelling

The dynamic properties of Stress-laminated Timber bridges have proven difficult to precisely estimate. This section will break down the modelling process in ABAQUS and highlight the assumptions. The finished model of the bridge deck is illustrated in figure 4.2. In order to make the modelling process as efficient as possible, a Python script was written to model the bridge deck, run the analysis, and export the mode shapes and natural frequencies. The script was based upon Martin Pltez's "*Efficient FE Modelling Course*" [45] and enabled quick editing of geometric parameters, material properties, and boundary conditions to further tune the model. It's worth noting that the bridge was greatly simplified resulting in the railing being neglected in the modelling process. The Python script can be found in appendix A. Each step of the

script will be further explained below.

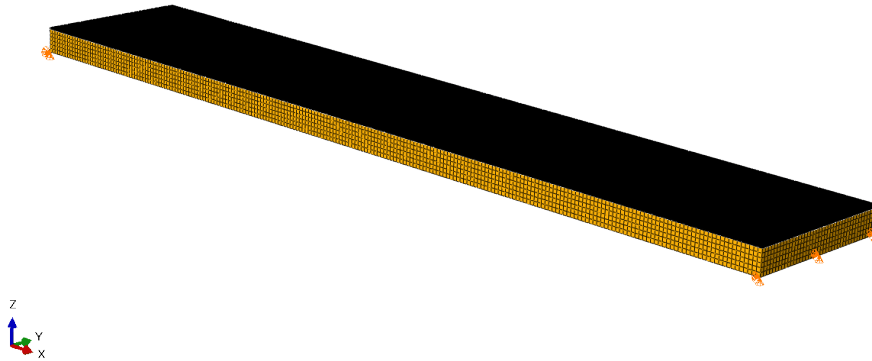


Figure 4.2: Stress-laminated Timber deck modelled in ABAQUS.

4.3.1 Creating the Parts

The bridge deck consists of two main parts; asphalt and Stress-laminated Timber deck. These parts are created and meshed separately in ABAQUS. The SLT deck is modelled using 3-dimensional deformable solids. This was chosen to ensure sufficient flexibility due to the great thickness of the SLT deck. The asphalt is modelled as a 3-dimensional deformable shell. Originally, the asphalt pavement was modelled using 3-dimensional deformable solids which led to an excessive amount of elements. This change marginally affected the results, yet the computational time was drastically reduced. Both parts are meshed with the same mesh size. The mesh size used is decided as the finest mesh our computers could handle and defined as six elements in the height of the SLT deck. The SLT deck is modelled using C3D8R elements, while the asphalt shell is modelled using S4R elements both with hourglass control.

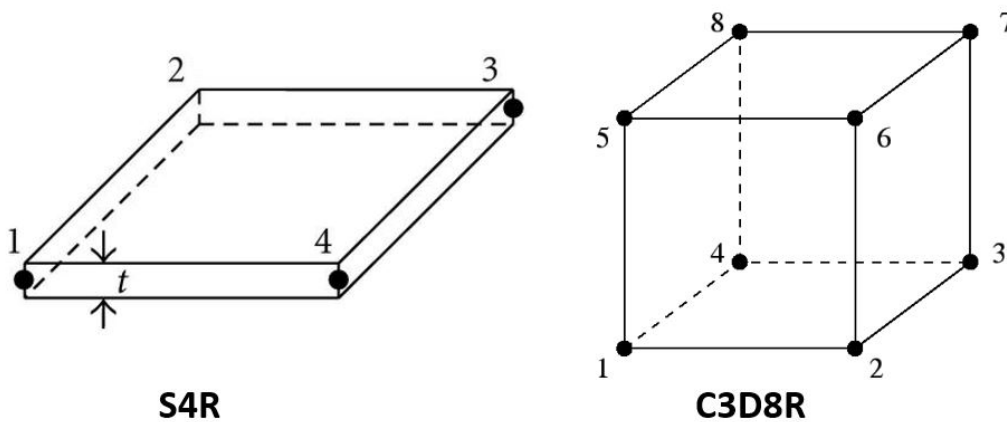


Figure 4.3: An illustration of S4R [46] and C3D8R [47] elements.

4.3.2 Defining the Materials

Asphalt's material properties are highly temperature dependent. The material is stiff for low temperatures, but soft for higher temperatures. The material is modelled as an *Isotropic* material with a Poisson's ratio of 0.3 assumed to be temperature independent. The elastic modulus is, however, highly dependent on the load frequency and temperature as presented in section 3.7. Loading frequency proved to be difficult to predict, and was assumed to be equal to the first natural frequency when the natural frequency was within the human induced frequency range. For bridges with the first natural frequency greater than the maximum human induced frequency, the loading frequency was assumed to be half of the first natural frequency. By implementing the parameters presented in table 4.1 into functions presented in section 3.7, the elastic modulus of the asphalt was derived.

Table 4.1: Parameters to estimate the elastic modulus of asphalt. The values are gathered from the on going research conducted by Hao Chen.

Parameter	Value
δ	0.9
α	3.8
β	-0.9
γ	0.4
C_1	16
C_2	110

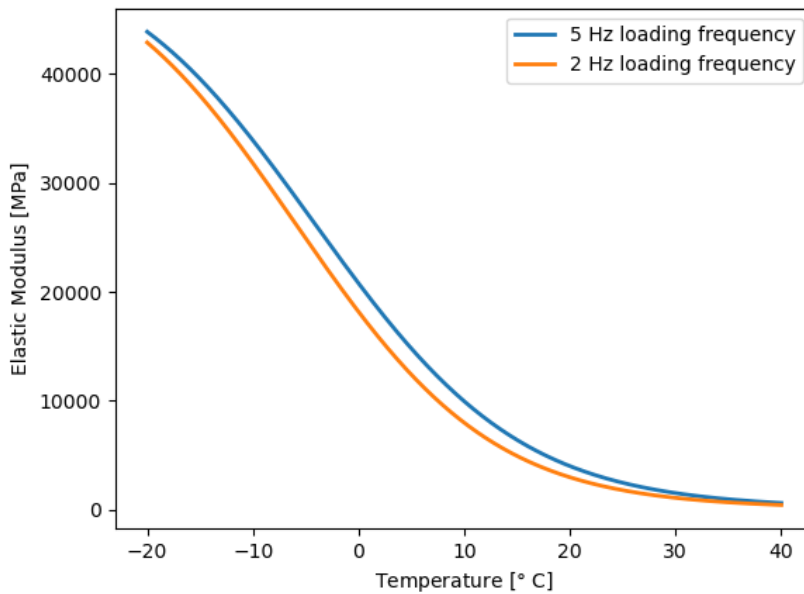


Figure 4.4: The elastic modulus of asphalt pavement as a function of temperature subjected to a loading of 5 Hz and 2 Hz, respectively.

The SLT bridge deck behaves as an orthotropic material, as mentioned in chapter 2. All SLT decks analyzed in this thesis consist of GL30C beams. The material is defined as *Engineering Constants* in ABAQUS and requires E_1 , E_2 , E_3 , G_{12} , G_{13} , G_{23} , ν_{12} , ν_{13} , ν_{23} , and ρ as inputs. These values are provided in NS-EN 14080 [8]. The N400 standard [48] describes that the 0.05-percentile stiffness and mean density should be used in the calculations. The parameters are presented in table 4.2. N400 also defines the load factor for the SLT deck and states that the density used in the analysis should be as shown in equation (4.1), where the last term is the density of the impregnating oils used on the timber.

$$\begin{aligned}\rho_{sup} &= 1.15 \cdot \rho_{mean} + 0.8 \text{ kg/m}^3 = 495.3 \text{ kg/m}^3 \\ \rho_{inf} &= 0.85 \cdot \rho_{mean} + 0.5 \text{ kg/m}^3 = 366 \text{ kg/m}^3\end{aligned}\tag{4.1}$$

Table 4.2: Elastic properties of GL30C.

\mathbf{E}_1 [MPa]	$\mathbf{E}_2, \mathbf{E}_3$ [MPa]	$\mathbf{G}_{12}, \mathbf{G}_{13}$ [MPa]	\mathbf{G}_{23} [MPa]	ν_{12} [-]	ν_{13}, ν_{23} [-]	ρ_{mean} [kg/m ³]
10800	250	540	54	0.5	0.6	430

4.3.3 Assigning Cross-sections

Firstly, a solid cross-section consisting of the previously defined material glulam is defined. The cross section is assigned to the SLT deck. Since glulam is an orthotropic material, it's necessary to define a coordinate system to ensure that the 1-direction is aligned with the length direction of the bridge. Lastly, a composite material consisting of one ply of asphalt is assigned to the asphalt part.

4.3.4 Assembly, Boundary Conditions, Constraints, and Step

An assembly is created to ensure that the asphalt is placed on top of the SLT deck. Boundary conditions are defined along two edges of the SLT deck, as seen in figure 4.2. One of the boundary conditions is pinned, while an input decides whether the other edge is a pinned or roller boundary condition. As mentioned in chapter 1, pinned-pinned boundary conditions yield superior results. All models analyzed in this thesis therefore have pinned-pinned boundary conditions. Due to the cold temperatures during the data collection, the asphalt layer is very stiff. A tie constraint is defined, connecting the touching faces of the two parts together. This assumption is, however, most likely only valid for lower temperatures. Lastly, a *Frequency* step is created in order to estimate natural frequencies and mode shapes of the model.

4.3.5 Rotational Stiffness

In order to implement rotational stiffness caused by the stiffness of the asphalt, springs are added to the asphalt shell as illustrated in figure 4.5. The rotational stiffness is modelled using equivalent horizontal springs, due to the 3D solid elements in the SLT deck not having rotational degrees of freedom. The springs are placed to correspond with the nodes of the mesh. It's worth noting that the script takes the horizontal stiffness as an input with a unit of $N/mm/mm$, not the rotational stiffness.

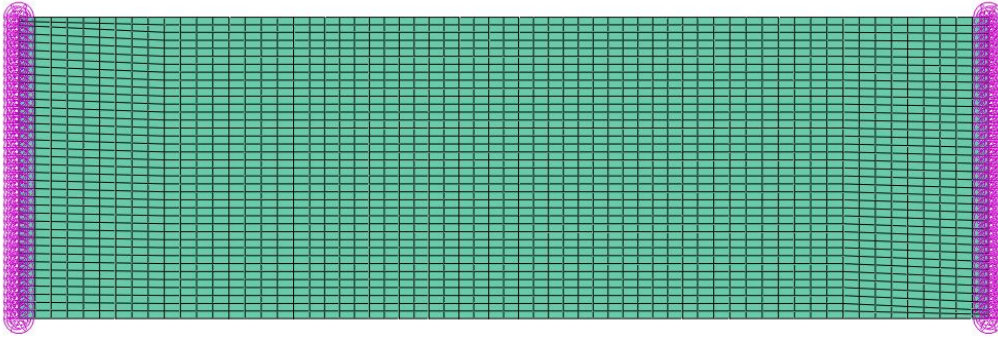


Figure 4.5: An example of spring placement on the asphalt part.

4.3.6 Creating Field-outputs

The Stress-laminated Timber bridges were monitored with 15 accelerometers as illustrated in figure 4.1. In order to compare the mode shapes from ABAQUS with the mode shapes derived using the data from the accelerometers, displacements in the z-direction from the coordinates of the accelerometers need to be extracted. The asphalt part is partitioned to make nodes at the sensor locations. Each node is assigned an unique name corresponding to the numbering illustrated in figure 4.1. A field-output is created for each node set extracting the displacement of the sensors.

4.3.7 Post-processing

Displacements are extracted as XY-data. Since ABAQUS doesn't allow for manual naming of XY-data results, a for loop with a try/except function changes the name of the output to correspond with the numbering introduced in figure 4.1. It's worth noting that this loop is based on the assumption that the automatic numbering generated by ABAQUS doesn't exceed 50. The displacements in the U_3 -directions are extracted and saved in a text-file. The OTB-file is opened and the natural frequencies are extracted and saved in another text-file. Lastly, another script reads the two text-files, sorts, and saves the data with the desired name as a npz-file. The npz-file contains the mode shapes and natural frequencies on the same format as the results from BFD, SSI-Cov, and SSI-DD ensuring that the different results easily may be compared.

Chapter 5

Bridges

5.1 Raufoss

The studied bridge in Raufoss was completed in 2019 and spans Hunnselva river. Sketches of the bridge indicate a slope of 1.82° . The slope is, however, neglected during the modelling process. The data was collected on the 9th of March, 2021. Unfortunately, the temperature wasn't recorded during the data collection. However, based on historic temperatures for the area, it was assumed that the asphalt had a temperature of approximately $3^\circ C$. The bridge deck was also covered by a thin layer snow on the day of the measurement.



Figure 5.1: Photograph of the bridge analyzed in Raufoss. The picture was taken by Petter Juell Nåvik.

Geometric properties

Length: 22,000 *mm*

Width: 4,046 *mm*

Slat width: 119 *mm*

Slat height: 600 *mm*

Slat quality: GL30C

Asphalt pavement thickness: 35 *mm*

5.2 Brumuddal

The Brumuddal bridge was completed in 2020 and spans Skanselva river. Structural drawings of the bridge don't indicate any slope. Measurements were conducted on the 9th of March, 2021. The deck was not covered in snow, and the average temperature was measured to be 0.7°C.



Figure 5.2: Photograph of the bridge analyzed in Brumuddal. The picture was taken by Petter Juell N avik.

Geometric properties

Length: 12,500 *mm*

Width: 3,885 *mm*

Slat width: 119 *mm*

Slat height: 367 *mm*

Slat quality: GL30C

Asphalt pavement thickness: 35 *mm*

Chapter 6

Results and Discussion

6.1 Raufoss Bridge

6.1.1 Basic Frequency Domain Method

This section will study the Basic Frequency Domain method performed on data sets from two different excitation methods; Jumping Test and Modal Hammer Test.

Jumping Test data

Due to noise, the PSD plots were coarse resulting in peak-picking becoming significantly more challenging. To make the PSD plot smooth, Welch's method with four divisions was employed. The plot clearly identified three modes as figure 6.1 illustrates. The estimated natural frequencies are presented in table 6.1, while the corresponding mode shapes are illustrated in figure 6.2.

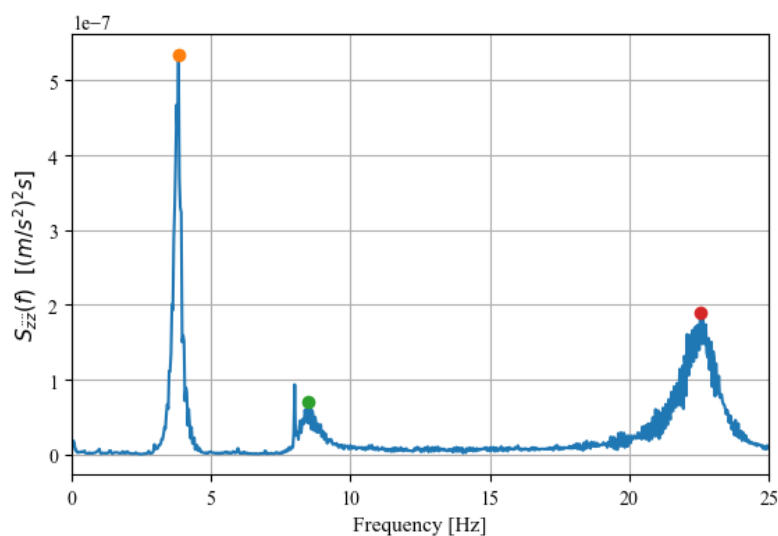


Figure 6.1: Power Spectral Density plot for sensor 1 obtained using the BFD method on the Jumping Test data.

Table 6.1: The natural frequencies of Raufoss bridge estimated from the PSD plot of the Jumping Test data.

Mode "i"	f_i [Hz]	Type
1	3.8333	Vertical
2	8.4667	Torsion
3	22.5333	Vertical

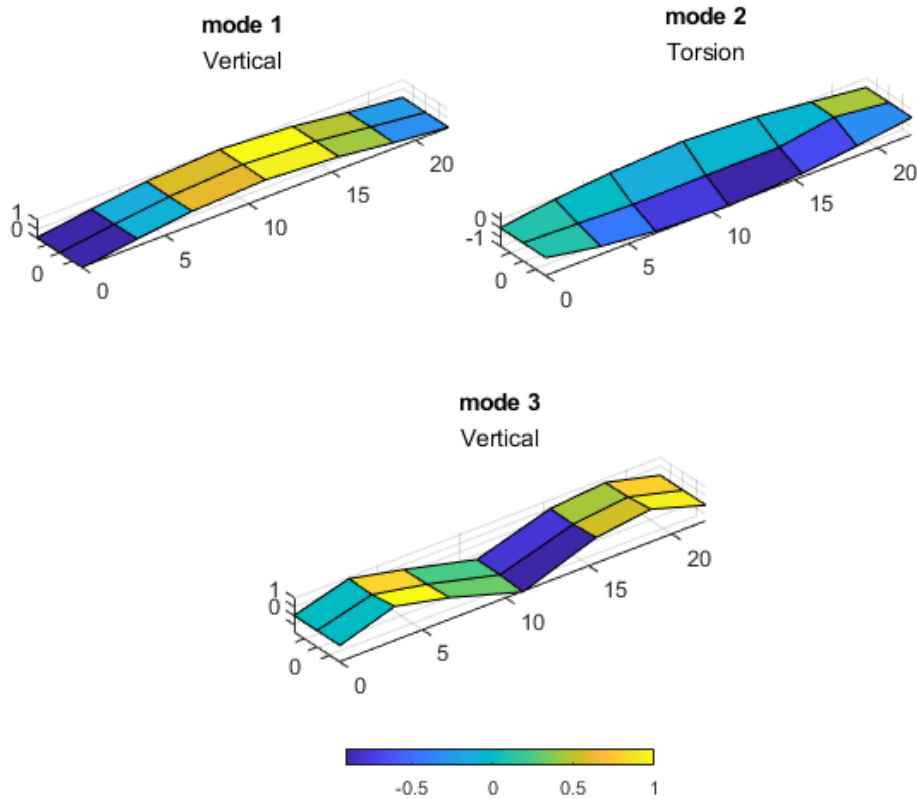


Figure 6.2: The displacement-normalized mode shapes of Raufoss bridge estimated by the BFD method using Jumping Test data.

Modal Hammer Test data

The PSD plot from the MHT was very coarse. To overcome this issue, the PSD plot was made smooth by Welch's method with 15 divisions. The smoothed out PSD plot is presented in figure 6.3. The PSD plot clearly identifies five different modes. The natural frequencies were identified by picking frequencies corresponding to the peaks of the PSD plot. The picked modes are represented by coloured dots. Estimated natural frequencies are presented in table 6.2, while the displacement-normalized mode shapes are illustrated in figure 6.4.

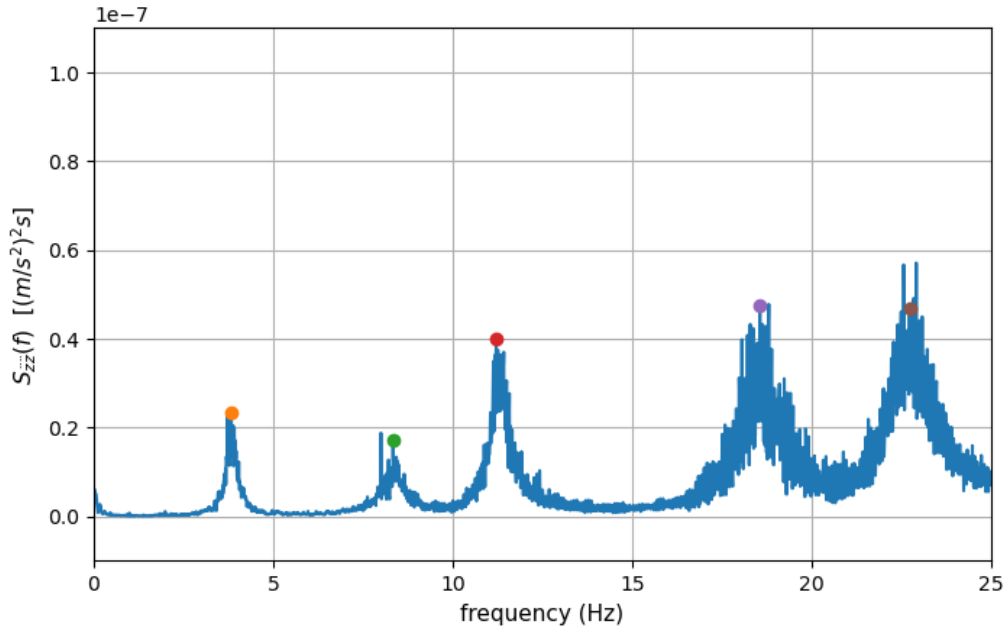


Figure 6.3: Power Spectral Density plot for sensor 11 obtained using the BFD method on the Modal Hammer Test data.

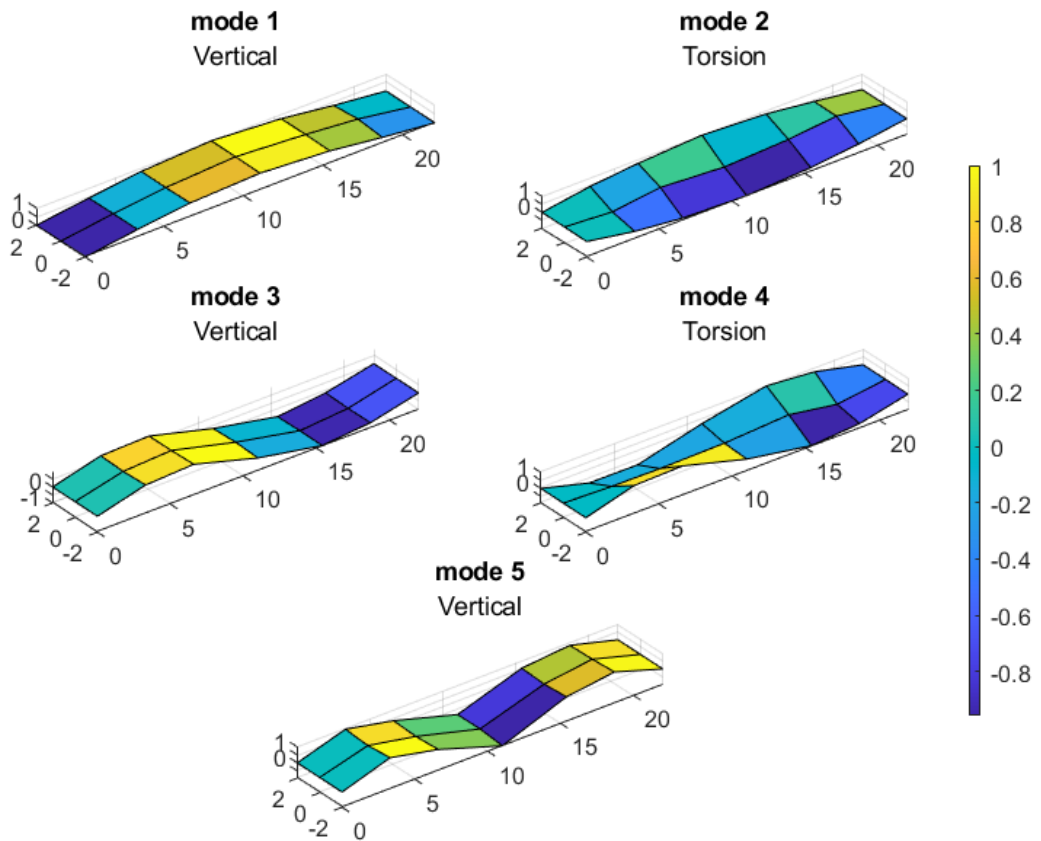


Figure 6.4: The displacement-normalized mode shapes of Raufoss bridge estimated by the BFD method using MHT data.

Table 6.2: The natural frequencies of Raufoss bridge derived using the PSD plot of the Modal Hammer Test data.

Mode "i"	f_i [Hz]	Type
1	3.8281	Vertical
2	8.3359	Torsion
3	11.2109	Vertical
4	18.5547	Torsion
5	22.7266	Vertical

Comparing the results from the excitation methods

Studying the mode shapes from the Jumping Test, it becomes evident that the data failed to estimate all modes. Vertical modes tend to be sinusoidal, as perfectly illustrated by the mode shapes for the vertical modes illustrated in figure 6.2 and 6.4. However, the sinus wave consisting of a full wavelength is clearly missing from the Jumping Test results. As mentioned in section 4.1, the Jumping Test was conducted by solely performing jumps at the midspan of the bridge. Modes not expected to exhibit deformation at the midspan, were consequently not excited by the jumps. The Jumping Test data set managed to identify several modes of the bridge, yet it was clearly unable to represent all modes. Performing jumps at different locations could ensure the excitation of all relevant modes. This becomes apparent as the MHT identified two modes not present in the results from the Jumping Test. The roving hammer was moved around the bridge deck and consequently excited more modes.

Modes identified by both time series yielded similar results. There were small deviations between the estimated natural frequencies. These inaccuracies were minimal and likely caused by inaccuracies in the peak-picking process. Noise introduced uncertainties in the exact location of the peaks. Welch's method simplified the peak-picking process but did not necessarily improve the accuracy of the peak locations. Welch's method may even have induced additional inaccuracies due to edge effects. There are still therefore uncertainties of the exact peak locations in the PSD plots presented in figure 6.1 and 6.3. Mode shapes identified by both excitation methods are practically identical.

Lastly, a significant peak can be identified in the PSD plots for a frequency of approximately 8 Hz. The slenderness of the peak indicates that the possible corresponding mode has low damping. This frequency was identified by the SSI methods, and therefore further investigated in section 6.1.2.

6.1.2 Stochastic Subspace Identification

This section will present and discuss the dynamic properties derived from employing the two Stochastic Subspace Identification methods on the data from Raufoss bridge. Only the Modal Hammer Test data was analyzed in this section since results presented in section 6.1.1 indicated that the Jumping Test failed to excite all modes.

Stabilization diagrams

Stabilization diagrams were estimated from the MHT data set by employing both SSI-Cov and SSI-DD. Both SSI methods were analyzed using identical input parameters. The model order was varied between 0 and 400 with a step size of 1, while the number of block rows was set to 150. The stabilization diagrams were plotted for a frequency range of 0 to 25 Hz. The Power Spectral Density plotted in the background enables easy comparison between the stabilized modes and the frequency content of the input data. The recorded MHT data set was obscenely large and employing the SSI methods on the entire time series would require significant computational power. A truncated data set was therefore constructed as explained in section 4.2. Cutting out periods of time without excitation should logically not influence the results significantly, but cutting the time series too close after excitation could result in loss of information thus possibly introducing inaccuracies.

The stabilization diagram estimated by the SSI-Cov method is presented in figure 6.5. Six modes were identified for the frequency range of interest. For further analysis of the identified modes in the stabilization diagram, a model order range where all modes had stabilized was identified. The second and third mode are closely spaced and therefore require higher model order to differentiate. Model orders between 200 and 400 were utilized to analyze the dynamic properties of the bridge. Data for model orders lower than 200 were therefore disregarded in further calculations.

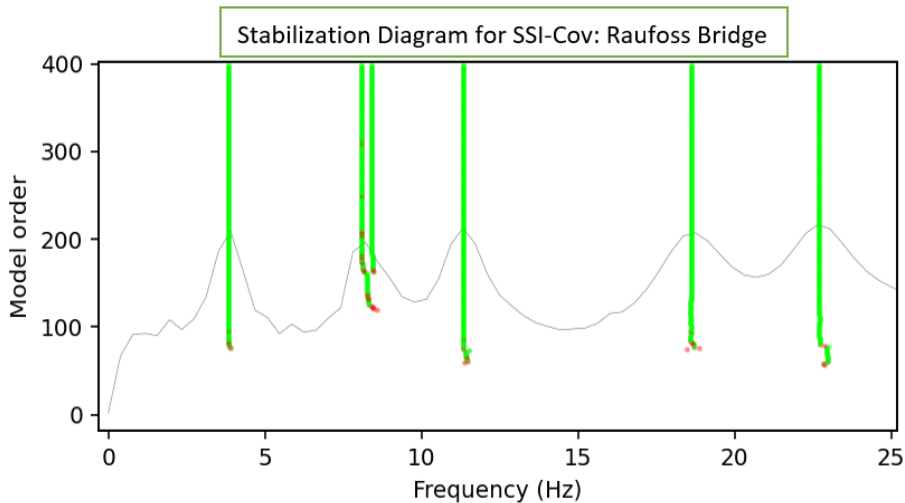


Figure 6.5: Stabilization diagram of Raufoss bridge using SSI-Cov with number of block rows equal to 150.

The stabilization diagram estimated by the SSI-DD method is presented in figure 6.6. Similarly to SSI-Cov, the second and third mode are closely spaced and require high model order to distinguish. Compared to the SSI-Cov method, the modes stabilize faster for the SSI-DD method. For comparison reasons between the two SSI methods, data for model orders lower than 200 were neglected in further calculations.

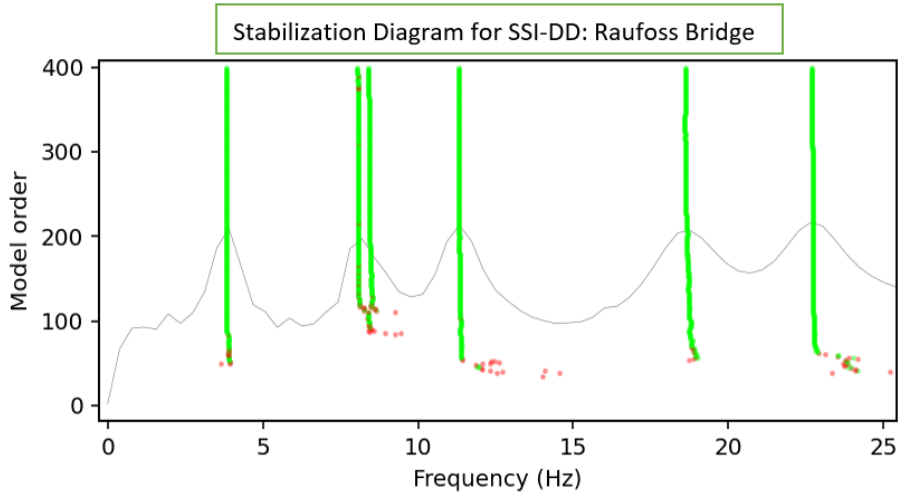


Figure 6.6: Stabilization diagram of Raufoss bridge using SSI-DD with number of block rows equal to 150.

Possible physical mode

The stabilization diagrams shown in figure 6.5 and 6.6 illustrate two closely spaced modes. The mode shapes were plotted, and the mode with the highest natural frequency of the two closely spaced modes was identified as the first torsional mode. This section seeks to investigate the mode with the lowest natural frequency of the two modes and determine whether it's a physical mode belonging to the bridge deck. The estimated mode shapes of the investigated mode were identically normalized and are presented in figure 6.7. Both SSI methods estimate the natural frequency to 8.07 Hz. The Power Spectral Density plots presented in section 6.1.1 indicate a narrow spike for the same frequency. To further investigate the mode, the estimated modal damping ratios were plotted as functions of the model order as presented in figure 6.8.

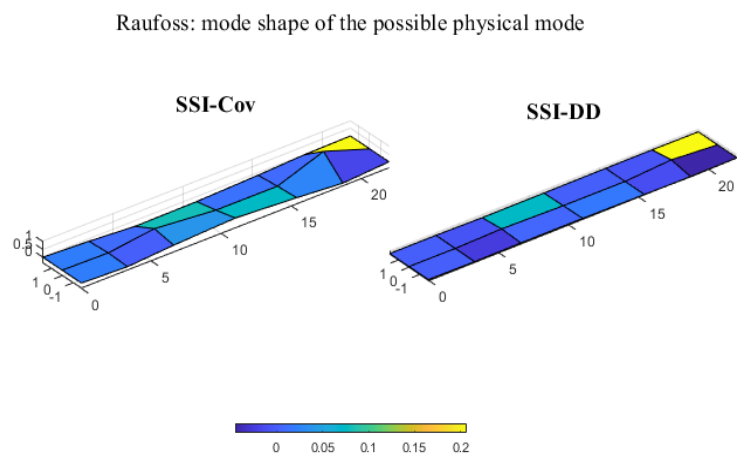


Figure 6.7: The mode shape of the possible physical mode of Raufoss bridge estimated by SSI-Cov and SSI-DD.

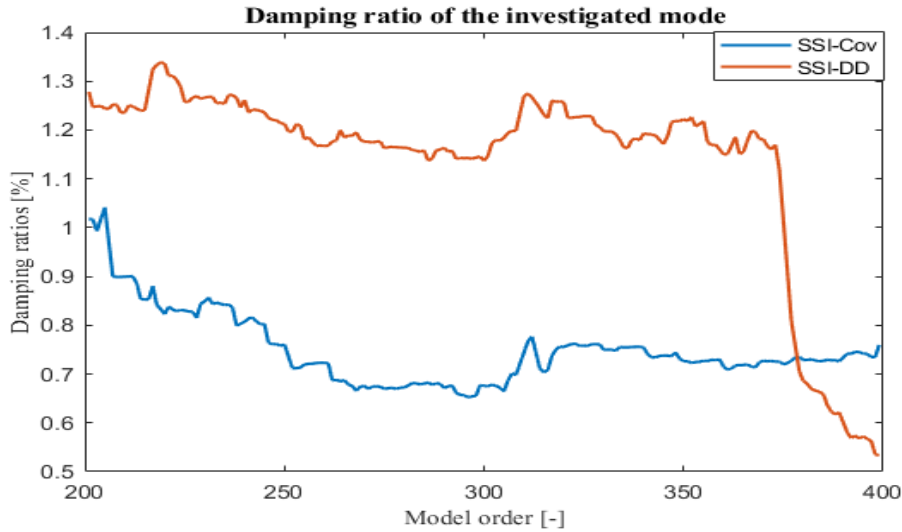


Figure 6.8: The damping ratio of the possible physical mode of Raufoss bridge estimated by the SSI methods.

Figure 6.8 indicates that the mode has a low damping ratio. This corresponds well with the hypothesis presented in section 6.1.1 stating that the mode probably had a low damping ratio due to the extreme narrowness of the peak. However, the modal damping ratio doesn't seem to converge when employing the SSI-DD. The damping ratio of this mode was significantly lower than the modal damping ratios estimated for the other well-defined modes. Additionally, the mode shape doesn't resemble anything one would expect of a mode shape belonging to the bridge deck. Since this thesis solely analyzed vertical accelerations, only torsional and vertical modes may be identified. Mode shapes of the other modes are later presented in figure 6.9. There are no missing vertical or torsional mode shapes. This mode was therefore assumed to be spurious and neglected in future calculations. The mode will, however, be further discussed in section 6.3.

Mode shapes

Mode shapes of the five remaining modes are illustrated in figure 6.9. Each pole in the five modes had slightly different estimates for the respective mode shapes. Picking the correct mode shape from the stabilization diagrams is consequently a highly discussed topic. The displacement-normalized mode shapes presented in figure 6.9 were picked by identifying the pole with the highest MPC value for each mode. The corresponding natural frequencies and modal damping of the identified poles are presented in table 6.3.

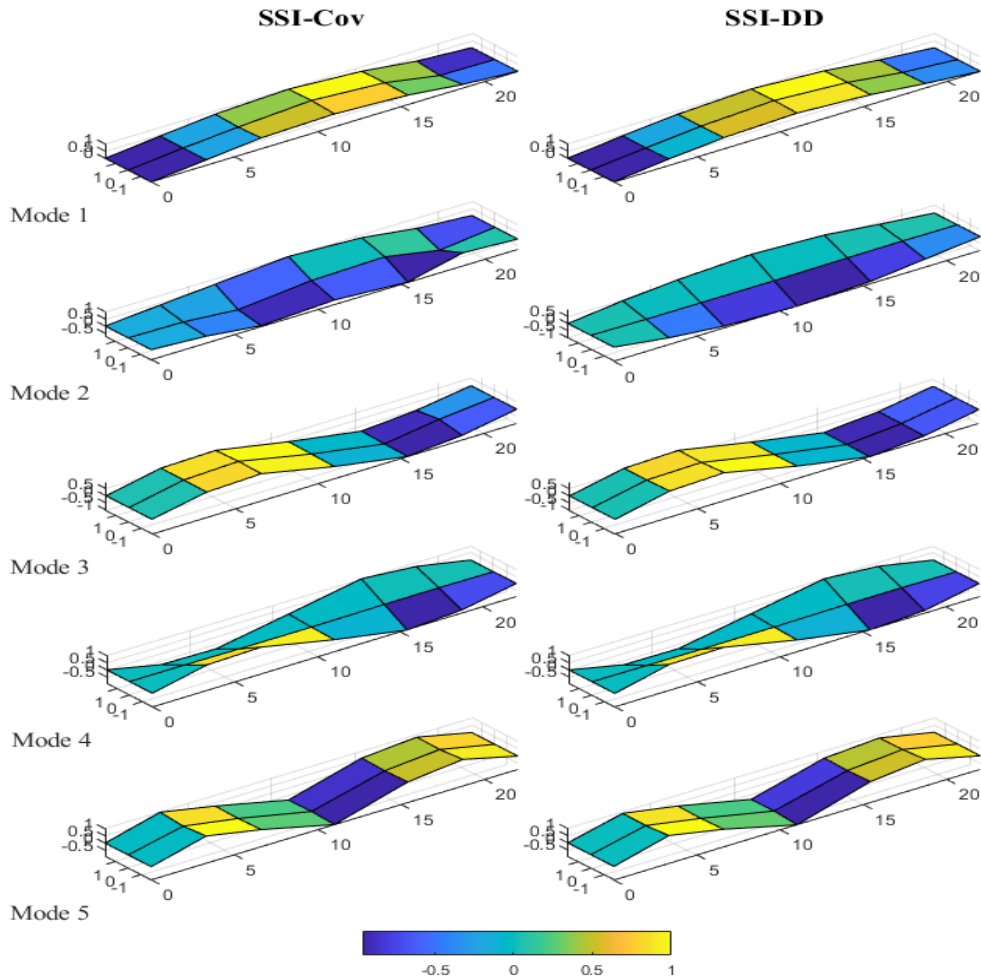


Figure 6.9: The mode shapes of Raufoss bridge corresponding to the highest MPC value, estimated by SSI-Cov and SSI-DD.

Table 6.3: Dynamic properties of the poles with the highest MPC values for SSI-Cov and SSI-DD.

Mode "i"	SSI-Cov			SSI-DD		
	MPC_{\max} [%]	$f_{i,MPC_{\max}}$ [Hz]	$\xi_{i,MPC_{\max}}$ [%]	MPC_{\max} [%]	$f_{i,MPC_{\max}}$ [Hz]	$\xi_{i,MPC_{\max}}$ [%]
1	99.88	3.8267	4.39	99.77	3.8258	4.53
2	99.70	8.4104	6.20	99.70	8.4085	5.67
3	99.70	11.3181	3.22	99.82	11.3154	3.21
4	99.98	18.6068	4.34	99.79	18.6142	4.45
5	99.95	22.6976	3.36	99.75	22.6978	3.41

Studying the mode shapes presented in figure 6.9, it became evident that both SSI methods yielded similar mode shapes. Both methods identified modes one, three, and five as vertical and modes two and four as torsional mode shapes. SSI-Cov, however, inaccurately predicted

the mode shape for the second mode. To ensure that the picked pole was representative, the MAC between the picked second mode shape from SSI-DD and the mode shapes estimated by SSI-Cov for different model orders were calculated. The picked pole yielded the highest MAC value. The inaccuracy may have been caused by the mode being closely spaced with another mode. Comparing the mode shape of the previously disregarded mode with the inaccurate mode shape, it becomes apparent that the spurious mode shape absorbs energy intended for the second mode shape estimated by SSI-Cov. Locations with strange results in the first torsional mode shape were emphasized in the spurious mode shape indicating that the mode absorbed energy. By lowering the number of block rows to 50, the two modes failed to properly separate. The estimated mode shape, presented in figure 6.10, was greatly improved. This indicates that SSI-Cov struggled to accurately estimate the mode shapes after the two modes had separated and stabilized.

Mode shape of mode 2 of Raufoss bridge estimated by SSI-Cov

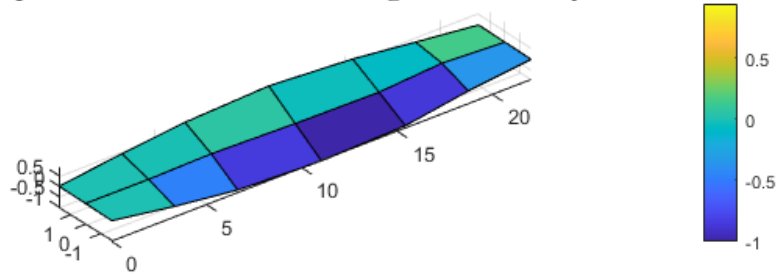


Figure 6.10: Mode shape of the second mode of Raufoss bridge estimated by SSI-Cov with 50 as the number of block rows.

Natural frequencies

The natural frequency for each mode was estimated by calculating the mean value, mode value, and standard deviation from the presumed stable poles. Figure 6.11 presents histograms of the natural frequencies for the five modes estimated by SSI-Cov and SSI-DD, where the mean values are represented by red lines. The estimated values for the natural frequencies are presented in table 6.4.

Table 6.4: Mean values, mode values, and standard deviations of the estimated natural frequencies of Raufoss bridge derived using SSI-Cov and SSI-DD.

Mode "i"	SSI-Cov			SSI-DD		
	$f_{i,\text{mean}}$ [Hz]	$f_{i,\text{mode}}$ [Hz]	Δf_i [Hz]	$f_{i,\text{mean}}$ [Hz]	$f_{i,\text{mode}}$ [Hz]	Δf_i [Hz]
1	3.8291	3.8300	0.0015	3.8262	3.8255	0.0008
2	8.4070	8.4021	0.0046	8.4295	8.4277	0.0112
3	11.3166	11.3160	0.0008	11.3150	11.3092	0.0066
4	18.6044	18.6059	0.0021	18.6178	18.6065	0.0171
5	22.6956	22.6958	0.0015	22.7048	22.7004	0.0068

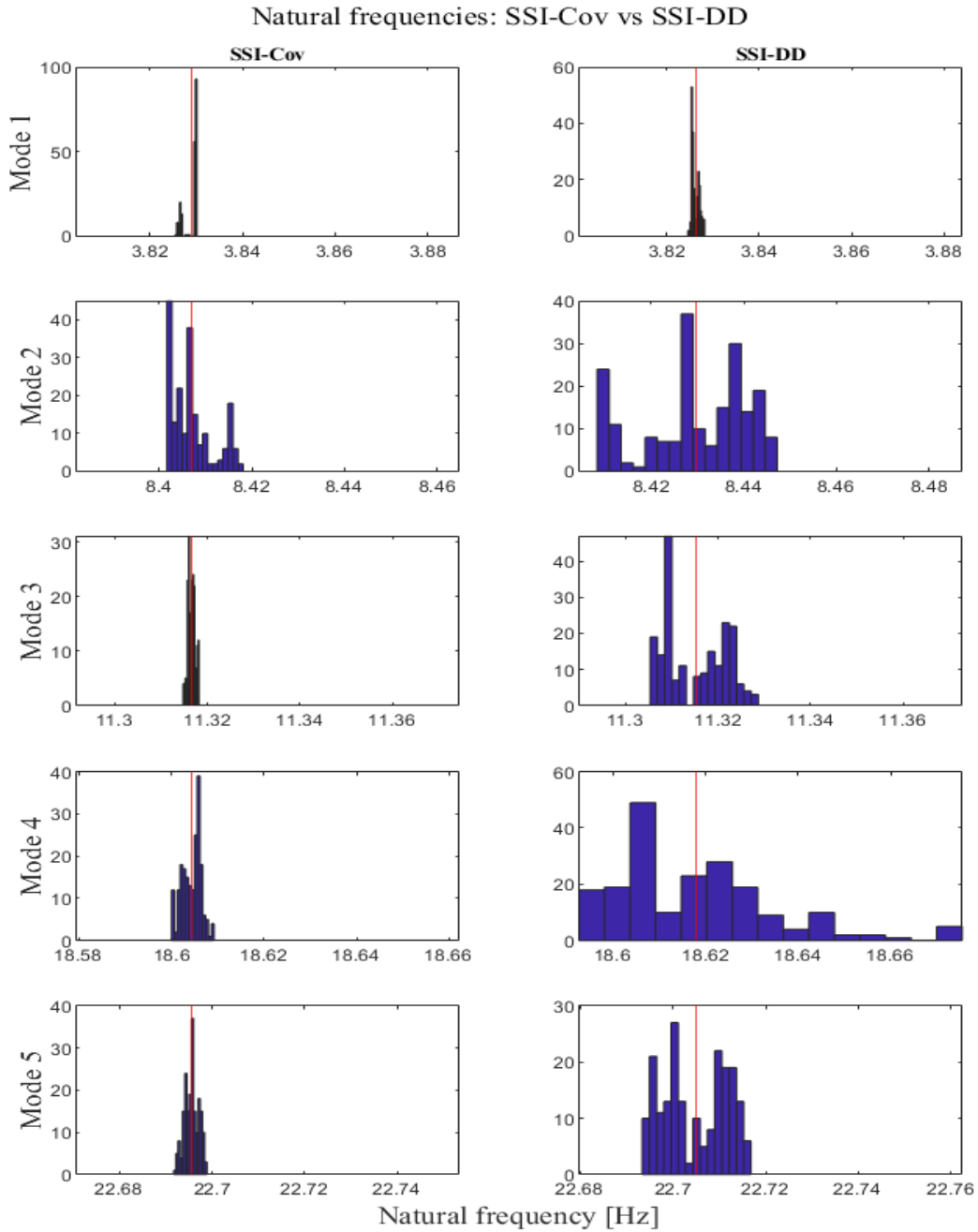


Figure 6.11: Histograms of the natural frequencies of Raufoss bridge estimated by the SSI methods.

The estimated natural frequencies were, for all practical cases, identical. There were minimal deviations between the natural frequencies derived using mean and mode value. This emphasized the little spread between natural frequencies estimated for different model orders as can be seen in figure 6.11. The standard deviation was consistently lower for the SSI-Cov method compared to the SSI-DD method, except for the first mode.

Modal damping ratios

Similarly to the natural frequencies, the modal damping ratios were estimated through the use of mean values, mode values, and standard deviations. The results are presented in table 6.5. Histograms of the damping ratios for the different modes are presented in figure 6.12, where the red line represents the mean values of the modal damping ratios. Lastly, the stabilization of the modal damping ratios for different model orders were investigated. The convergence of the damping ratios is illustrated in figure 6.13.

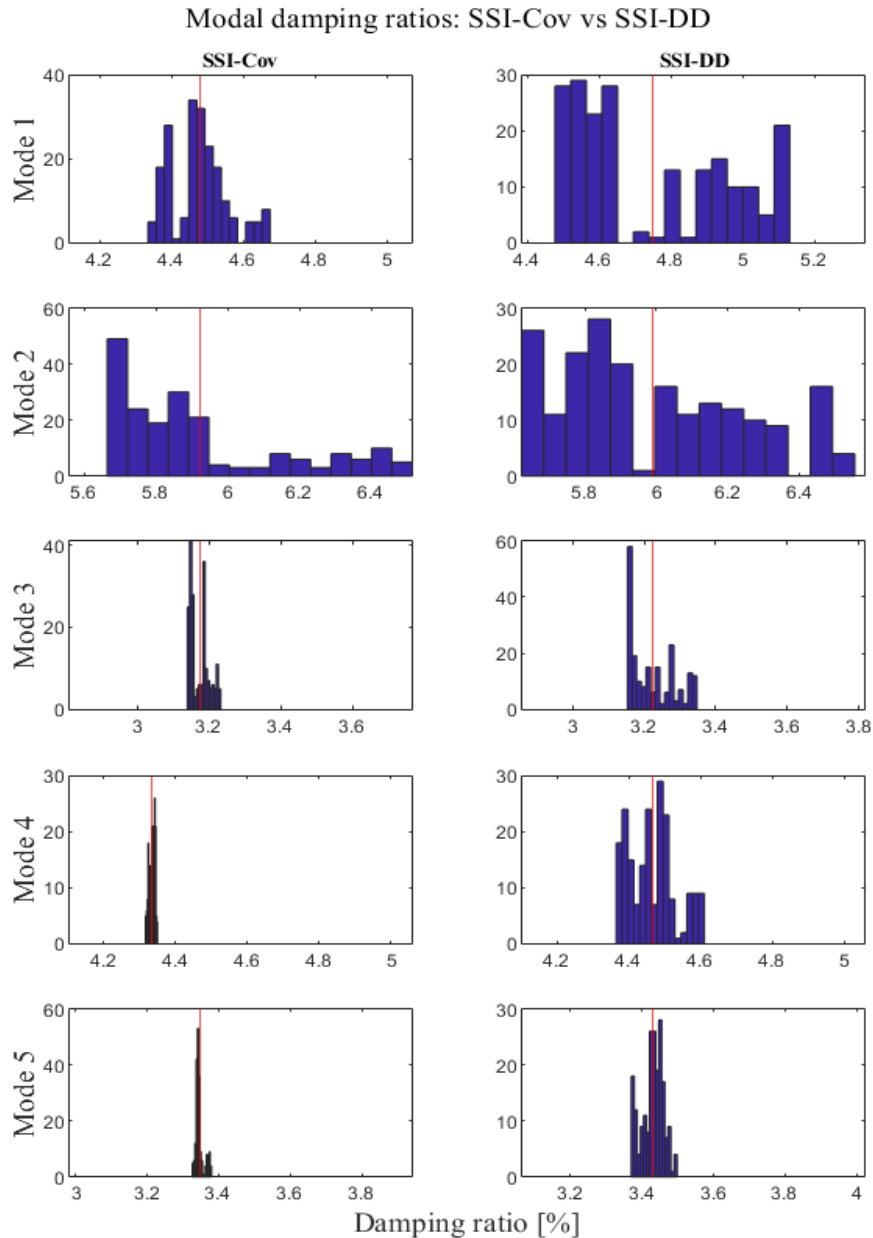


Figure 6.12: Histograms of the estimated modal damping ratios of Raufoss bridge by the SSI methods.

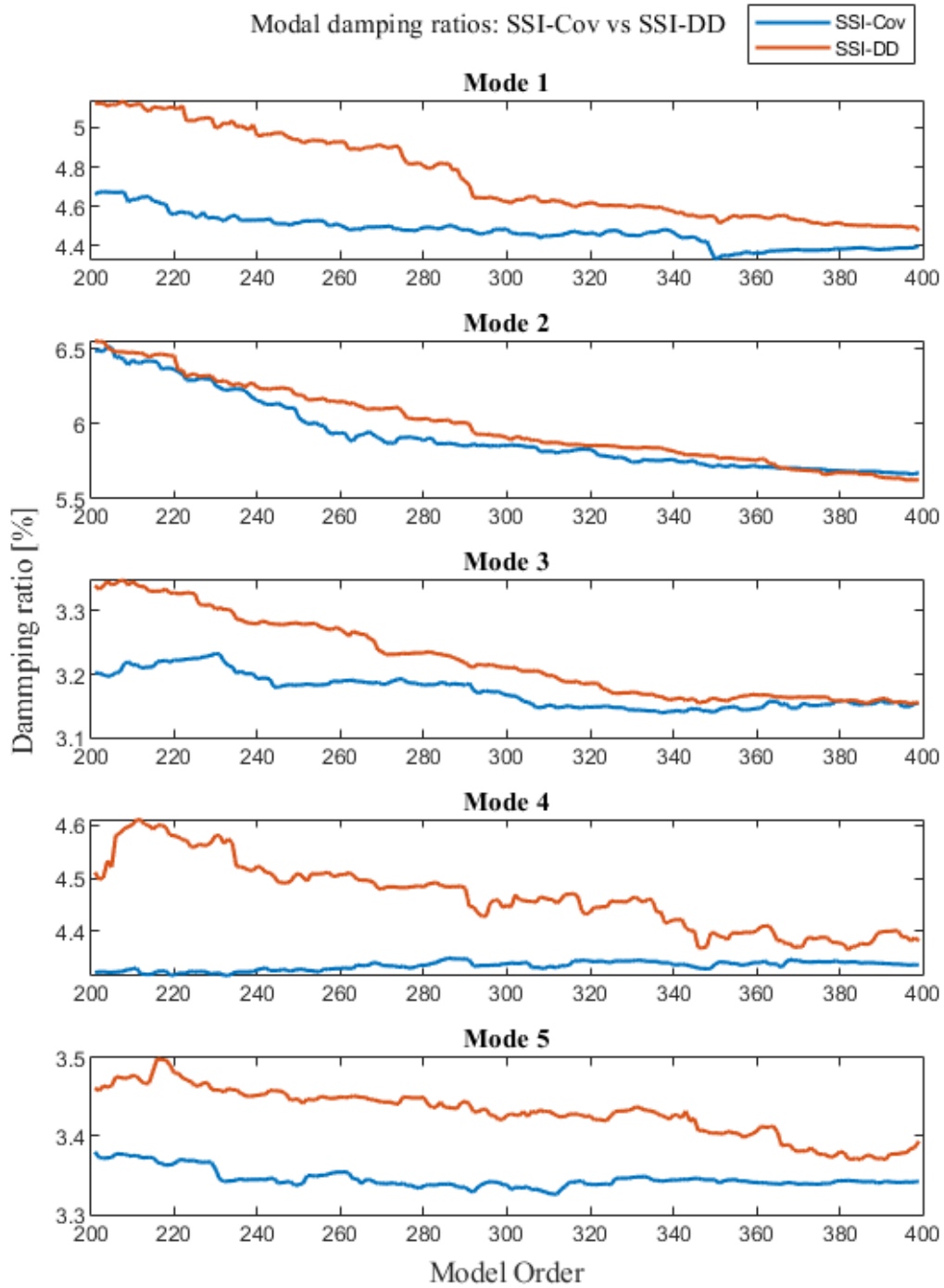


Figure 6.13: The modal damping ratios of Raufoss bridge plotted as functions of the model order estimated by the SSI methods.

Table 6.5: Mean values, mode values, and standard deviations of the modal damping ratios of Raufoss bridge derived using the SSI methods.

Mode "i"	SSI-Cov			SSI-DD		
	$\xi_{i,\text{mean}}$ [%]	$\xi_{i,\text{mode}}$ [%]	$\Delta\xi_i$ [%]	$\xi_{i,\text{mean}}$ [%]	$\xi_{i,\text{mode}}$ [%]	$\Delta\xi_i$ [%]
1	4.48	4.46	0.08	4.75	4.54	0.21
2	5.92	5.69	0.24	5.99	5.84	0.26
3	3.17	3.15	0.03	3.22	3.16	0.06
4	4.33	4.34	0.01	4.47	4.49	0.07
5	3.35	3.34	0.01	3.43	3.45	0.03

By studying the convergence of the modal damping ratios illustrated in figure 6.13, it became apparent that the SSI-Cov method converged for lower model orders compared to the SSI-DD method. The SSI-DD method consistently overestimated the modal damping ratios for lower model orders. This yielded greater spread in the results and thus higher estimated modal damping ratios and standard deviations compared to the results derived from the SSI-Cov method. This reasoning was, however, not applicable for the second mode. The modal damping ratio for the second mode was initially overestimated by both SSI-Cov and SSI-DD, while both slowly converge towards an approximate damping ratio of 5.6%. Although SSI-DD required higher model orders to converge, the damping ratios eventually converged towards the damping ratios estimated by SSI-Cov.

6.1.3 Finite Element Model Comparison

This section will compare the dynamic properties extracted from the ABAQUS model with the analytical results. As mentioned in section 3.8, the frequency range of interest was limited to three times the maximum human induced frequency, $3 \times f_{\text{induced,max}} \approx 15$ Hz. The optimization consequently only considered the first three identified modes derived in the previous sections. The natural frequencies and mode shapes were extracted from the ABAQUS model for different rotational stiffnesses. The following sections will compare the results from the three modal analysis techniques to the result from ABAQUS. The rotational stiffness was optimized to minimize the error of the first natural frequency. All data extracted from ABAQUS was derived with the assumption that the asphalt pavement's temperature was 3°C and the bridge deck was subjected to a loading frequency of 4 Hz. The loading frequency was chosen as it was approximately equal to the first natural frequency previously estimated.

ABAQUS vs BFD

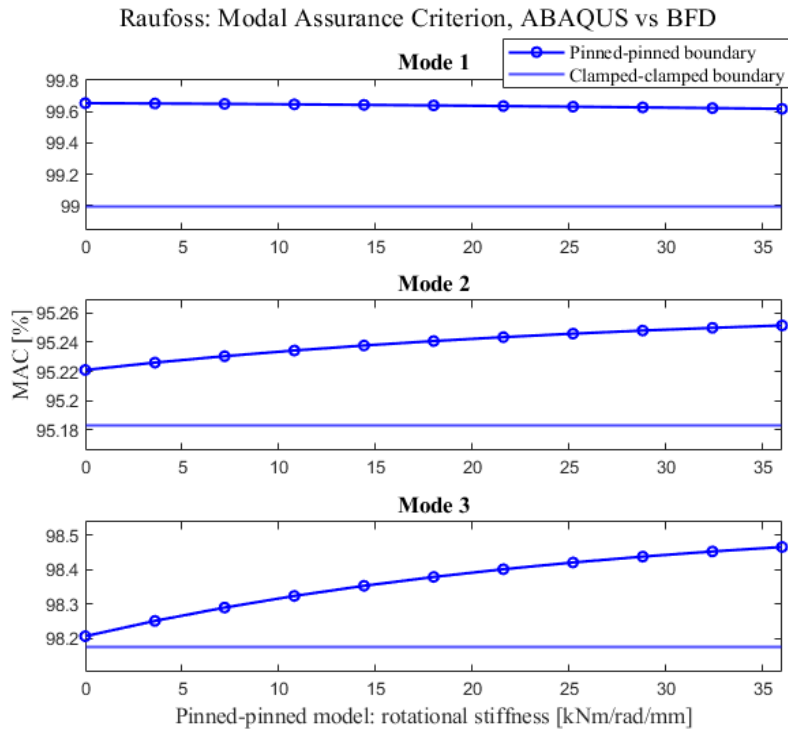


Figure 6.14: The MAC values between the mode shapes estimated by ABAQUS and BFD for Raufoss bridge.

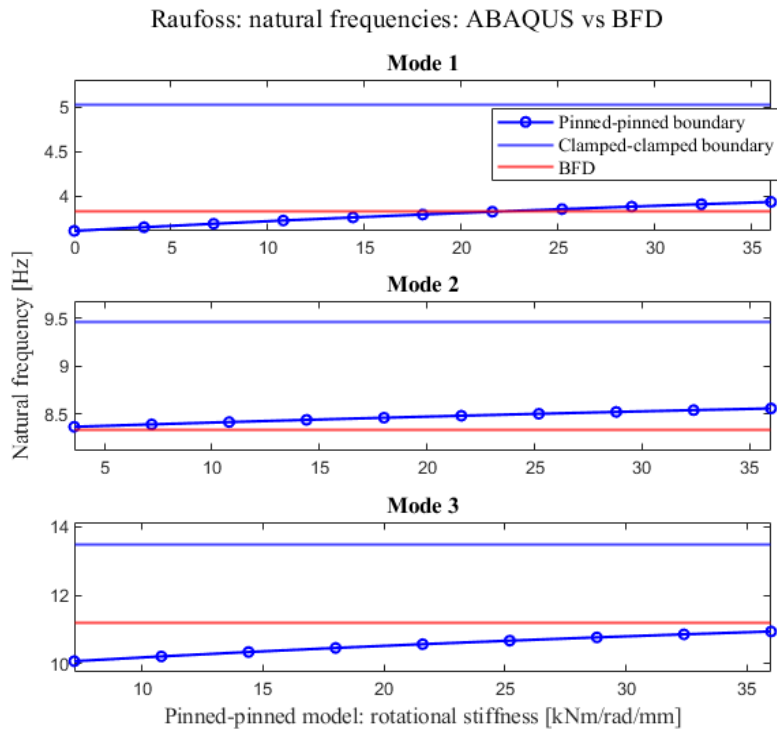


Figure 6.15: The natural frequencies estimated by ABAQUS and BFD for Raufoss bridge.

ABAQUS vs SSI-Cov

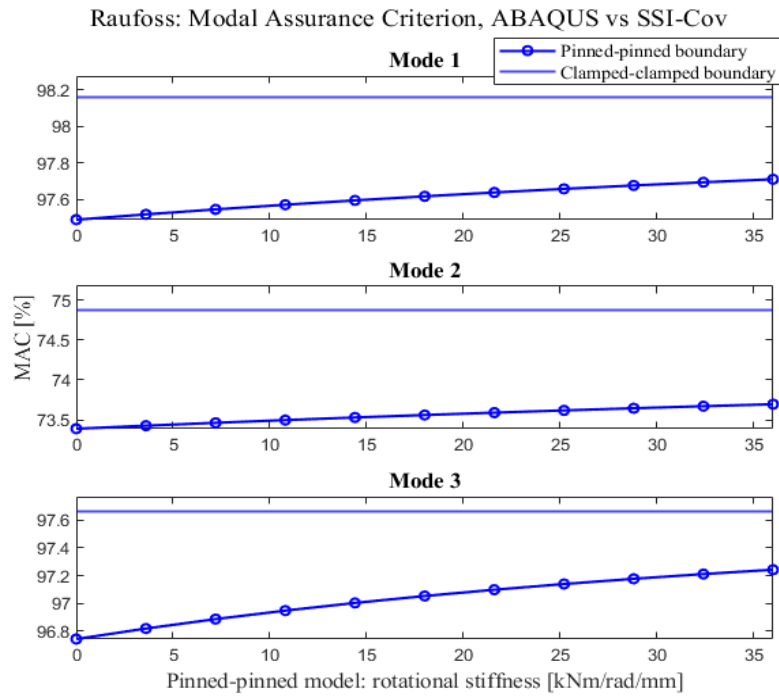


Figure 6.16: The MAC values between the mode shapes estimated by ABAQUS and SSI-Cov for Raufoss bridge.

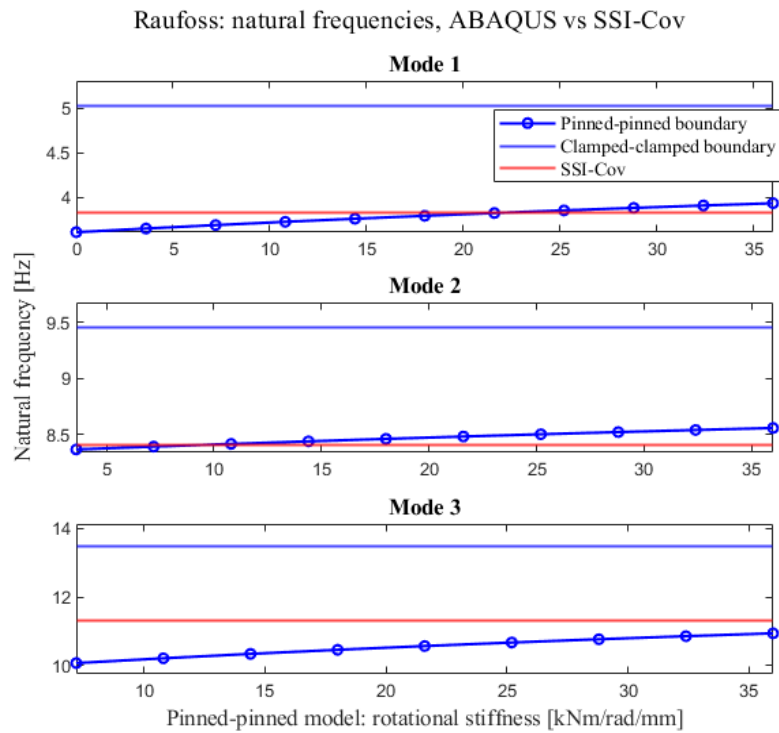


Figure 6.17: The natural frequencies estimated by ABAQUS and SSI-Cov for Raufoss bridge.

ABAQUS vs SSI-DD

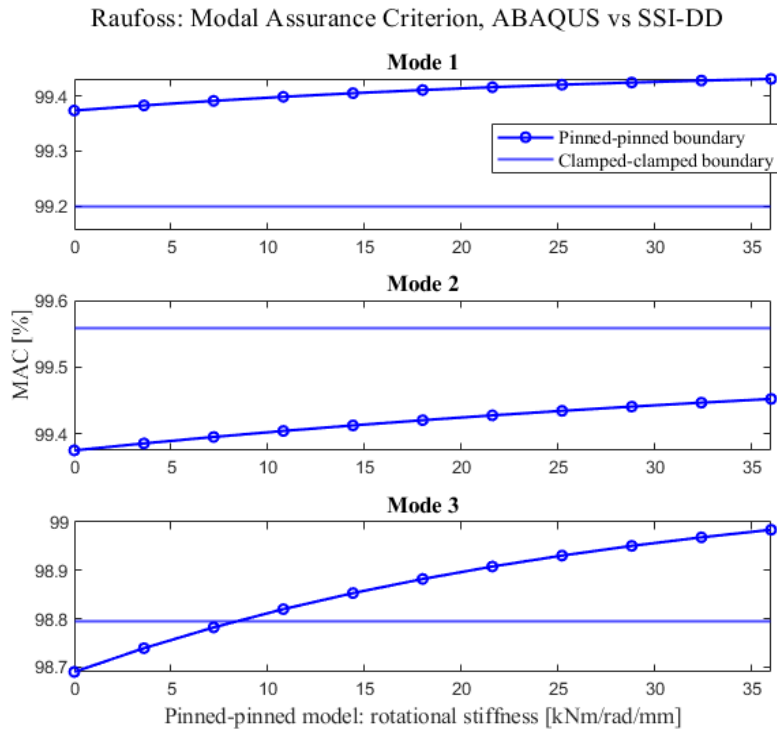


Figure 6.18: The MAC values between the mode shapes estimated by ABAQUS and SSI-DD for Raufoss bridge.

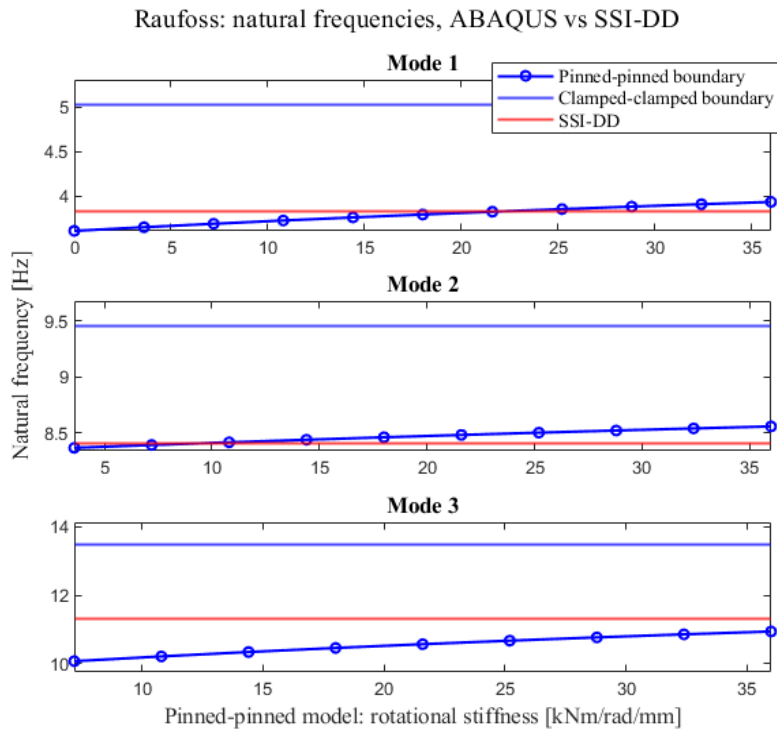


Figure 6.19: The natural frequencies estimated by ABAQUS and SSI-DD for Raufoss bridge.

Discussing data from the numerical model

The estimated natural frequencies were highly susceptible to additional rotational stiffness. The optimization process was employed on the first natural frequency as this mode laid within the human induced frequency range defined in section 3.8. Considering that all three modal analysis techniques yielded similar natural frequencies for the first mode, as presented in previous sections, the optimized rotational stiffness of approximately 21.6 kNm/rad/mm evidently applied for all three modal analysis techniques, as presented in figure 6.15, 6.17, and 6.19.

The optimized rotational stiffness yielded inferior results for modes two and three. The second natural frequency didn't vary much for the studied rotational stiffnesses, but the most accurate estimate was for a rotational stiffness for approximately 7 kNm/rad/mm . The third natural frequency was extremely sensitive to additional rotational stiffness and was initially drastically underestimated. The third natural frequency from ABAQUS converged towards the estimated natural frequency as the stiffness was increased. The optimal rotational stiffness laid outside of the studied stiffness range in this thesis. The natural frequencies derived for clamped edges were significantly higher than the estimated frequencies. This indicates that the asphalt pavement solely adds some rotational stiffness.

Investigating the MAC values presented in figure 6.14, 6.16, and 6.18, it became apparent that ABAQUS accurately managed to estimate similar mode shape as BFD, SSI-Cov, and SSI-DD. The only mode not accurately estimated was the second mode shape estimated by SSI-Cov. This mode has, however, previously been identified as abnormal, and the low MAC value was therefore expected. Additional rotational stiffness didn't significantly influence the accuracy of the mode shapes. The reasoning for the slow convergence will be further discussed in section 6.3. The improvement of the MAC value was minimal, and all rotational stiffnesses yielded excellent representations of the mode shapes. One surprising difference between the results was that the MAC value decreased for BFD and SSI-DD when the boundary condition was assumed to be clamped. This indicated that the estimated mode shapes were not entirely clamped. SSI-Cov, on the other hand, yielded superior MAC values as the boundary conditions were regarded as clamped. It's however worth noting that assuming clamped boundary conditions slightly improved the MAC value, yet drastically decreased the accuracy of the natural frequencies.

Extrapolating the model for other temperatures

Raufoss bridge was analyzed for an assumed temperature of 3°C . However, an increase in temperature would result in a decrease in natural frequencies due to the reduced stiffness of the asphalt pavement. The extrapolation of the first natural frequency was computed for temperatures varying between 0°C and 40°C for an assumed loading frequency of 4.0 Hz. The rotational stiffness was not calibrated for different temperatures. Therefore, natural frequencies were estimated for a rotational stiffness equal to the optimized stiffness derived for 3°C , 21.6 kNm/rad/mm . The result is presented in figure 6.20

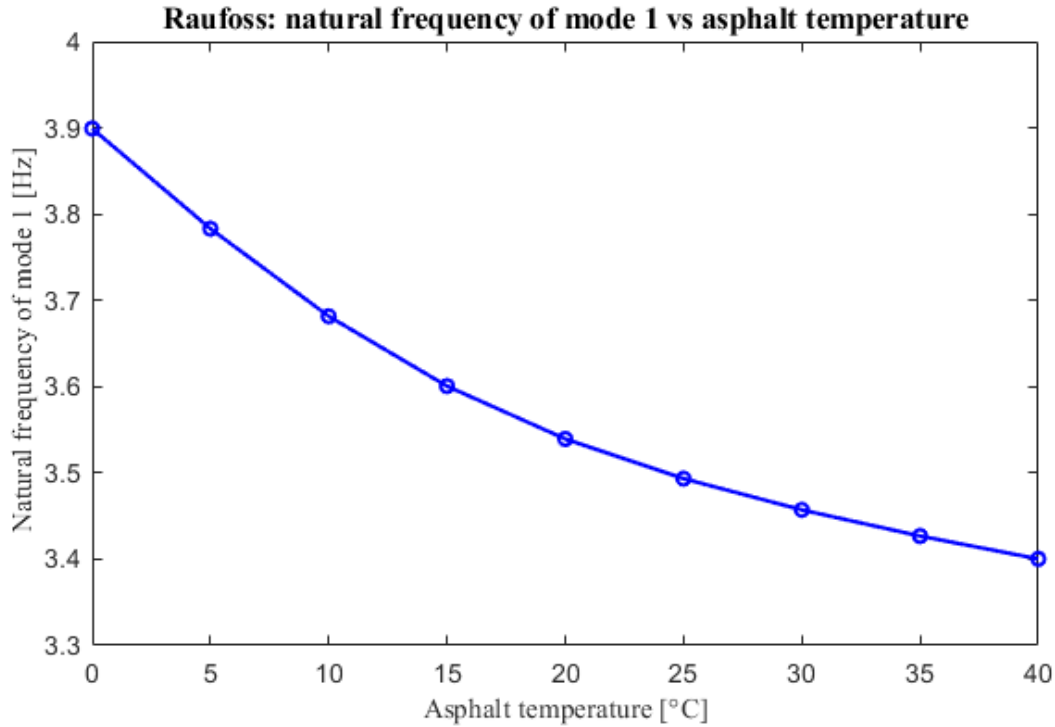


Figure 6.20: The first natural frequency plotted as a function of the asphalt pavement's temperature while subjected to a loading frequency of 4 Hz.

As expected, the natural frequency decreased as the temperature increased. This was caused by the reduced stiffness of the asphalt pavement. The true natural frequency is, however, expected to be lower than what the graph predicts, as it is assumed that the rotational stiffness will be reduced as the asphalt's stiffness decreases. As the bridge was only measured for one temperature, the temperature dependency of the rotational stiffness could not be modeled.

6.1.4 Comfort Criterion

The first natural frequency was well within the human induced frequency range. The first mode must therefore fulfill the comfort criterion defined in EC 1995-2. The natural frequency was assumed to be between 2.5 and 5.0 Hz for all relevant temperatures. The total mass of the bridge, neglecting the railing and other installed components, was approximated to 33.7 tons. The estimated vertical acceleration for a single pedestrian crossing the bridge assuming a modal damping ratio of 1.5% was derived as follows:

$$a_{vert,1} = \frac{100}{M\xi} = \frac{100}{33700 \cdot 0.015} \approx 0.20 \text{ m/s}^2.$$

This acceleration was converted into an acceleration for a constant stream of pedestrians crossing the bridge as follows:

$$a_{vert,n} = 0.23 \cdot a_{vert,1} \cdot 0.6 \cdot A \cdot k_{vert} = 0.23 \cdot 0.20 \cdot 0.6 \cdot 4.046 \cdot 22 \cdot 0.6 \approx 1.47 \text{ m/s}^2.$$

The vertical acceleration caused by a single pedestrian walking across the bridge was well below the comfort criterion of 0.7 m/s^2 defined by the standard. However, the comfort criterion for a constant stream of pedestrians crossing the bridge was significantly larger than the maximum acceleration allowed. The SSI methods estimated a damping ratio exceeding 4.4% for the first mode. A damping ratio of 1.5% was therefore assumed to be conservative since the damping is expected to increase as the temperature increases. The damping ratio needs to be checked for lower temperatures to verify that the damping ratio exceeds 3.2% for the comfort criterion to be fulfilled. By assuming a modal damping ratio of 4.4%, the crowd induced acceleration was estimated to be 0.5 m/s^2 and therefore within the comfort criterion.

Higher temperatures result in the first natural frequency dropping below 3.5 Hz, as predicted by the extrapolation presented in figure 6.20. This may prove critical as $a_{vert,1}$ now needs to be estimated for a pedestrian running instead of walking. This results in the acceleration, $a_{vert,1}$, increasing by a factor of six. If the damping ratio is assumed to be 4.4%, the maximum number of people that can jog across the bridge simultaneously, assuming a natural frequency of 3.5 Hz, is estimated as follows:

$$a_{vert,n} = 0.23a_{vert,1}nk_{vert} = 0.23\frac{600}{M\xi}nk_{vert}$$

$$n = \frac{a_{vert,n}M\xi}{0.23 \cdot 600 \cdot k_{vert}} = \frac{0.7 \cdot 33700 \cdot 0.044}{0.23 \cdot 600 \cdot 0.6} = 12.5.$$

The calculation indicates that twelve people may jog across the bride simultaneously for the given natural frequency. As there is some uncertainty as to the actual natural frequency of the bridge for higher temperatures, the extreme scenario of a natural frequency of 2.5 Hz was investigated. This assumption resulted in a maximum of seven people could jog across the bridge simultaneously.

6.2 Brumunddal Bridge

6.2.1 Basic Frequency Domain Method

This section will investigate the BFD method employed on data sets from two different excitation methods performed on Brumunddal pedestrian bridge; Jumping Test and Modal Hammer Test.

Jumping Test data

The Basic Frequency Domain method was employed on the data set from the Jumping Test to estimate the natural frequencies and the mode shapes of Brumunddal pedestrian bridge. To simplify the peak-picking process, the PSD plot was smoothed out. Welch's method with four divisions was utilized, and the result is plotted in figure 6.21. The PSD plot clearly identified two modes, presented by red dots. The estimated displacement-normalized mode shapes are illustrated in figure 6.22, while the corresponding natural frequencies are presented in table 6.6.

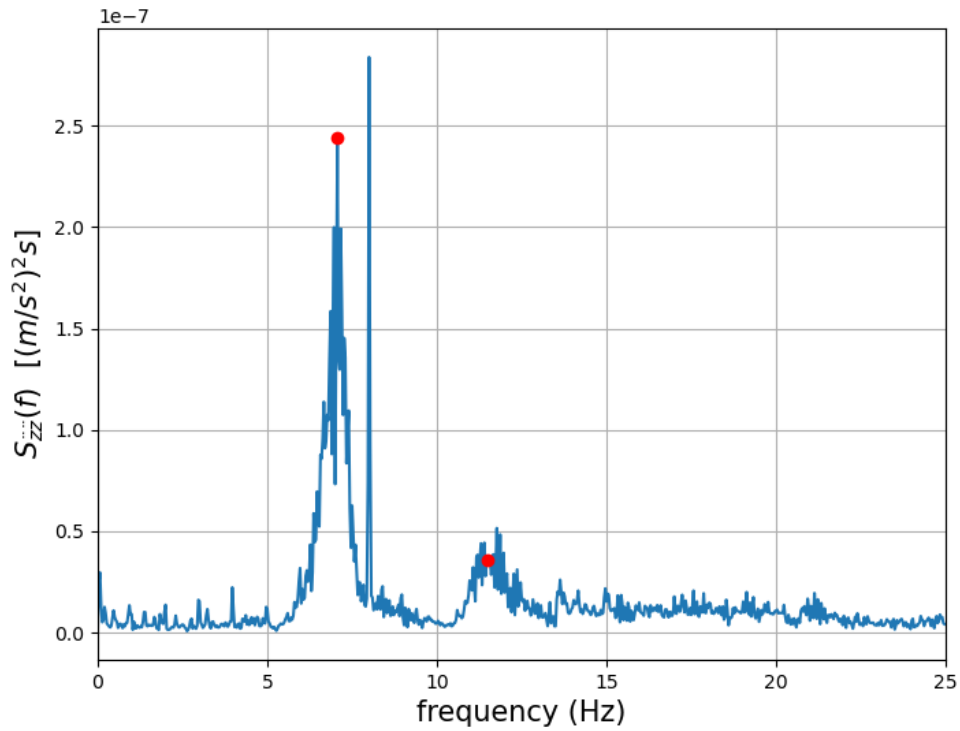


Figure 6.21: Power Spectral Density plot for sensor 5 obtained using the BFD method on the Jumping Test Data.

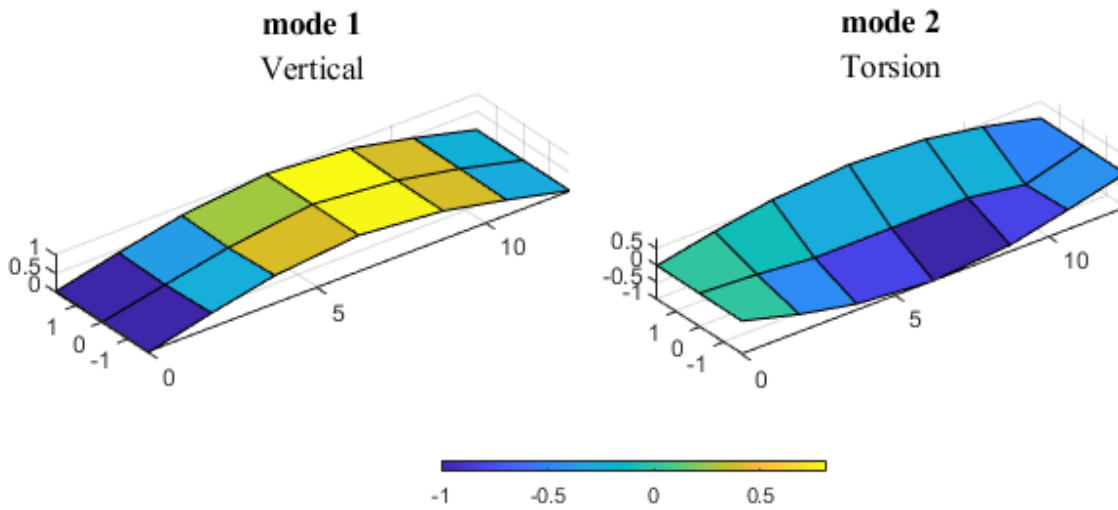


Figure 6.22: The displacement-normalized mode shapes of Brumunddal bridge estimated by the BFD method using Jumping Test Data.

Table 6.6: The natural frequencies of Brumunddal bridge estimated from the PSD plot of the Jumping Test data.

Mode "i"	f_i [Hz]	Type
1	7.0667	Vertical
2	11.5000	Torsion

Modal Hammer Test data

The Modal Hammer Test time series was noisy, which resulted in a coarse PSD plot. To perform the peak-picking process more easily, Welch's method with 30 divisions was applied. The final PSD plot is presented in figure 6.23. Three well defined modes were identified from the plot presented by colored dots. Estimated natural frequencies are presented in table 6.7, while the corresponding mode shapes are illustrated in figure 6.24.

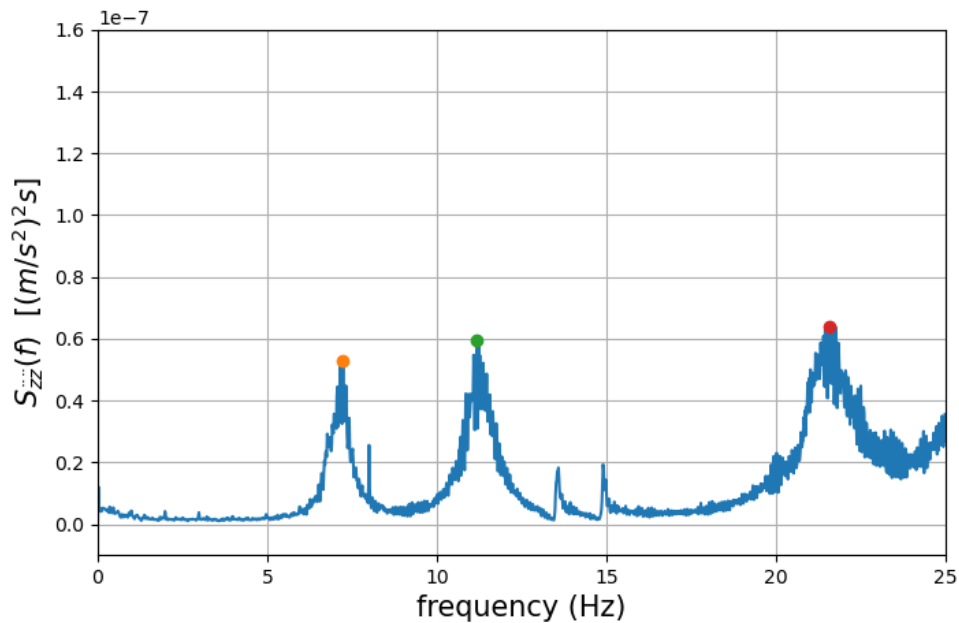


Figure 6.23: Power Spectral Density plot for sensor 4 obtained by the BFD method on the Modal Hammer Test data.

Table 6.7: The natural frequencies of Brumunddal bridge derived using the Modal Hammer Test data.

Mode "i"	f_i [Hz]	Type
1	7.2333	Vertical
2	11.1833	Torsion
3	21.5833	Vertical

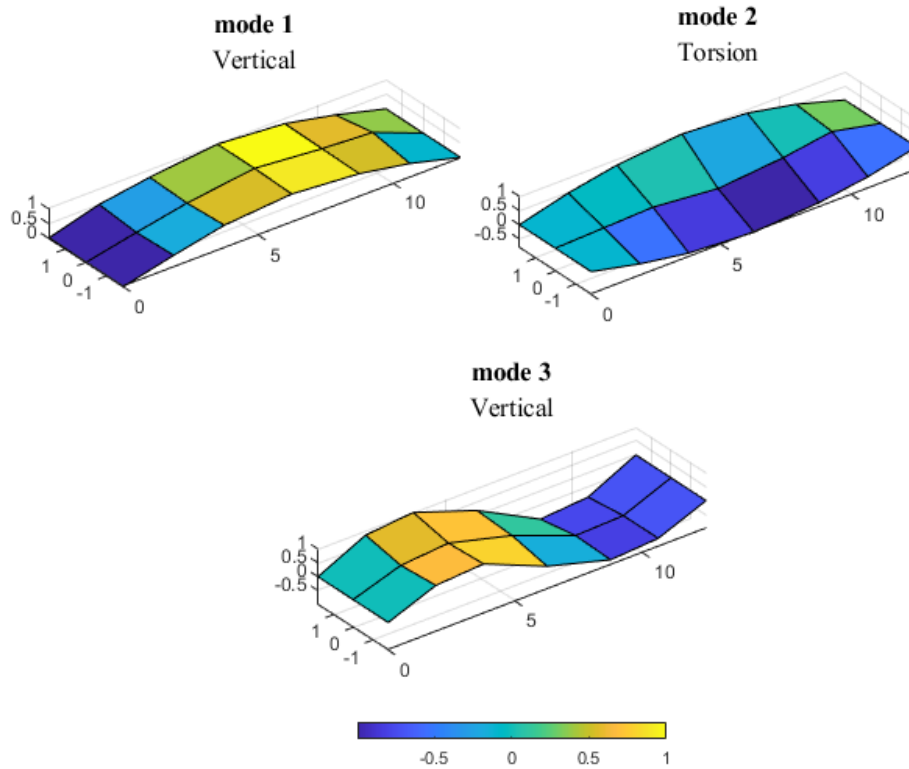


Figure 6.24: The displacement-normalized mode shapes of Brumunddal bridge estimated by BFD method using MHT data.

Comparing the results from the excitation methods

The MHT results identified a mode not present in the results from the Jumping Test. The mode shape of the missing mode doesn't exhibit deformation at the midspan, and thus wasn't excited by the Jumping Test solely consisting of jumps at the midspan. The roving hammer was, on the other hand, moved around the bridge deck thus exciting more modes. More modes were therefore expected to be identified from the MHT time series.

The results indicated deviations between the natural frequencies estimated from the two excitation methods. The estimated natural frequencies were similar, yet the deviation was greater than initially expected. This deviation may have been caused by noise and/or inaccuracies in the peak-picking process. Even after the PSD plots were smoothed out, there were still uncertainties over the exact peak locations. Additionally, the smoothing process may have induced inaccuracies due to the edge effects introduced by Welch's method.

The mode shapes were clearly sinusoidal, as was expected. However, there seemed to be marginal inaccuracies for the second mode shape. This inaccuracy was very noticeable for the Jumping Test data, presented in figure 6.22, and it could be related to the inaccuracy in the peak-picking process.

Lastly, both PSD plots indicated a narrow spike located at approximately 8 Hz. Narrow spikes tend to represent modes with low damping ratios. Additionally, the MHT data indicated two peaks with natural frequencies of approximately 13 and 15 Hz, respectively. These were not present from the Jumping Test, and their validity were put into question. Several of these modes were also identified by the SSI methods, as will be presented later. These modes will be further investigated in section 6.2.2.

6.2.2 Stochastic Subspace Identification SSI

This section will present and discuss the dynamic properties of Brumunddal bridge estimated by employing the Stochastic Subspace Identification methods. Due to the Jumping Test data not being able to represent all modes, solely the truncated data set from the MHT was analyzed.

Stabilization diagrams

Stabilization diagrams were plotted for both Covariance-Driven Stochastic Subspace Identification and Data-Driven Stochastic Subspace Identification for a frequency range of 0 to 25 Hz and 0 to 35 Hz, respectively. The data was analyzed using 150 block rows for model orders varied between 0 and 400 with a spacing of 1. To easily compare the alignment of the modes to the frequency content of the data, the Power Spectral Density was plotted in the background.

The stabilization diagram estimated by the SSI-Cov method is presented in figure 6.25. The diagram identified four modes within the frequency range of interest. The first, third, and fourth modes were all stable from model order 100. The second mode didn't stabilize before a model order of 150. This mode was infested by spurious poles, represented by red dots. The validity of this mode will be further investigated later.

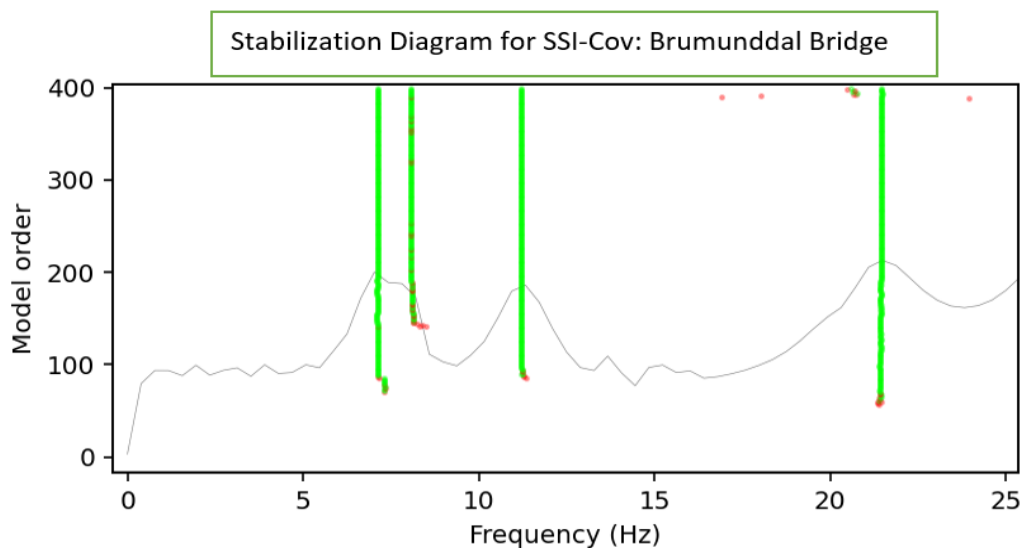


Figure 6.25: Stabilization diagram of Brumunddal bridge using SSI-Cov with number of block rows equal to 150.

The stabilization diagram estimated by SSI-DD is presented in figure 6.26. Five modes may be identified from the diagram within the frequency of 0 to 25 Hz. The stabilization diagram, however, presented modes up to a natural frequency of 35 Hz. This was done to simplify the process of identifying spurious modes. The fourth mode was not identified by SSI-Cov. The mode was heavily infested by spurious poles and will require further investigation to be validated. Similarly to the stabilization diagram from SSI-Cov, the second mode stabilized, but was infested by spurious poles. The other three modes stabilized by model order 100 and corresponded well with the previously identified modes by SSI-Cov.

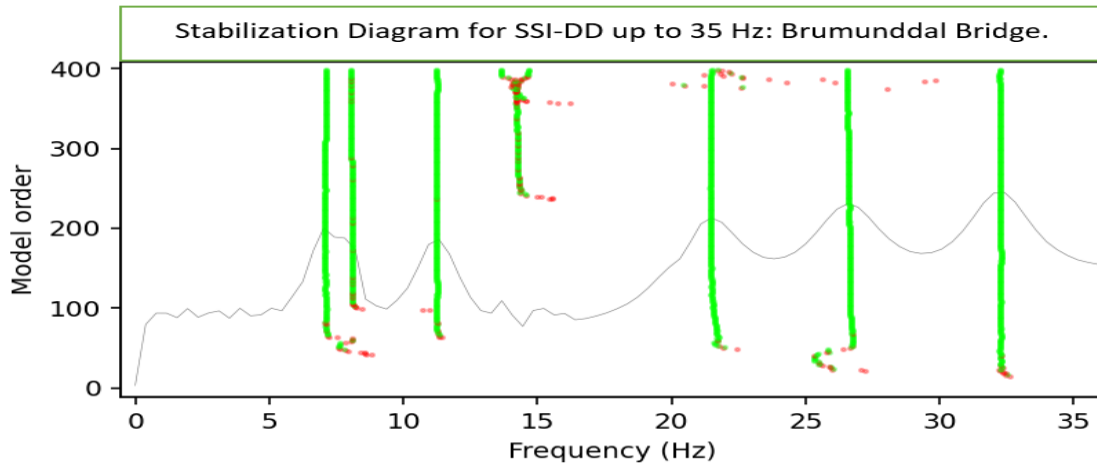


Figure 6.26: Stabilization diagram of Brumunddal bridge using SSI-DD with number of block rows equal to 150.

Possible physical modes

Two modes stuck out from the stabilization diagrams and required further investigation. The second mode present in both stabilization diagrams required higher model orders to stabilize compared to other identified modes. Additionally, this mode was infested by many spurious poles, which typically indicates that the mode may be spurious. Likewise, the fourth mode identified in figure 6.26 struggled to stabilize. The mode was heavily infested by spurious poles and seemed to separate as the model order approached 400.

The second mode identified from SSI-Cov and SSI-DD was studied first. The mode had an average natural frequency of 8.07 Hz for both SSI methods. The PSD plots presented in section 6.2.1 indicated narrow spikes for this frequency. Modes with narrow spikes in the frequency domain tend to have low damping. The modal damping ratios derived using the SSI methods were plotted as functions of the model order and the results are presented in figure 6.28, while the identically normalized mode shapes are presented in figure 6.27.

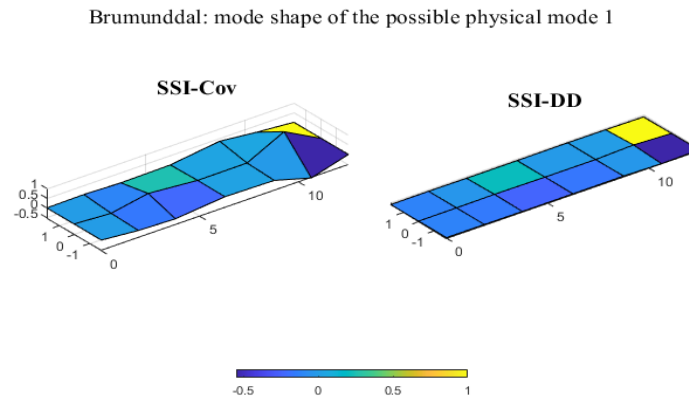


Figure 6.27: The mode shape of the possible physical mode of Brumunddal bridge estimated by SSI-Cov and SSI-DD

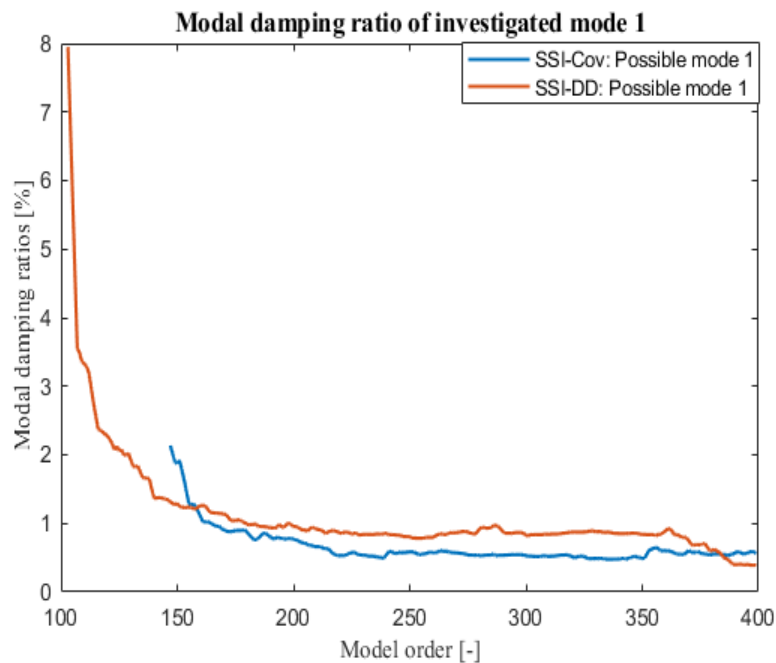


Figure 6.28: The damping ratio of the possible physical mode of Brumunddal bridge estimated by the SSI methods.

The graph above indicates that the modal damping ratio stabilizes at 0.6% for SSI-Cov. The damping ratio initially seems to stabilize at approximately 1% for SSI-DD. However, the ratio collapses as the model order approaches 400. Both methods should technically stabilize towards the same damping value indicating that the damping ratios are yet to stabilize. Such low damping ratios seem unrealistic for a SLT deck mode. The analyzed data may only represent vertical and torsional modes. The mode shapes illustrated in figure 6.32 indicate that this mode can be neither vertical nor torsional as there are no missing mode shapes. Due to the low estimated modal damping ratios, the inability for the damping ratio from SSI-DD to stabilize, and the other modes not allowing the mode to be a vertical or torsional mode shape, the mode will not be regarded as a mode belonging to the bridge deck. The mode will be disregarded in

further calculations, but will be further discussed in section 6.3.

The stabilization diagram from SSI-DD, figure 6.26, presents a mode with natural frequency of approximately 14.2 Hz. As the model order approaches 400, the mode separates into two modes. These modes may be identified from the PSD plot from the Modal Hammer Test data presented in figure 6.3. The modes are infested by unstable poles resulting in the validity of the modes being put into question. The model order limit was changed to 600 for the modes to properly separate, while the number of block rows remained unchanged at 150. The new stabilization diagram is presented in figure 6.29. The two modes have mean natural frequencies of 13.46 Hz and 14.80 Hz, respectively. The convergence of the damping ratios were investigated by plotting the damping ratios as functions of the model order as seen in figure 6.30.

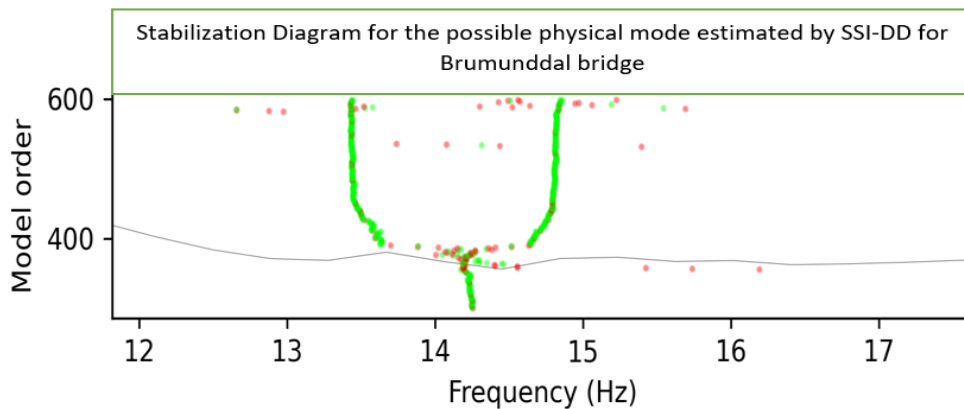


Figure 6.29: Stabilization diagram of Brumunddal bridge for the investigated mode using SSI-DD with number of block rows equals 150.

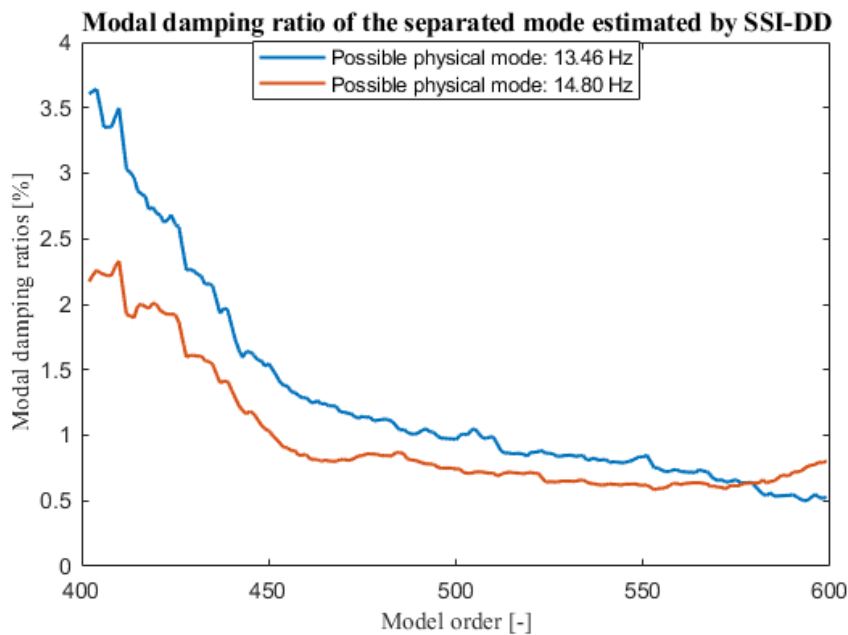


Figure 6.30: The damping ratio of the possible physical mode of Brumunddal bridge estimated by SSI-DD.

As indicated in figure 6.30, the modal damping ratios stabilize at approximately 0.5% and 0.8%, respectively. These low damping ratios are emphasised by the PSD plots from the MHT data, where the same natural frequencies are presented as narrow spikes. The modes were therefore expected to have low damping ratios. The damping ratios of the separated modes were significantly low compared to the modal damping ratios associated with the well-defined modes later presented in figure 6.36. Similarly as for the argumentation for the second mode, only vertical and torsional modes may be represented by the input data and sensor layout. The mode shapes for the three identified mode shapes are presented in figure 6.32. These mode shapes indicate that the investigated modes may not be a vertical mode. The frequency range for the stabilization diagram estimated with SSI-DD was increased to include the second torsional mode which has a mean natural frequency of 26.60 Hz. The mode shape is plotted in figure 6.31 clearly indicating that the investigated modes can't be torsional. The investigated modes are consequently assumed to not belong to the bridge deck and were thus neglected in further calculations.

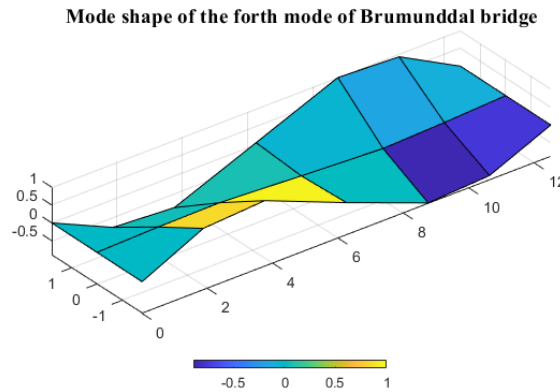


Figure 6.31: Mode shape of the mode with natural frequency of approximately 26.60 Hz for Brumunddal bridge estimated by SSI-DD.

Mode shapes

Mode shapes were picked based on the poles with the highest MPC values, as previously stated for Raufoss bridge. The mode shapes were normalized and are illustrated in figure 6.32. Dynamic properties of the picked poles are presented in table 6.8.

Table 6.8: Dynamic properties of the poles with the highest MPC values fro SSI-Cov and SSI-DD.

Mode "i"	SSI-Cov			SSI-DD		
	MPC _{max} [%]	f _{i,MPC_{max}} [Hz]	ξ _{i,MPC_{max}} [%]	MPC _{max} [%]	f _{i,MPC_{max}} [Hz]	ξ _{i,MPC_{max}} [%]
1	99.51	7.1135	4.66	96.97	7.0968	5.27
2	99.97	11.2045	4.59	99.73	11.2482	4.71
3	99.84	21.4644	4.11	99.74	21.4945	4.11

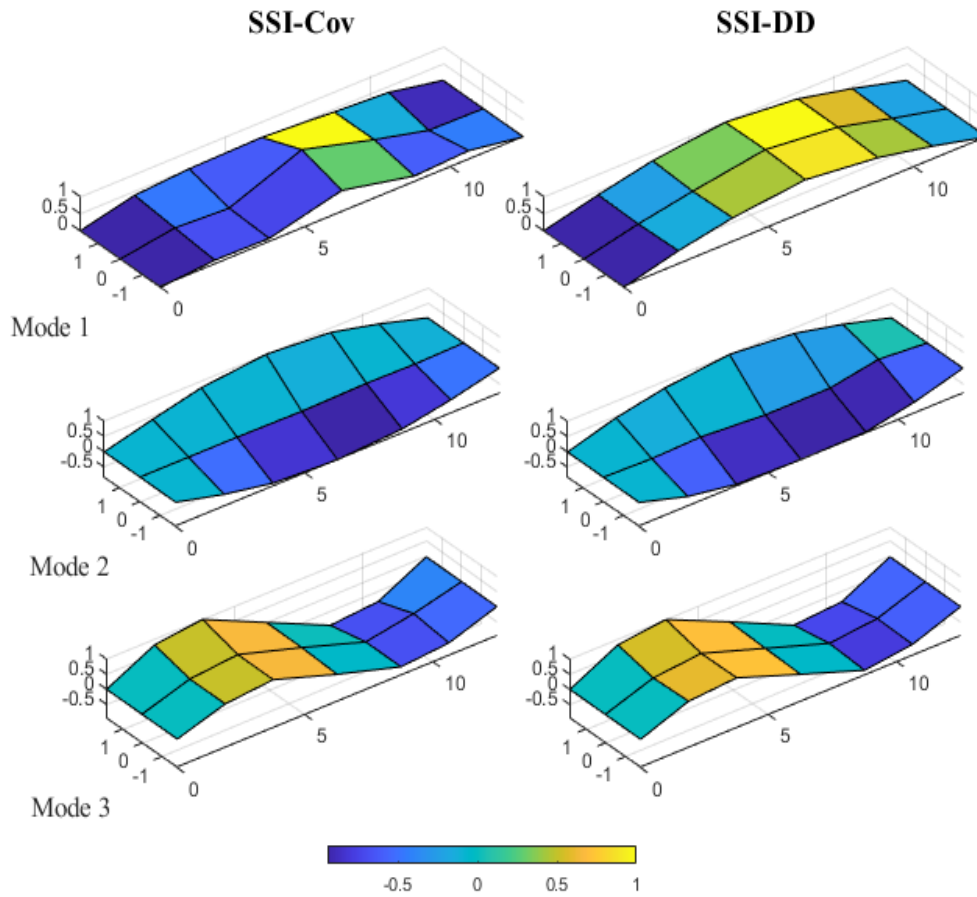


Figure 6.32: The mode shapes of Brumunddal bridge corresponding to the highest MPC value, estimated by SSI-Cov and SSI-DD.

Figure 6.32 indicates that both SSI-Cov and SSI-DD accurately identified whether the modes were vertical or torsional. However, SSI-Cov struggled to accurately predict the first mode shape. The first mode was expected to be shaped as half a sinus wave with a bit of clamping effect at each end, such as can be seen from the results from SSI-DD. There are no clear indications why this inaccuracy occurred by studying the values given in table 6.8. Both the natural frequency and modal damping ratio correspond well with the estimated values for the first mode. Further investigations demonstrated that the pole with the highest MPC also had the highest MAC value compared to the mode shape estimated by SSI-DD of approximately 80%. The first mode is relatively closely spaced to the identified mode with a natural frequency of 8.07 Hz assumed to be spurious in the previous section. Comparing the first mode shape for SSI-Cov and the assumed spurious mode, presented in figure 6.27, it becomes apparent that the sensors yielding strange results for the first mode shape are emphasized in the spurious mode shape. This could indicate that the spurious mode absorbs energy intended for the first mode shape. The mode shape from SSI-DD was normalized by the same value as the mode shape estimated by SSI-Cov. The figure clearly illustrates that the mode shape from SSI-DD hardly absorbs any energy explaining why SSI-Cov struggled to accurately estimate the first mode shape, while SSI-DD did. To further investigate this hypothesis, the time series was analyzed

for the number of block rows equal to 50 and model orders ranging from 0 to 400. The picked first mode shape is illustrated in figure 6.33.

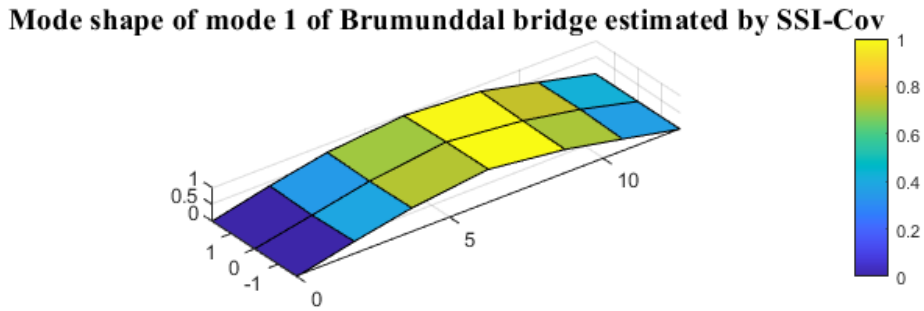


Figure 6.33: Mode shape of the first mode of Brumunddal bridge estimated by SSI-Cov with 50 as the number of block rows.

The newly estimated mode shape looks identical to the one originally estimated by SSI-DD. The improvement of the mode shape was most likely caused by the assumed spurious mode failing to stabilize due to the low number of block rows. The mode, therefore, absorbed little energy. Even though the mode shape improves, the low number of block rows yields inferior results for natural frequencies and damping ratios.

Natural frequencies

The presumed stable poles with model orders greater than 100 were used to estimate the natural frequencies of the three modes. The mean values, mode values, and standard deviations were derived for each mode and the results are presented in table 6.9. Histograms of the estimated natural frequencies are presented in figure 6.34. The mean natural frequencies estimated for the different modes by the SSI methods are presented in the histograms as red lines.

Table 6.9: Mean values, mode values, and standard deviations of the estimated natural frequencies of Brumunddal bridge derived using SSI-Cov and SSI-DD.

Mode "i"	SSI-Cov			SSI-DD		
	$f_{i,\text{mean}}$ [Hz]	$f_{i,\text{mode}}$ [Hz]	Δf_i [Hz]	$f_{i,\text{mean}}$ [Hz]	$f_{i,\text{mode}}$ [Hz]	Δf_i [Hz]
1	7.1142	7.1093	0.0087	7.0890	7.0840	0.0063
2	11.1991	11.2019	0.0041	11.2350	11.2418	0.0145
3	21.4478	21.4547	0.0092	21.4566	21.4468	0.0233

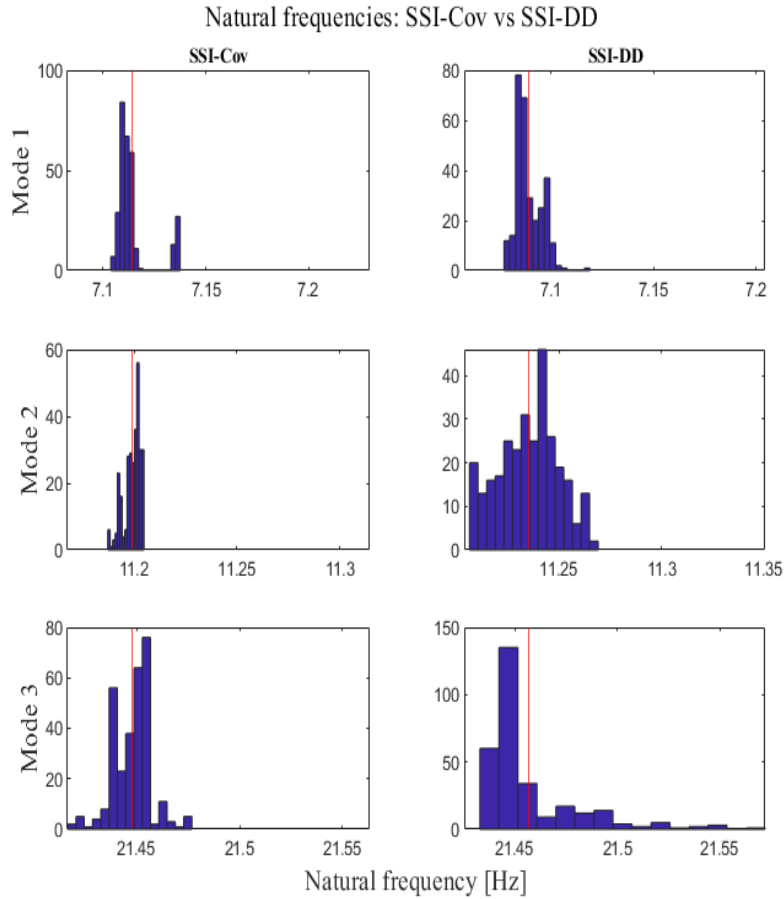


Figure 6.34: Histograms of the natural frequencies of Brumunddal bridge estimated by the SSI methods.

Table 6.9 indicated little deviation between the natural frequencies estimated using mean and mode values for both SSI methods. There were additionally minimal differences between the natural frequencies derived using SSI-Cov and SSI-DD. However, there was significantly less deviation between the natural frequencies derived by employing SSI-Cov compared to SSI-DD as presented by the histograms. This results in the standard deviation for SSI-Cov being significantly smaller than the standard deviations derived for SSI-DD.

Modal damping ratios

Damping ratios were, similarly to the natural frequencies, estimated through the use of mean values, mode values, and standard deviations. The estimated values are presented in table 6.10. To represent the uncertainty in the estimated damping ratios, the spread of the ratios are presented in histograms presented in figure 6.35. Figure 6.36 plots the damping ratios functions of the model order in order to study the convergence of the damping ratios.

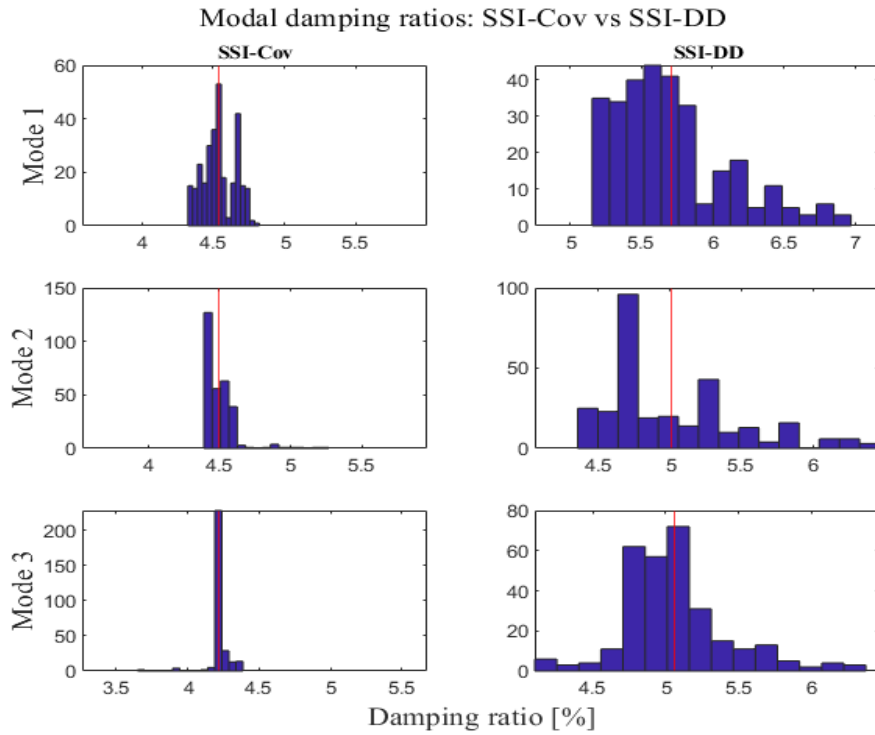


Figure 6.35: Histograms of the estimated modal damping ratios of Brumunddal bridge by the SSI methods.

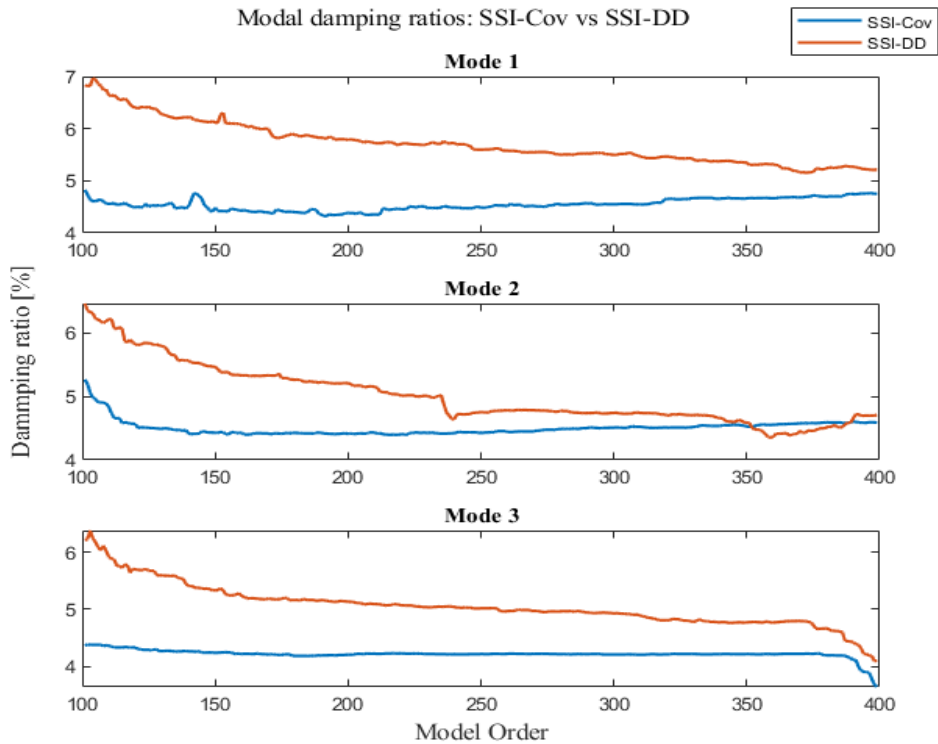


Figure 6.36: The modal damping ratios of Brumunddal bridge plotted as functions of the model order estimated by the SSI methods.

Table 6.10: Mean values, mode values, and standard deviations of the modal damping ratios of Brumunddal bridge derived using the SSI methods.

Mode "i"	SSI-Cov			SSI-DD		
	$\xi_{i,\text{mean}}$ [%]	$\xi_{i,\text{mode}}$ [%]	$\Delta\xi_i$ [%]	$\xi_{i,\text{mean}}$ [%]	$\xi_{i,\text{mode}}$ [%]	$\Delta\xi_i$ [%]
1	4.54	4.54	0.11	5.72	5.58	0.40
2	4.50	4.42	0.11	5.02	4.71	0.47
3	4.22	4.21	0.08	5.06	5.09	0.36

The convergence plots presented in figure 6.36 indicate that SSI-DD overestimated the modal damping ratio for lower model orders and converged as the model order was increased. SSI-Cov, on the other hand, converged for lower model orders. Modal damping ratios estimated using SSI-DD were consistently larger compared to SSI-Cov, but the damping ratios from both SSI methods converged towards the same value as the model order was increased. The rapid convergence of SSI-Cov is evident from table 6.10 where the mean and mode value are practically identical in combination with the low standard deviation. The slow convergence of SSI-DD resulted in larger deviations between the mean and mode values as well as greater standard deviations. The histograms of the modal damping ratios clearly illustrate that the modal damping ratios for SSI-DD was significantly more unclear compared to SSI-Cov. The two first modal damping ratios converged towards approximately 4.8% and 4.6%, respectively. The damping ratio for the third mode was more uncertain as it initially seemed to converge. However, the damping ratio drastically decreased for SSI-Cov and SSI-DD when the model order approached 400. Higher model orders or a higher number of block rows are therefore required to accurately predict the convergence value of this mode.

6.2.3 Finite Element Model Comparison

The ABAQUS model was analyzed for rotational stiffnesses ranging from 0 to 13.5 $kNm/rad/mm$. Brumunddal bridge's parameters were presented in chapter 5, while the material properties were defined in section 4.3. The following graphs compare the natural frequencies and MAC values from the ABAQUS model as a function of rotational stiffness compared with the result estimated from BFD, SSI-Cov, and SSI-DD, respectively. Similarly as for the Raufoss bridge, solely frequencies under 15 Hz were considered thus only the first two modes were considered.

ABAQUS vs BFD

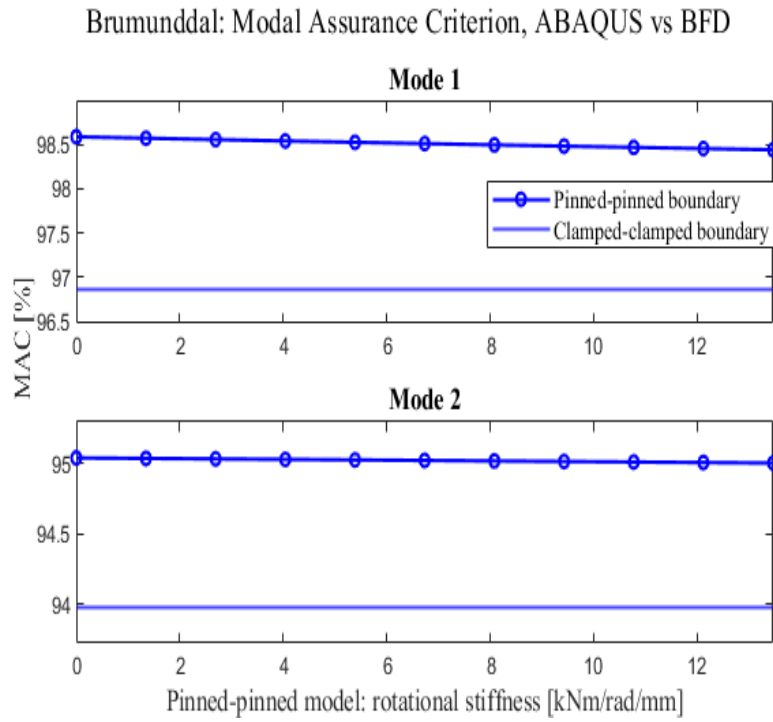


Figure 6.37: The MAC values between the mode shapes estimated by ABAQUS and BFD for Brumunddal bridge.

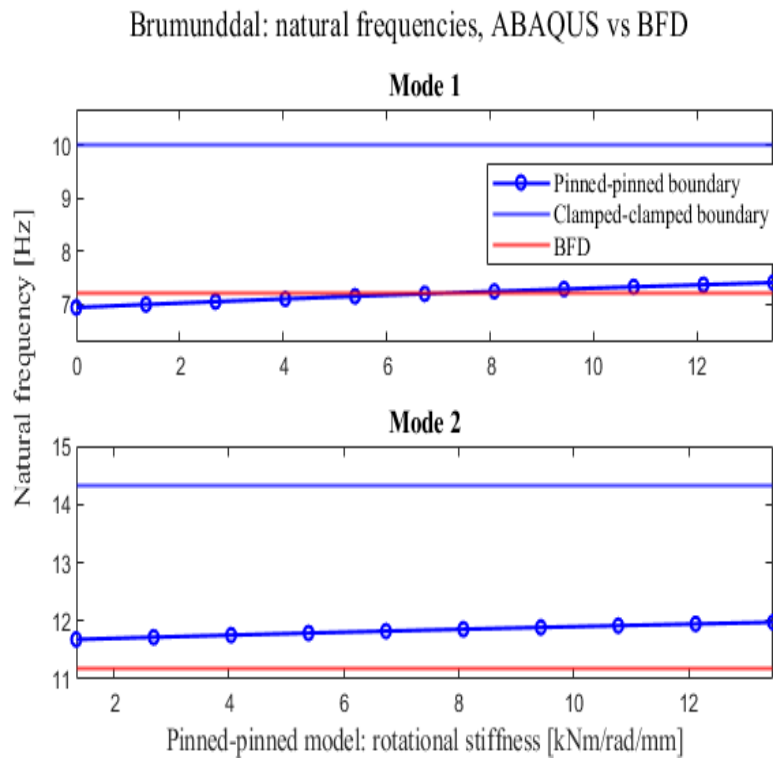


Figure 6.38: The natural frequencies estimated by ABAQUS and BFD for Brumunddal bridge.

ABAQUS vs SSI-Cov

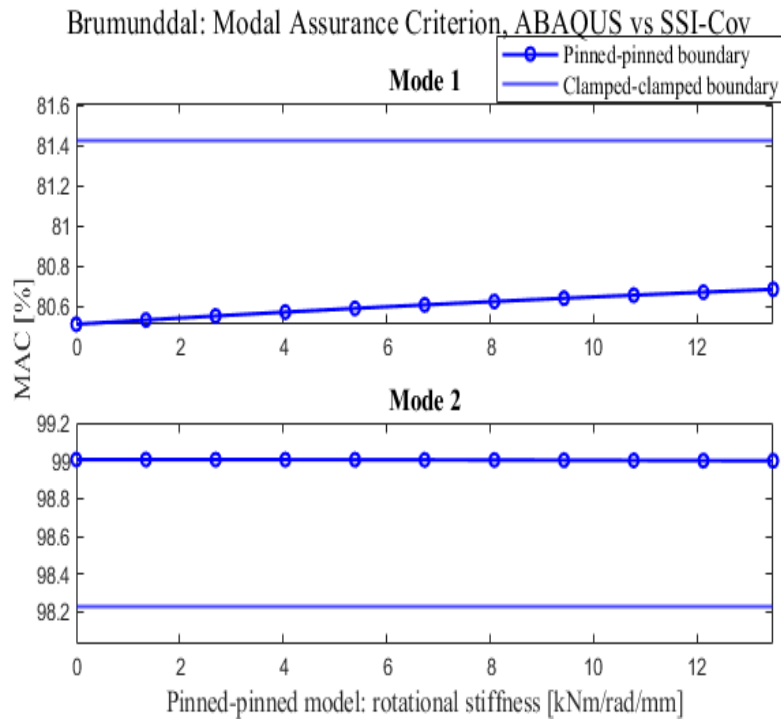


Figure 6.39: The MAC values between the mode shapes estimated by ABAQUS and SSI-Cov for Brumunddal bridge.

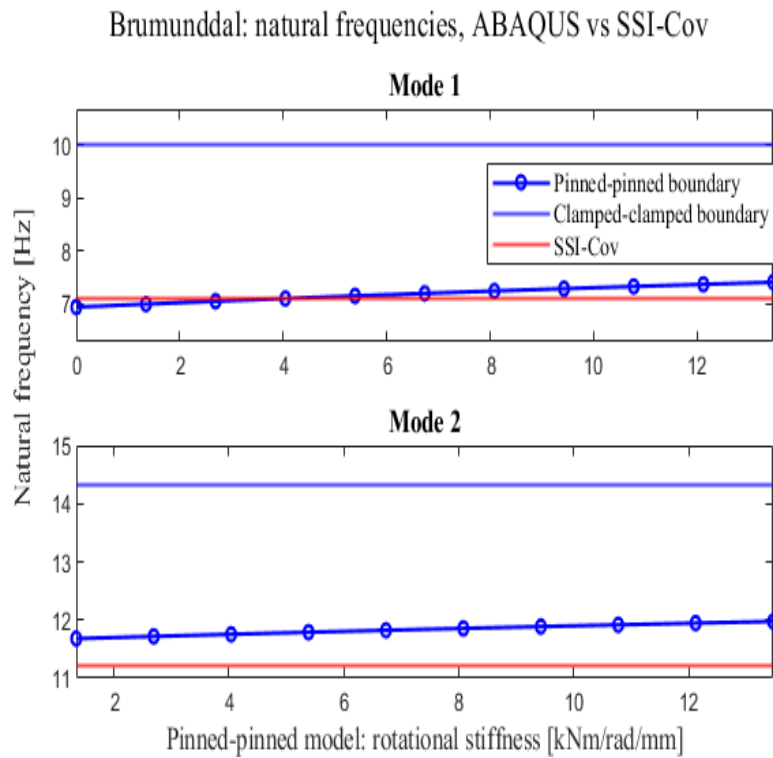


Figure 6.40: The natural frequencies estimated by ABAQUS and SSI-Cov for Brumunddal bridge.

ABAQUS vs SSI-DD

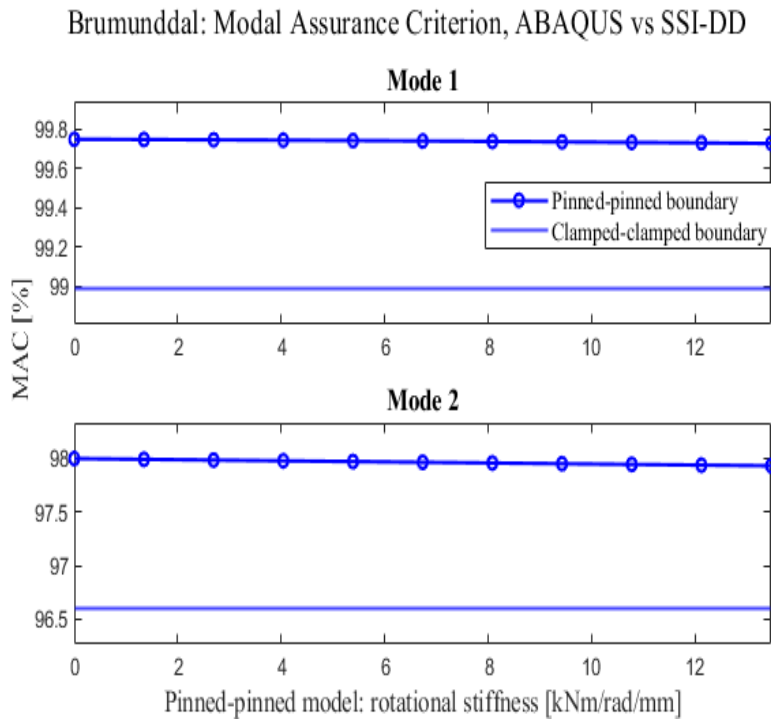


Figure 6.41: The MAC values between the mode shapes estimated by ABAQUS and SSI-DD for Brumunddal bridge.

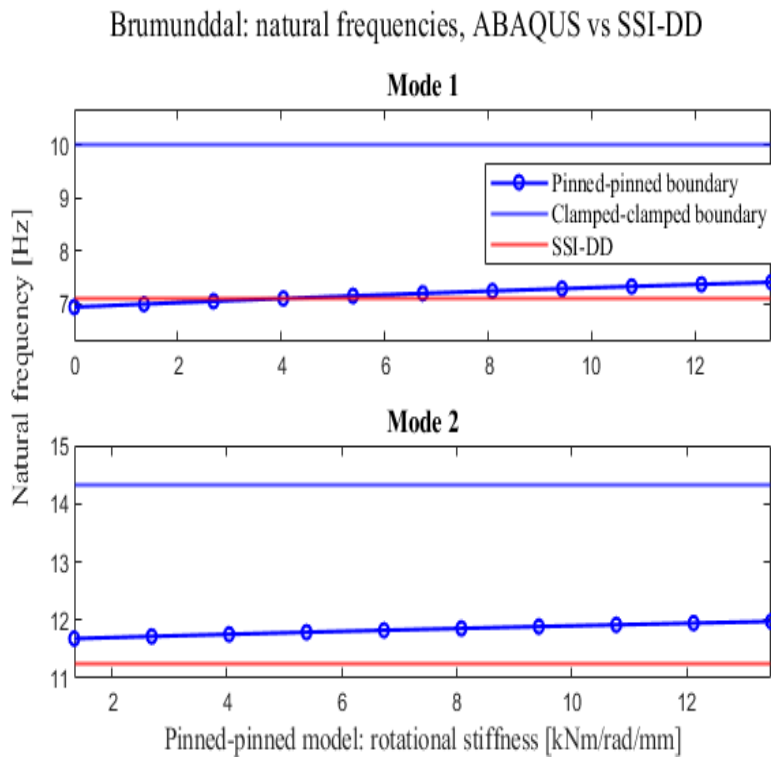


Figure 6.42: The natural frequencies estimated by ABAQUS and SSI-DD for Brumunddal bridge.

Discussing data from the numerical model

The ABAQUS model initially underestimated the first natural frequency for low rotational stiffness. As the rotational stiffness approached 6.7 kNm/rad/mm , the model accurately predicted the first natural frequency for BFD. The first natural frequency from SSI-Cov and SSI-DD was most accurately estimated for a rotational stiffness of approximately 4.0 kNm/rad/mm . The second natural frequency was, however, consistently overestimated compared to the estimates from all three modal analysis techniques. This error increased with the rotational stiffness. The optimized rotational stiffnesses yielded an error of approximately 5.7% for BFD and 4.9% for the SSI methods. The ABAQUS model drastically overestimated the natural frequencies when the boundary conditions were assumed to be clamped. This was expected as the analytical data indicated that the asphalt solely added some rotational stiffness to the bridge deck.

Investigating the development of the MAC values for the analyzed rotational stiffness range, indicated that the rotational stiffness hardly affected the mode shape. Results for the first mode shape from SSI-Cov were disregarded as this mode had previously been identified as having an unexpected mode. Therefore, the low MAC value was expected. All modes indicated a decrease in MAC value as the rotational stiffness increased, before stabilizing at a MAC estimated for clamped boundary conditions. All estimated MAC values were, however, over 95%. It was therefore evident that the ABAQUS model accurately managed to predict the accurate mode shapes of the bridge deck. The accuracy of the mode shapes will be further discussed in section 6.3.

Extrapolating the model for other temperatures

Natural frequencies and mode shapes previously extracted from ABAQUS, were estimated by assuming a temperature of 0.7°C and a loading frequency of 3.5 Hz. The bridge is expected to be subjected to higher temperatures during its lifespan. The first natural frequency was therefore estimated for temperatures ranging between 0 and 40°C . As the stiffness of the asphalt pavement is highly temperature dependent, the rotational stiffness that the bridge experiences is also assumed to be temperature dependent. Measurements were solely conducted for one temperature resulting in it being impossible to extrapolate the temperature dependency of the optimized rotational stiffness. Therefore, the previously optimized rotational stiffness of 4.0 kNm/rad/mm was assumed constant for all temperatures during the extrapolation. It is, however, assumed that the rotational stiffness will be reduced as the temperature increases. This would result in the extrapolating presented in figure 6.43 overestimating the true natural frequency.

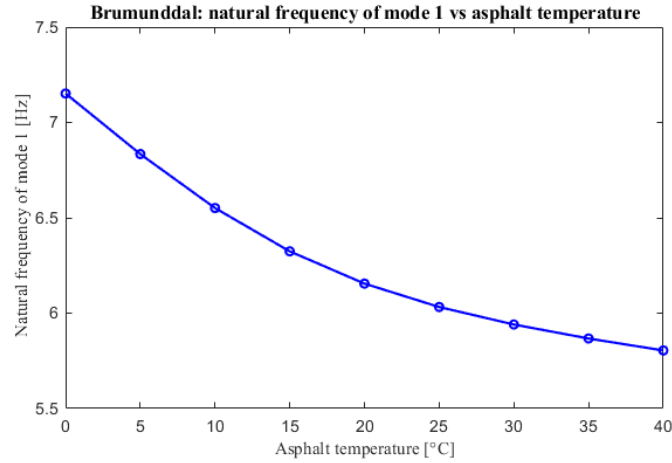


Figure 6.43: The first natural frequency plotted as a function of the asphalt pavement’s temperature while subjected to a loading frequency of 3.5 Hz.

6.2.4 Comfort Criterion

The Brumunddal bridge didn’t have any natural frequencies below 5 Hz and therefore exempt from the acceleration criterion for the analyzed temperature and loading frequency. However, the extrapolation indicated that the natural frequency approached 5 Hz for higher temperatures. As the extrapolation was done for a rotational stiffness equating the rotational stiffness estimated from SSI-Cov and SSI-DD for $0.7^{\circ}C$, it’s expected that the natural frequency was overestimated for higher temperatures.

If the first natural frequency drops below 5 Hz for higher temperatures, the comfort criterion for pedestrians crossing the bridge should be estimated. It’s considered highly unlikely that the bridge’s natural frequency will become lower than 3.5 Hz and will therefore not be analyzed for pedestrians running. The bridge has an estimated mass of approximately 12.8 tons. By assuming a modal damping ratio of approximately 1.5%, defined in the standard, the acceleration induced by a single pedestrian was estimated as follows:

$$a_{vert,1} = \frac{100}{M\xi} = \frac{100}{12,800kg \cdot 0.015} \approx 0.52 m/s^2.$$

The single pedestrian induces an acceleration below the limit of $0.7 m/s^2$. The acceleration for a continuous crowd crossing the bridge assuming a natural frequency of 4.5 Hz was estimated as follows:

$$a_{vert,n} = 0.23 \cdot a_{vert,1} \cdot n \cdot k_{vert} \approx 0.23 \cdot 0.52 \cdot 0.6 \cdot 3.885 \cdot 12.5 \cdot 0.2 \approx 0.7 m/s^2.$$

Assuming that the natural frequency may be as low as 4.5 Hz as the temperature increases, the acceleration criterion is fulfilled by using the standardized damping ratio of 1.5%. The damping ratio is assumed to increase as temperatures increase. As the damping ratio was estimated to approximately 4.8% for $0.7^{\circ}C$, it’s assumed that this ratio is conservative for temperatures where the natural frequency potentially could drop below 5 Hz. The bridge should, therefore, fulfill the comfort criterion for all relevant temperatures.

6.3 Final Comparison

The Modal Hammer Test data was analyzed with three different modal analysis techniques: BFD, SSI-Cov, and SSI-DD. All methods identified five modes for Raufoss and three modes for Brumunddal with natural frequencies lower than 25 Hz. Table 6.11 and 6.12 present the deviations between the estimated natural frequencies from the different methods. The tables indicate that the SSI methods yielded practically identical estimates of the natural frequencies. BFD, on the other hand, introduced more uncertainties due to the peak-picking process not being exact. The largest recorded deviation was, however, only 1.89%.

Table 6.11: The deviations in the natural frequencies of Raufoss bridge estimated by SSI-Cov, SSI-DD and BFD.

The deviations in the estimated natural frequencies of Raufoss bridge			
Mode "i"	SSI – Cov vs SSI – DD [%]	SSI – Cov vs BFD [%]	SSI – DD vs BFD [%]
1	0.02	0.04	0.06
2	0.02	0.88	0.86
3	0.02	0.95	0.92
4	0.04	0.28	0.32
5	0.00	0.13	0.13

Table 6.12: The deviations in the natural frequencies of Brumunddal bridge estimated by SSI-Cov, SSI-DD and BFD.

The deviations in the estimated natural frequencies of Brumunddal bridge			
Mode "i"	SSI – Cov vs SSI – DD [%]	SSI – Cov vs BFD [%]	SSI – DD vs BFD [%]
1	0.23	1.66	1.89
2	0.39	0.19	0.58
3	0.14	0.55	0.41

The small deviations between the mean natural frequency estimated by SSI-Cov and SSI-DD don't paint the entire picture. The natural frequencies estimated by SSI-Cov were more consistent compared to SSI-DD. This resulted in the standard deviation for SSI-Cov being significantly smaller compared to SSI-DD. The same reasoning applied for estimating the damping ratios. SSI-DD struggled to precisely estimate damping ratios for low model orders, whereas damping ratios estimated by SSI-Cov typically converged immediately. Damping ratios estimated by both methods eventually converged towards the same value, however the convergence required significant model order for SSI-DD.

The three modal analysis techniques correctly identified whether each mode was torsional or vertical. The mode shapes from SSI-Cov clearly identified that the method struggled with closely spaced modes. The method managed to accurately separate the modes based on natural frequencies and damping ratios, but the energy dissipation was evident from the closely spaced modes' mode shapes. The presumed spurious mode with a natural frequency of 8.07 Hz corrupted the second mode shape from Raufoss and the first mode shape from Brumunddal.

Comparing the closely spaced modes estimated by SSI-Cov, it became evident that sensors exhibiting strange results in the corrupt mode shapes were emphasized in the presumed spurious mode shape. This indicated that SSI-Cov struggled with the energy dissipation between the closely spaced modes as the spurious mode absorbed energy intended for the corrupted mode shapes. The spurious mode was identified by all modal analysis techniques for the same exact frequency for both bridges. Structural drawings of both bridges indicate that they have identical railings. The mode was therefore assumed to belong to the bridges' railing. Both bridges were analyzed with the same equipment by the same students. This opens the possibility for the mode to be caused by equipment failure or systematic errors.

One of the main differences between the three methods was the required computational power. BFD required minimal computational power and analyzed the entire time series within a couple of minutes. The code for BFD was self-written and could thus be further optimized. This was, however, deemed unnecessary for the data analyzed in this thesis. The SSI methods, on the other hand, required substantial computational power. The time series had to be truncated and the number of block rows limited for the analyses to run. SSI-Cov required approximately half an hour to complete, while SSI-DD took well over an hour to complete. Even though the SSI methods are only meant to be employed on white noise data, both SSI-Cov and SSI-DD managed to accurately estimate the dynamic properties of the analyzed bridges. This might be caused by the hard roving hammer tip inducing a wide enough frequency range to be approximated to white noise.

Natural frequencies and mode shapes from the analytical analysis were accurately predicted by the ABAQUS model. However, the marginal effect the rotational stiffness had on the mode shapes was surprising. As seen in figure 6.44, the boundary edges of the model were distorted. These edges were expected to deform linearly. The code would unfortunately not run when the edges were constrained to deform linearly due to over constrained nodes. Successfully implementing this constraint, would most likely increase the accuracy of the mode shape. The additional constraint would increase the stiffness of the system and thus increase the estimated natural frequencies and lower the optimized rotational stiffness.

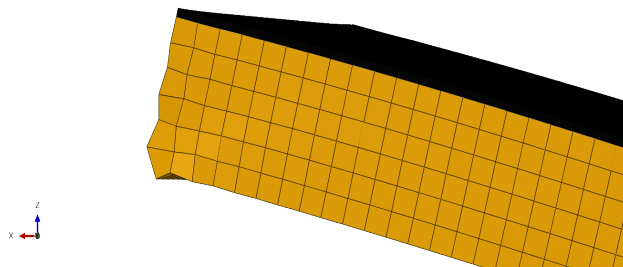


Figure 6.44: Screenshot of the boundary edge of the first mode shape for the Raufoss bridge with $k_{rot} = k_{opt}$.

Chapter 7

Concluding Remarks

7.1 Conclusion

Data from the Modal Hammer Test was separately analyzed by three different modal analysis techniques. Estimated natural frequencies from BFD method deviated from the frequencies estimated by the SSI methods. This deviation was likely caused by noise complicating the peak-picking process. Natural frequencies estimated by SSI-Cov had significantly smaller standard deviations compared to SSI-DD, but the mean values estimated by both SSI methods were practically identical. SSI-Cov struggled to estimate mode shapes for closely spaced modes. This inaccuracy was assumed to be caused by energy absorption by spurious modes. The inaccuracy was not present for BFD or SSI-DD. Damping ratios were solely estimated by the two SSI methods. The convergence plots indicated that damping ratios estimated with SSI-DD required higher model orders to converge while consistently overestimating damping ratios for lower model orders. Damping ratios estimated with SSI-Cov, on the other hand, converged for lower model orders. The estimated damping ratios were significantly larger compared to the 1.5% suggested by the European standard. The damping ratios for the first modes were estimated to be 4.4% for Raufoss and 4.8% for Brumunddal. This observation corresponds well with estimates from other timber bridges previously mentioned in section 1.2.

The BFD method required minimal computational power to estimate the natural frequencies and mode shapes. The method struggled to analyze closely spaced modes and should mainly be used to obtain rough estimates of the dynamic properties of the structure. The SSI methods yielded superior estimates of the dynamic properties but required substantial computational power. SSI methods should technically be employed on white noise data. Results indicated that the methods accurately predicted the dynamic behaviour from the MHT data even though the data not being white noise. One reason for this could be that the hard roving hammer tip induced a wide enough frequency range for the data to be approximated to white noise. SSI-Cov yielded superior estimates for natural frequencies and damping ratios compared to SSI-DD. However, SSI-DD accurately estimated the mode shapes of the closely spaced modes. SSI-DD required substantially more computational power compared to SSI-Cov, yet solely yield superior mode shapes for closely spaced modes. To most efficiently estimate the dynamic behaviour of

the bridges, BFD should be employed to get a rough estimate before estimating the dynamic properties with SSI-Cov.

The simplified ABAQUS model managed to accurately predict the natural frequencies and mode shapes of the bridge deck. The model was optimized to exactly predict the first natural frequency previously estimated by the modal analysis techniques. Data extracted from the model was compared to estimated values for the bridges which indicated that all MAC values exceeded 95% while the predicted natural frequencies were within a 10% error of the estimated values. The model's boundary edges were distorted resulting in the mode shapes barely being affected by the rotational stiffness. The accuracy of the result is expected to improve if the edges were constrained to deform linearly.

The first natural frequencies were extrapolated for temperatures between 0 and 40°C. The extrapolation was done for the optimized rotational stiffnesses. The true natural frequencies are therefore expected to be lower than estimated. The first natural frequency for the Raufoss bridge, became lower than 3.5 Hz for higher temperatures. The bridge was therefore analyzed for pedestrians running across the bridge. Assuming a natural frequency of 2.5 Hz and a damping ratio of 4.4%, the comfort criterion was fulfilled if no more than seven people jog across the bridge simultaneously. Extrapolation of the Brumunddal bridge indicated that the natural frequency wouldn't not go below 5 Hz. To be on the safe side, an assumed worst-case scenario of a natural frequency of 4.5 Hz and a damping ratio of 1.5% was investigated. The bridge fulfilled the comfort criterion for a continuous stream of people crossing the bridge for these assumptions. The damping ratio used in this calculation was also assumed conservative.

7.2 Further Work

The ABAQUS model should be modified to ensure that the boundary edges deform linearly. This should increase the stiffness and thus increase the estimated natural frequencies. This should also increase the mode shapes' sensitivity to added rotational stiffness and yield superior MAC values. To ensure convergence due to mesh size, the model should be run for a refined mesh. This will, however, require a more powerful computer than the ones we had available.

The temperature dependency of the asphalt pavement should be further analyzed. The ABAQUS model needs to be verified and optimized for other temperatures. Measurements must be conducted at different temperatures for this to be possible. The temperature dependency of the rotational stiffness could then be estimated. The temperature dependency of the damping ratios should also be investigated.

Bibliography

- [1] G. Mishra, “History of bridges – construction of bridges since ancient times,” <https://theconstructor.org/structures/history-of-bridges> [Accessed Date: 2022/03/21].
- [2] “Why timber is an environmentally friendly material,” <http://www.trefokus.no/treveilederen/temaer/miljo-og-berekraft/hvorfor-er-tre-et-miljovennlig-byggemateriale> [Accessed Date: 2022/03/23].
- [3] “Why use timber,” <https://bridgebuilders.com/timber-bridge-construction/why-use-timber> [Accessed Date: 2022/03/23].
- [4] G. Tilly, D. Cullington, and R. Eyre, “Dynamic behaviour of footbridges,” 1984.
- [5] D. P. Taylor, “Damper retrofit of the london millennium footbridge – a case study in biodynamic design,” 2002.
- [6] S. Gsell, D. Gsell, R. Steiger, and G. Feltrin, “Influence of asphalt pavement on damping ratio and resonance frequencies of timber bridges,” *Engineering Structures*, vol. 32, pp. 3122–3129, 10 2010.
- [7] CEN, “Ns-en 1990:2002+a1:2005+na:2016,” *Standard Norge*, 2016.
- [8] —, “Ns-en 1995-2:2004+na:2010,” *Standard Norge*, 2010.
- [9] G. Feltrin, R. Steiger, D. Gsell, A. Gülzow, and W. Wilson, “Serviceability assessment of a wooden trough bridge by static and dynamic tests,” 06 2010.
- [10] B. Peeters and G. De Roeck, “One year monitoring of the z24-bridge: Environmental influences versus damage events,” *Proceedings of SPIE - The International Society for Optical Engineering*, vol. 2, 05 2000.
- [11] B. Weber, “Dynamic properties of footbridges: Influence of asphalt pavement and support conditions,” *MATEC Web of Conferences*, vol. 24, p. 01004, 01 2015.
- [12] D. Giraldo, W. Song, S. Dyke, and J. Caicedo, “Modal identification through ambient vibration: Comparative study,” *Journal of Engineering Mechanics-asce - J ENG MECH-ASCE*, vol. 135, 08 2009.

- [13] P. Nåvik, A. Rønquist, and S. Stichel, “Identification of system damping in railway catenary wire systems from full-scale measurements,” *Engineering Structures*, vol. 113, pp. 71–78, 04 2016.
- [14] F. Magalhães, E. Caetano, and A. Cunha, “Operational modal analysis and finite element model correlation of the braga stadium suspended roof,” *Engineering Structures*, vol. 30, pp. 1688–1698, 06 2008.
- [15] R. Crocetti, K. Ekholm, and R. Kliger, “Stress-laminated-timber decks: state of the art and design based on swedish practice,” 2015.
- [16] M. Ritter and U. S. F. S. E. Staff, *Timber Bridges: Design, Construction, Inspection, and Maintenance*, ser. Engineering management. U.S. Department of Agriculture, Forest Service, Engineering Staff, 1990.
- [17] “Ski- og turbro over holmenkollveien klar til bruk,” <https://kommunikasjon.ntb.no/pressemelding/ski--og-turbro-over-holmenkollveien-klar-til-bruk?publisherId=12550484&releaseId=17906935> [Accessed Date: 2022/03/14].
- [18] J. A. Kainz and M. A. Ritter, “Effect of cold temperatures on stress-laminated timber bridge decks.”
- [19] K. Ekholm, “Performance of stress-laminated-timber bridge decks,” *Chalmers University of Technology*, 2013.
- [20] M. G. Oliva and A. G. Dimakis, “Behavior of stress-laminated timber highway bridge,” *Journal of Structural Engineering-asce*, vol. 114, pp. 1850–1869, 1988.
- [21] “The environmental benefits of timber-frame buildings,” <https://www.bsstainless.com/the-environmental-benefits-of-timber-frame> [Accessed Date: 2022/03/14].
- [22] A. K. Chopra, *Dynamics of Structures*. Pearson Education, 2012.
- [23] G. F. Franklin, Giovanni, J. D. Powell, and M. Workman, *Digital Control of Dynamic Systems*. Ellis-Kagle Press, Half Moon Bay, California, 2014.
- [24] C. Rainieri and G. Fabbrocino, *Operational Modal Analysis of Civil Engineering Structures: An Introduction and Guide for Applications*. Springer-verlag New York inc., 2014.
- [25] S. Qin, J. Kang, and Q. Wang, “Operational modal analysis based on subspace algorithm with an improved stabilization diagram method,” *Hindawi Publishing Corporation*, vol. 2016, 2015.
- [26] B. Peeters and G. D. Roeck, “Stochastic system identification for operational modal analysis: A review,” *Journal of Dynamic Systems, Measurement, and Control*, vol. 123, 2001.

- [27] H. Akaike, “Stochastic theory of minimal realization,” 1974.
- [28] R. Bagheri, “Understanding singular value decomposition and its application in data science,” <https://towardsdatascience.com/understanding-singular-value-decomposition-and-its-application-in-data-science-388a54be95d> [Accessed Date: 2022/02/01].
- [29] P. Van Overschee and B. De Moor, *Subspace identification for linear systems. Theory, implementation, applications. Incl. 1 disk*, 01 1996, vol. xiv, pp. xiv + 254.
- [30] —, *Subspace algorithms for the stochastic identification problem*, 1993, vol. 29, no. 3, p. 649 to 660.
- [31] E. Reynders, J. Houbrechts, and G. De Roeck, “Fully automated (operational) modal analysis,” *Mechanical Systems and Signal Processing*, vol. 29, pp. 228–250, 05 2012.
- [32] D. F. Elliott, *Handbook of Digital Signal Processing: Engineering Applications*, 1988.
- [33] A. J. Felber, “Development of a hybrid bridge evaluation system,” 1993.
- [34] M. H. Hayes, *Statistical Digital Signal Processing and Modeling*, 1996.
- [35] “Hanning window.” [Online]. Available: <https://docs.scipy.org/doc/scipy-1.0.0/reference/generated/scipy.signal.hanning.html>
- [36] R. J. Allemang, “The modal assurance criterion (mac): Twenty years of use and abuse.”
- [37] E. Obeng, Y. A. Tuffour, D. A. Obeng, and B. Koranteng-Yorke, *Preliminary k-Values of Unbound Natural Quartzitic Gravels for Mechanistic-Empirical Pavement Design*. The Society for Experimental Mechanics and John Wiley & Sons Ltd, 2004.
- [38] T. Pellinen, M. Witczak, and R. Bonaquist, “Asphalt mix master curve construction using sigmoidal fitting function with non-linear least squares optimization,” 12 2003, pp. 83–101.
- [39] G. D. R. K. Van Nimmen, G. Lombaert and P. V. den Broeck., “Vibration serviceability of footbridges: Evaluation of the current codes of practice,” *Engineering Structures*, 2014.
- [40] V. Racic, A. Pavic, and J. Brownjohn, “Experimental identification and analytical modelling of human walking forces: Literature review,” *Journal of Sound and Vibration*, 2009.
- [41] H. Bachmann, W. J. Ammann, F. Deischl, J. Eisenmann, I. Floegl, G. H. Hirsch, G. K. Klein, G. J. Lande, O. Mahrenholtz, H. G. Natke, H. Nussbaumer, A. J. Pretlove, J. H. Rainer, E.-U. Saemann, and L. Steinbeisser, *Vibration Problems in Structures*. The Society for Experimental Mechanics and John Wiley & Sons Ltd, 1995.
- [42] L. K. Martinsen and S. O. Johansen, “Dynamic properties of stresslaminated timber bridges,” 06 2021.

- [43] M.Tarfaoui, P.B.Gning, and L.Hamitouche, *Modal Testing: A practitioner's guide*. The Society for Experimental Mechanics and John Wiley & Sons Ltd, 2008.
- [44] G. T. Frøseth, "Gunnstein/strid: strid - v0.4.3," May 2022. [Online]. Available: <https://doi.org/10.5281/zenodo.6540518>
- [45] M. Pletz, "Efficient FE Modelling Course – understanding mechanics." [Online]. Available: <https://www.martinpletz.com/fe-scripting/>
- [46] C. Liu, J. DeWolf, and J.-H. Kim, "Development of a new cracked mindlin plate element," <https://www.hindawi.com/journals/isrn/2011/842572/> [Accessed Date: 2022/03/15].
- [47] "Eight-node brick element (c3d8 and f3d8)," https://web.mit.edu/calculix_v2.7/CalculiX/ccx_2.7/doc/ccx/node26.html [Accessed Date: 2022/03/15].
- [48] S. Vegvesen, "N400:2022 n400 bruprojektering," 2022.

A Python Code to Model the Bridge in ABAQUS

In []:

```
from abaqus import *
from abaqusConstants import *
from caeModules import *
import os
import numpy as np
from odbAccess import *
import math

session.journalOptions.setValue(replayGeometry=COORDINATE,
                                recoverGeometry=COORDINATE)
DIR0 = os.path.abspath('')

""" This function analyzes SLT bridges consisting of GL30C.
Steps to run the code:
1. Change the parameters at the bottom of the script to fit the bridge
and save the code
2. Open the folder where this script is saved, right click, and open
PowerShell
3. Write "Abaqus cae" and press enter
4. Execute the code by writing execfile('CodeName.py') in the Kernel
Command in ABAQUS"""

def make_geometry_solid(model,L,B,partname,t,dh):
    # draw the sketch
    s = model.ConstrainedSketch(name='plate', sheetSize=200.0)
    s.rectangle(point1=(0.0, 0.0), point2=(L, B))

    # create the part
    p = model.Part(name=partname, dimensionality=THREE_D, type=DEFORMABLE_BODY)
    p.BaseSolidExtrude(depth=t, sketch=s)

    p.Set(name='all', faces=p.faces[:])
    p.Set(name='Horizontal', edges=p.edges.findAt(((L/2,B,t)),((L/2,0,t)),))
    p.Set(name='Vertical', edges=p.edges.findAt(((0,B/2,t)),((L,B/2,t)),))

    p.Set(faces=p.faces.findAt(((L/2, B/2, 0), )), name='Align z-dir')

    p.Surface( name='Align z-dir', side1Faces=p.faces.findAt(((L/2, B/2, t), )))

    p.Surface( name='BC_srf1', side1Faces=p.faces.findAt(((0, B/2, t/2), )))
    p.Surface( name='BC_srf2', side1Faces=p.faces.findAt(((L, B/2, t/2), )))

    p.Set(faces=p.faces.findAt(((0.0, B/2, t/2), )), name='Align x-dir')
    p.Set(faces=p.faces.findAt(((L/2, B, t/2), )), name='Align y-dir')

    p.Set(name='BC-Line1', edges=p.edges.findAt(((L,B/2,0)),))
    p.Set(name='BC-Line2', edges=p.edges.findAt(((0,B/2,0)),))

    p.Set(name='BC-Line3', edges=p.edges.findAt(((L,B/2,t)),))
    p.Set(name='BC-Line4', edges=p.edges.findAt(((0,B/2,t)),))

    # meshing
    p.seedPart(size=dh)
    p.generateMesh()
    return p
```

```

def make_geometry_shell(model,L,B,partname,div,dh):
    # draw the sketch
    s = model.ConstrainedSketch(name='plate', sheetSize=200.0)
    s.rectangle(point1=(0.0, 0.0), point2=(L, B))

    # create the part
    p = model.Part(name=partname, dimensionality=THREE_D, type=DEFORMABLE_BODY)
    p.BaseShell(sketch=s)

    # create sets, surfaces, and reference point
    p.Set(name='all', faces=p.faces[:])
    p.Set(name='Horizontal', edges=p.edges.findAt(((L/2,B,0)),((L/2,0,0)),))
    p.Set(name='Vertical', edges=p.edges.findAt(((0,B/2,0)),((L,B/2,0)),))
    p.Set(name='BC-Line1', edges=p.edges.findAt(((L,B/2,0)),))
    p.Set(name='BC-Line2', edges=p.edges.findAt(((0,B/2,0)),))

    # meshing
    p.seedPart(size=dh)
    return p

def make_sections(model,p1,p2,E1,E2,E3,G12,G13,G23,v12,v13,v23,rho1,t1,E,v,rho2,t2):
    # create material, create and assign sketch Options
    mat1 = model.Material(name='Glulam')
    mat1.Density(table=((rho1, ), ))
    mat1.Elastic(table=((E1,E2,E3,v12,v13,v23,G12,G13,G23), ),
                type=ENGINEERING_CONSTANTS)

    mat2 = model.Material(name='Asphalt')
    mat2.Density(table=((rho2, ), ))
    mat2.Elastic(table=((E, v), ))

    model.HomogeneousSolidSection(material='Glulam', name='SLTD CS',
                                   thickness=None)
    p2.Set(cells=p2.cells.getSequenceFromMask(['[#1 ]', ], ), name='SLTD')
    p2.SectionAssignment(offset=0.0, offsetField='', offsetType=MIDDLE_SURFACE,
                        region=p2.sets['SLTD'], sectionName='SLTD CS',
                        thicknessAssignment=FROM_SECTION)
    p2.MaterialOrientation(additionalRotationField='',
                          additionalRotationType=ROTATION_NONE, angle=0.0
                          , axis=AXIS_1, fieldName='', localCsys=None, orientationType=SYSTEM,
                          region=p2.sets['SLTD'], stackDirection=STACK_3)

    p1.Compositelayout(description='',
                      elementType=SHELL, name='Asphalt CS', offsetType=BOTTOM_SURFACE,
                      symmetric=False, thicknessAssignment=FROM_SECTION)
    p1.compositelayouts['Asphalt CS'].Section(
        integrationRule=SIMPSON, poissonDefinition=DEFAULT, preIntegrate=OFF,
        temperature=GRADIENT, thicknessType=UNIFORM, useDensity=OFF)
    p1.compositelayouts['Asphalt CS'].ReferenceOrientation(
        additionalRotationType=ROTATION_NONE, angle=0.0, axis=AXIS_3, fieldName='',
        localCsys=None, orientationType=GLOBAL)
    p1.compositelayouts['Asphalt CS'].CompositePly(
        additionalRotationField='', additionalRotationType=ROTATION_NONE, angle=0.0
        , axis=AXIS_3, material='Asphalt', numIntPoints=3, orientationType=
        SPECIFY_ORIENT, orientationValue=0.0, plyName='Ply-1',
        region=p1.sets['all'], suppressed=False, thickness=t2,
        thicknessType= SPECIFY_THICKNESS)
    return

def make_assembly(model,p1,p2,t1,t2):

```

```

# assembly
a = model.rootAssembly
inst1 = a.Instance(name='Asphalt - 1', part=p1, dependent=ON)
inst2 = a.Instance(name='SLTD - 1', part=p2, dependent=ON)

inst1.translate(vector=(0.0, 0.0, t2))
return inst1,inst2

def make_boundaries(model,inst1,inst2,n,L,B,t2,BC_u1):
# step and history output
step = model.FrequencyStep(name='Frequency', previous='Initial', numEigen=n)

model.DisplacementBC(amplitude=UNSET, createStepName=
'Frequency', distributionType=UNIFORM, fieldName='', fixed=OFF,
localCsys=None, name='BC-1', region= inst2.sets['BC-Line1'], u1=0.0,
u2=0.0, u3=0.0,
ur1=UNSET, ur2=UNSET, ur3=UNSET)

model.DisplacementBC(amplitude=UNSET, createStepName=
'Frequency', distributionType=UNIFORM, fieldName='', fixed=OFF,
localCsys=None, name='BC-2', region= inst2.sets['BC-Line2'], u1=BC_u1,
u2=0.0, u3=0.0,
ur1=UNSET, ur2=UNSET, ur3=UNSET) #unset

a = model.rootAssembly

a.Surface(name='m_Surf-3', side2Faces=inst1.faces.findAt(((L/2, B/2, t2), )))
a.Surface(name='s_Surf-3', side1Faces=inst2.faces.findAt(((L/2, B/2, t2), )))
model.Tie(adjust=ON, master=a-surfaces['m_Surf-3'], name=
'Constraint-1', positionToleranceMethod=COMPUTED,
slave=a-surfaces['s_Surf-3'], thickness=ON, tieRotations=ON)
return

def partition_part(model,p,div,L,B):
dy = np.linspace(0,B,div)
for i,y in enumerate(dy[1:-1]) :
a = p.DatumPlaneByThreePoints((0.0, y, 0.0), (L, y, 0.0), (0.0, y, 100))
p.PartitionEdgeByDatumPlane(datumPlane=p.datums[a.id],
edges=p.edges.findAt(((0.0, y, 0.0), )))
p.PartitionEdgeByDatumPlane(datumPlane=p.datums[a.id],
edges=p.edges.findAt(((L, y, 0.0), )))

return

def stiffness(model,p,L,B,div,K):
dy = np.linspace(0,B,div)
for i,y in enumerate(dy) :
if i == 0 or i == div-1:
p.engineeringFeatures.SpringDashpotToGround(
dashpotBehavior=OFF, dashpotCoefficient=0.0, dof=1,
name='Springs/Dashpots'+str(i), orientation=None,
region=regionToolset.Region(
vertices=p.vertices.findAt(((0.0, y, 0.0), ),
((L, y, 0.0), ), ),
springBehavior=ON, springStiffness=K*0.5)
else :
p.engineeringFeatures.SpringDashpotToGround(
dashpotBehavior=OFF, dashpotCoefficient=0.0, dof=1,
name='Springs/Dashpots'+str(i), orientation=None,
region=regionToolset.Region(
vertices=p.vertices.findAt(((0.0, y, 0.0), ),

```

```

        ((L, y , 0.0), ), ),
        springBehavior=ON, springStiffness=K)

    return

def IdentifySensors(model,p,X,Y,t):
    b = np.shape(X)
    for i in range(b[1]):
        a = p.DatumPlaneByThreePoints((X[0][i], 0.0, 0.0), (X[0][i], B, 0.0),
                                       (X[0][i], 0.0, 100))
        p.PartitionFaceByDatumPlane(datumPlane=p.datums[a.id],
                                    faces=p.faces.findAt(((X[0][i], B/2, 0.0), )))
    for i in range(b[0]):
        a = p.DatumPlaneByThreePoints((0.0, Y[i][0], 0.0), (L, Y[i][0], 0.0),
                                       (0.0, Y[i][0], 100))
        for j in range(1,b[1],1):
            p.PartitionFaceByDatumPlane(datumPlane=p.datums[a.id],
                                        faces=p.faces.findAt(((X[0][j]-10, Y[i][0], 0.0), )))
    p.generateMesh()

    n = 0
    for j in range(b[0]):
        for i in range(b[1]):
            n = n + 1
            p.Set(name='Sensor_nr 100'+str(n),
                  vertices=p.vertices.findAt(((X[0][i], Y[j][0], 0.0), )))
    return

def MakeOuput(model,inst,X):
    b = np.size(X)
    for i in range(b) :
        model.FieldOutputRequest(createStepName='Frequency',
                                 name='Displacement sensor nr '+str(i+1), rebar=EXCLUDE, region=
                                 inst.sets['Sensor_nr 100'+str(i+1)], sectionPoints=DEFAULT, variables=PRESELECT)
    return

def evaluate_historyOutput(model,filename,BC,K):
    a = model.rootAssembly
    session.viewports['Viewport: 1'].setValues(displayedObject=a)
    o3 = session.openOdb(name='plate-test.odb')
    session.viewports['Viewport: 1'].setValues(displayedObject=o3)

    odb = session.odbs['plate-test.odb']

    # Delete old output requests
    for i in range(1,16,1):
        try:
            del session.xyDataObjects['Sensor '+str(i)]
        except:
            continue

    # Make new output requests and save the data
    for i in range(1,16,1):
        try :
            del session.xyDataObjects['U:U3 PI: Asphalt - 1 N: '+str(i)]
        except :
            continue
    for i in range(1,16,1) :
        session.xyDataListFromField(odb=odb, outputPosition=NODAL, variable=((('U',
        NODAL, ((COMPONENT, 'U3'), )), ),
        nodeSets=("Asphalt - 1.Sensor_nr 100"+str(i), ))

    for j in range(50):

```

```

        try:
            session.xyDataObjects.changeKey(fromName='U:U3 PI: Asphalt - 1 N: '+str(j),
                                           toName='Sensor '+str(i))
        except:
            continue

data = [session.xyDataObjects['Sensor '+str(i+1)] for i in range(15)] #range(Leng(x))
session.writeXYReport(fileName=filename+'.txt',xyData = data, appendMode=0)

odb = openOdb(path='plate-test.odb')
step1 = odb.steps['Frequency']
region = step1.historyRegions['Assembly ASSEMBLY']
freqData = region.historyOutputs['EIGFREQ'].data

# np.savez(filename+"frequency.npz", f=freqData)
np.savetxt(filename+' frequency.txt',freqData)
odb.close()
return

def asphalt_stiffness(T,f):
    d, a, b, g, C1, C2 = 0.9, 3.8, -0.9, 0.4, 16, 110
    log_at = -C1*(T-15)/(C2 + T - 15 )
    log_fr = log_at + np.log10(f)
    log_E = d + a/(1+np.exp(b-g*log_fr))
    return 10**log_E

def run_model(model,job_name):
    # create and run job
    job = mdb.Job(name=job_name, model='Model-1', type=ANALYSIS, resultsFormat=ODB)
    job.submit(consistencyChecking=OFF)
    job.waitForCompletion()
    return

def plate_model(job_name,L,B,E1,E2,E3,G12,G13,G23,v12,v13,v23,rho1,
                t2, E,v,rho2,t1,n,K,div,X,Y,filename,BC,dh):
    # check parameters for errors
    if B >= L:
        raise ValueError('Length of the model should be greater than the width')
    # reset model
    Mdb()
    model = mdb.models['Model-1']
    # make the parts, mesh it and return it
    p1 = make_geometry_shell(model,L,B,'Asphalt',div,dh)
    p2 = make_geometry_solid(model,L,B,'SLTD',t2,dh)
    # make materials and sections
    make_sections(model, p1,p2,E1,E2,E3,G12,G13,G23,v12,v13,v23,rho1,t2,E,v,rho2,t1)
    # make the assembly & constraint
    inst1,inst2 = make_assembly(model,p1,p2,t1,t2)
    # create step and boundaries
    make_boundaries(model,inst1,inst2,n,L,B,t2,BC)
    # Add rotational stiffness
    if K > 0 :
        partition_part(model,p1,div,L,B)
        stiffness(model,p1,L,B,div,K)
    # Make sets for each of the sensors
    IdentifySensors(model,p1,X,Y,t2)
    # Create field output
    MakeOuput(model,inst1,X)

```

```

# save the model
mdb.saveAs(job_name)
# run the model
# run_model(model,job_name)
# # Extract the modeshape and natural frequencies
# evaluate_historyOutput(model,filename,BC,K)
return model

## Define the Length and width
L = 22000 #mm 22000 12500
B = 4046 #mm 4046 3885

# Define the name of the text file saved
filename = 'Raufoss Data'

# Material properties of the timber
Ex = 10800 #MPa
Ey = 250 #MPa
Ez = 250 #MPa
Gxy = 540 #MPa
Gxz = 540 #MPa
Gyz = 54 #MPa
v12 = 0.5
v13 = 0.6
v23 = 0.6
rho_1 = 430*1.15 + 0.8 #kg/m3 Se notater

# Define the temperature and Loading frequency of the asphalt pavement
T = 3 # degrees celsius
f = 4 # Assumed first natural frequency
e = asphalt_stiffness(float(T),float(f)) #MPa
v = 0.3 # -
rho_2 = 2322 #kg/m3 2322 2243

# Define thicknesses
t_asphalt = 35 #mm
t_wood = 600 # mm 600 367

# Define horizontal stiffness
k = 60 #500 N/mm/mm

# Define amount of modes analyzed
n = 10

# Ensures six elements in the height direction of the SLT deck
dh = t_wood/6
div = math.floor(B/dh)

# Define the boundary condition; roller=UNSET, pinned=0.0
BC = 0.0

# ----- Convert Inpyt to Correct Units -----
rho_1 = rho_1 * 10**(-12)
rho_2 = rho_2 * 10**(-12)

# ----- Convert uniformly distribute stiffness to point stiffness
db = B/(div-1)
K = db*k

```

```
# ----- Sensor placement -----  
x = L*np.array([0.15,0.3,0.5,0.7,0.85])  
y = B*np.array([0.05,0.5,0.95])  
  
X,Y = np.meshgrid(x,y)  
  
# ----- Run Code -----  
plate_model('plate-test',L,B,Ex,Ey,Ez,Gxy,Gxz,Gyz,v12,v13,v23,rho_1,t_wood,e,  
            v,rho_2,t_asphalt,n,K,div,X,Y,filename,BC,dh)
```


B Zip-file

All codes and data sets used throughout this thesis are saved in zip-file. The content of this zip-file will be further explained:

- ABAQUS_Model

This is a folder that contains two Python scripts: “PythonCode” and “text2npz”. “PythonCode” is the same code as presented in Appendix A. The file models, runs, and extracts the mode shapes and natural frequencies to text-files. “text2npz” reads the text files and saves the data into npz-files.

- Analyzed_Data

Contains the data analyzed in the thesis. Each bridge has its own folder and contains the Modal Hammer Test data, Jumping Test data, the truncated time series, and the time stamps of the measurements.

- Basic_Frequency_Domain_Method

This folder contains one Python script named “BFD”. This self-written script analyzes the time series in the frequency domain.

- Stochastic_Subspace_Identification_Method

Contains two Python scripts: “Covariance-Driven” and “Data-Driven”. These scripts analyze the time series using SSI-Cov and SSI-DD, respectively.

